RALT-022

# A Measurement of the Structure Function of the Proton, $F_2(x, Q^2)$, at Low Bjorken-$x$

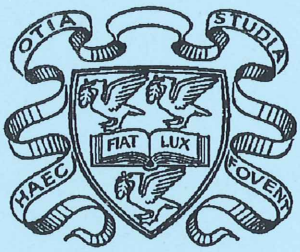


Thesis submitted in accordance with the requirements of the University of Liverpool for the degree of Doctor of Philosophy

by

Roland Martin

April 1994

Oliver Lodge Laboratory
University of Liverpool

# A Measurement of the Structure Function of the Proton, $F_2(x, Q^2)$, at Low Bjorken-$x$

**Roland Martin**
**Liverpool, 1994**

# Abstract

The HERA accelerator collides $820 GeV$ protons with $26.7 GeV$ electrons. This gives a much higher centre of mass energy for $ep$ collisions than has been hitherto possible allowing the structure of the proton to be investigated in an entirely new kinematic region.

This thesis presents measurements of the structure function of the proton, $F_2(x, Q^2)$, as a function of both Bjorken $x$ and $Q^2$ in a new kinematic domain of $x$ between $2 \cdot 10^{-4}$ and $2 \cdot 10^{-2}$, and $Q^2$ between $8.5\, GeV^2$ and $60\, GeV^2$. The structure function is observed to rise sharply with decreasing $x$, which may be attributable to new physics in the structure of the proton associated with a surprisingly large gluon density. The $Q^2$ evolution of the structure function is measured to be consistent within experimental errors with both QCD GLAP evolution and scale invariance.

# Acknowledgments

I would like to thank my supervisor, John Dainton, for his continual support, encouragement and enthusiasm throughout my years as a PhD student.

I would also like to thank the rest of the Liverpool H1 group for helping me both in and outside work.

I am indebted to everyone at DESY for their assistance, especially the H1 ELAN working group.

Thanks are also due to the Science and Engineering Research Council (SERC) for financial support between October 1990 and October 1993.

I must also thank my parents, my sister and my brother whose constant encouragement and support has made all this possible.

Finally I would like to thank all the people I have met in Hamburg, especially the members of the Ruder-Gesellschaft Hansa, for making my stay in Germany so enjoyable.

# The Author's Contribution

This thesis is concerned with part of the *ep* physics program of the H1 experiment at DESY Hamburg. The data whose analysis is presented here were taken as part of a collaborative effort involving the many physicists and engineers of the H1 collaboration. My involvement with this work was as a member of the Liverpool H1 group where I took specific responsibility for aspects of the construction, installation and operation of the H1 radial wire drift chambers at Liverpool, in high energy test beams at CERN and in H1 for the first *ep* data taking. Simultaneously I worked as part of the H1 'ELAN' working group concerned with the extraction of the proton structure function $F_2(x, Q^2)$. The physics analysis presented here was carried out by myself using an established unfolding technique. The results are consistent with those published by H1 in summer 1993.

# Contents

# List of Figures

# List of Tables

# Chapter 1

# Introduction

Much of our current understanding of the nature of matter comes from high energy deep inelastic lepton scattering. This is due to the point-like nature of the leptons, which provides a clean probe with which to study the sub-structure of other particles. In an interaction, a boson with four momentum squared, $Q^2$, is exchanged between the proton, or a part of the proton (parton), and the lepton. The larger the $Q^2$, the smaller the scale inside the nucleon that can be probed. Another useful variable is Bjorken $x$ (henceforth referred to just as $x$), which is the fraction of the incident proton's momentum carried by the struck parton.

HERA (Hadron Electron Ring Anlage), is designed to collide $820\,GeV$ protons and $30\,GeV$ electrons. The collider presents new challenges in both accelerator and detector design and construction. HERA consists of two storage rings in a tunnel of $6.3\,km$ circumference, one for the protons and one for the electrons. In order to contain such high energy protons in the ring, superconducting magnets of $4.7\,T$ are required. Owing to the relatively small cross section for deep inelastic electron-proton scattering, bunches cross every $96\,ns$ in order to produce a reasonable rate for interesting physics events. This short bunch crossing time, and the high rates of background events require detectors that are able to efficiently and quickly reject background events.

Colliding accelerated beams of particles gives a much higher centre of mass energy for the collisions than at fixed target experiments in which leptons have been scattered off stationary nucleons. The high centre of mass of the collisions not only allows experiments to measure events at very high $Q^2$ (up to about $10^5\,GeV^2$) but also down to much lower $x$ than has been previously attainable. This region has been of considerable interest, not only in planning for future high energy proton-proton colliders, but also because there are widely differing theoretical predictions for the numbers of partons that might be seen at small $x$

in a proton.

This thesis is concerned with neutral current deep inelastic scattering (DIS). The electron scatters off the proton, via the exchange of a virtual photon or $Z^0$ (neutral current), breaking the proton up in the process (inelastic scattering), with the exchange of a boson whose $Q^2$ is larger than the mass of the proton (deep) so that the structure of the proton is resolved. Experiments at HERA can also study many other physics processes. As well as neutral current DIS, at sufficiently high $Q^2$ charged current DIS, in which the electron scatters to a neutrino via the exchange of a $W^{\pm}$, can be studied. The total cross section for $ep$ scattering is dominated by photoproduction, the scattering of a nearly real photon off the proton. This can be used to provide information on the structure of the photon. HERA is also an ideal place to search for 'exotic' particles, such as lepto-quarks.

Chapter 2 of this thesis discusses the theory of DIS and the structure of the proton. Following an overview of the H1 detector (chapter 3), the selection of DIS events is described in chapter 4. The measurement of the proton structure function as a function of $x$ at fixed $Q^2$ and $Q^2$ at fixed $x$ using DIS $ep$ events is then presented in chapter 5.

# Chapter 2

# HERA Physics

## 2.1 Deep Inelastic Scattering

A schematic diagram of a deep inelastic scattering (DIS) event is shown in figure 2.1. An incoming lepton, with four-momentum $k^\mu$, scatters off the proton (four-momentum $P^\mu$) via the exchange of a vector boson (4-momentum $q^\mu$). In neutral current (NC) DIS, the exchanged boson is a photon or a $Z^0$, in charged current (CC) it is a $W^\pm$ boson. After the interaction, the scattered lepton has a four-momentum $k'^\mu$ and the four-momentum of the vector sum of all the final state particles except the lepton is $P'^\mu$.

Some of the variables commonly used to describe the kinematics of the collision are

$$Q^2 = -q^2 = -(k^\mu - k'^\mu)^2 \ , \tag{2.1}$$

the four-momentum transfer squared;

$$x = \frac{Q^2}{2\,P \cdot q} \ , \tag{2.2}$$

the Bjorken scaling variable, which can be shown to be the fraction of the proton's momentum carried by the struck parton in the infinite momentum frame of the proton (or if the partons are assumed to be massless);

$$y = \frac{P \cdot q}{k \cdot q} \ , \tag{2.3}$$

the fractional energy loss of the electron in the proton rest frame, or $\frac{1}{2}(1-\cos\theta^\star)$, where $\theta^\star$ is the angle of the scattered lepton in the electron–parton rest frame;

$$\nu = \frac{P \cdot q}{M_{proton}} \ , \tag{2.4}$$

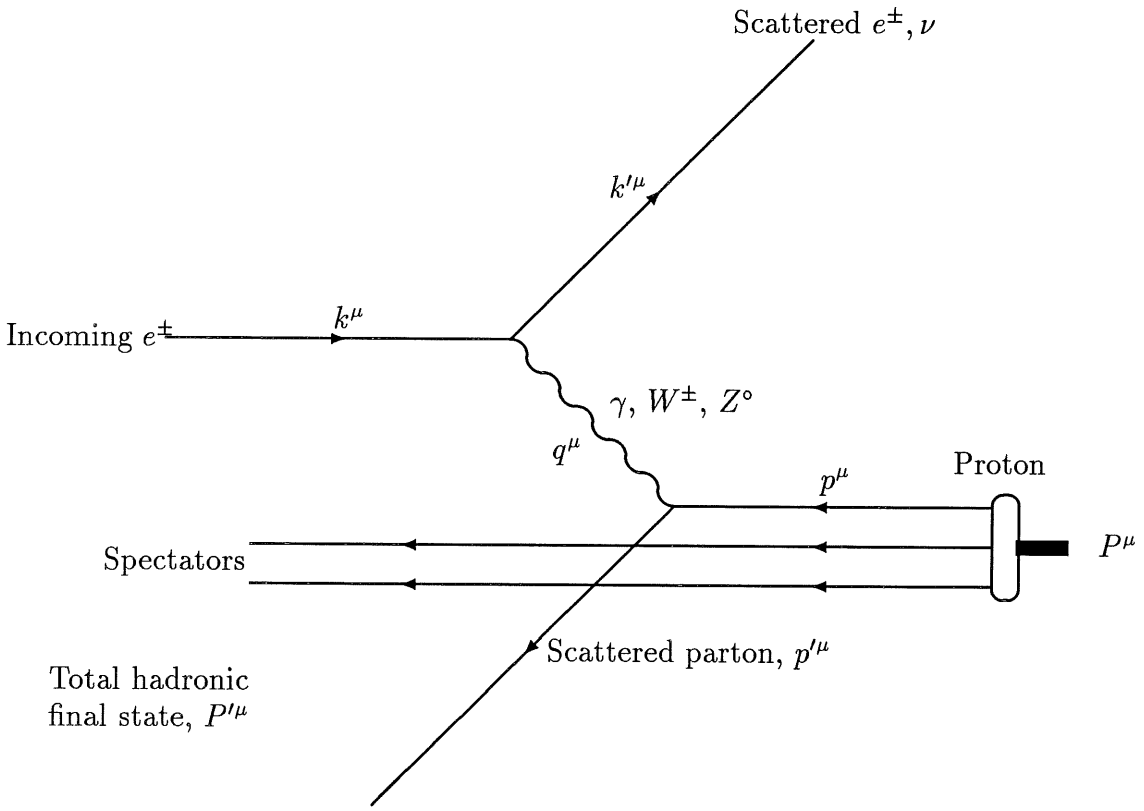


Figure 2.1: Schematic diagram of a DIS event. The scattered parton hadronizes to form the 'current' jet, the spectators to form the 'target' jet.

the energy loss of the electron in the proton rest frame;

$$W^2 = P' \cdot P' \ , \tag{2.5}$$

the invariant mass of the hadronic final state.

There are, however, only two independent variables. Equations 2.1 to 2.5 are related by

$$Q^2 = sxy \tag{2.6}$$

where $s$ is the centre of mass energy of the $ep$ collision,

$$x = \frac{Q^2}{2M_{proton}\nu} \tag{2.7}$$

and

$$W^2 = \frac{(1-x)Q^2}{x} \tag{2.8}$$

provided that the energy scale ($Q^2$ or $W^2$) of the process is much greater than the proton rest mass.

Figure 2.2 shows the direction and energy of the scattered electron and scattered parton in the form of vectors for the HERA beam energies used in this measurement.

## 2.2 Kinematic Reconstruction

In terms of observable quantities, $Q^2$ and $y$ have the simplest forms. The kinematics can be calculated from either the electron or the hadronic final state.

In terms of the electron variables,

$$y = 1 - \frac{E'_e}{E_e}\sin^2\frac{\theta'_e}{2} \ , \tag{2.9}$$

and

$$Q^2 = 4E_eE'_e\cos^2\frac{\theta'_e}{2} \ , \tag{2.10}$$

where $E_e$ is the electron beam energy (26.7 GeV), $E'_e$ is the scattered lepton energy and $\theta'_e$ the scattered lepton angle in the H1 convention[1]. Figures 2.3 (a) and (b) show lines of constant angle and energy on the $x, Q^2$ plane. This thesis is concerned with data at relatively low $Q^2$ ($4\,GeV^2 < Q^2 < 100\,GeV^2$) compared

[1]In H1 the proton beam direction defines the positive z-axis.

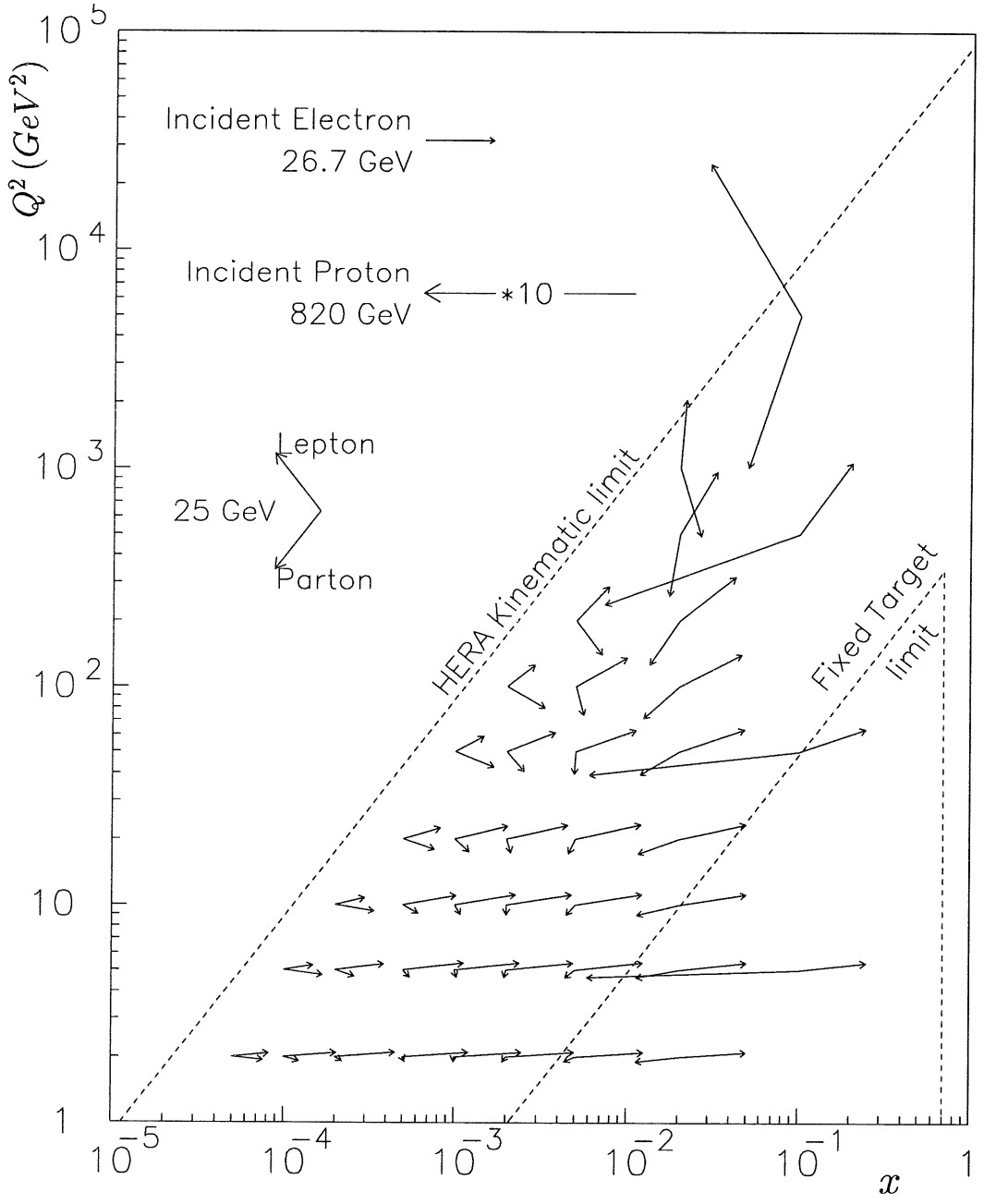


Figure 2.2: The energy and angle of the scattered lepton and current jet as a function of $x$ and $Q^2$.

with the HERA kinematic limit, corresponding to the electron being scattered at large angles, $\theta$. As can be seen, there is a large region of the kinematic domain for which the electron energy changes by only a small amount. This is seen in the energy spectrum of the scattered electrons as a peak around the beam energy (the 'kinematic peak') and is used for detector calibration. It should also be noted that the resolution in $y$ gets worse as one goes to smaller $y$, giving poor $x$ reconstruction at high values of $x$.

In calculating the kinematics from the hadronic final state it must be remembered that much of the energy of the proton spectators ('target jet') is lost in the forward beam pipe. Also, it may be difficult to correctly assign particles to the struck parton ('current') jet because of smearing and fragmentation. To overcome these difficulties, the method of Jacquet-Blondel [1] is used. In this method, all the final state particles, except the scattered electron, are used. The kinematics can then be calculated from

$$y = \frac{1}{2E_e}\sum_{all}(E - P_z)\ , \tag{2.11}$$

and

$$Q^2 = \frac{1}{1-y}\left((\sum_{all} P_x)^2 + (\sum_{all} P_y)^2\right)\ , \tag{2.12}$$

where the sum is over all final state particles except the scattered electron. This method also has the advantage of minimizing the effect of not detecting all the particles due to losses in the beam pipe. For a particle lost in the beam pipe in the proton direction, for example particles from the target jet, the energy and longitudinal momentum are almost the same, and the transverse momentum is small. The situation is much worse for particles that are lost down the beam pipe in the backward direction, as the contribution of such a particle to the calculation of $y$ is almost twice its energy. Figures 2.2 and 2.3 show that this latter case is unlikely except at very large $y$ (low electron energy).

Both of the above methods are sensitive to the energy scales of the calorimeters. This sensitivity can be reduced using the 'double angle' method, in which the kinematics are calculated from the angle of the scattered electron and $\gamma_h$, defined by

$$\cos\gamma_h = \frac{(\sum P_x)^2 + (\sum P_y)^2 - (\sum(E - P_z))^2}{(\sum P_x)^2 + (\sum P_y)^2 + (\sum(E - P_z))^2} \tag{2.13}$$

where the sum is over all final state particles except the scattered electron. $\gamma_h$ is the angle of the current jet in the model of figure 2.1. This method can also be used to predict the scattered electron energy and thus to be of use in calibration. The mapping of current jet energy and angle on the $x, Q^2$ plane is shown in figures 2.3 (c) and (d). As has been seen, there are four useful measured quantities that can be used in calculating the kinematics of any event. Since the kinematics

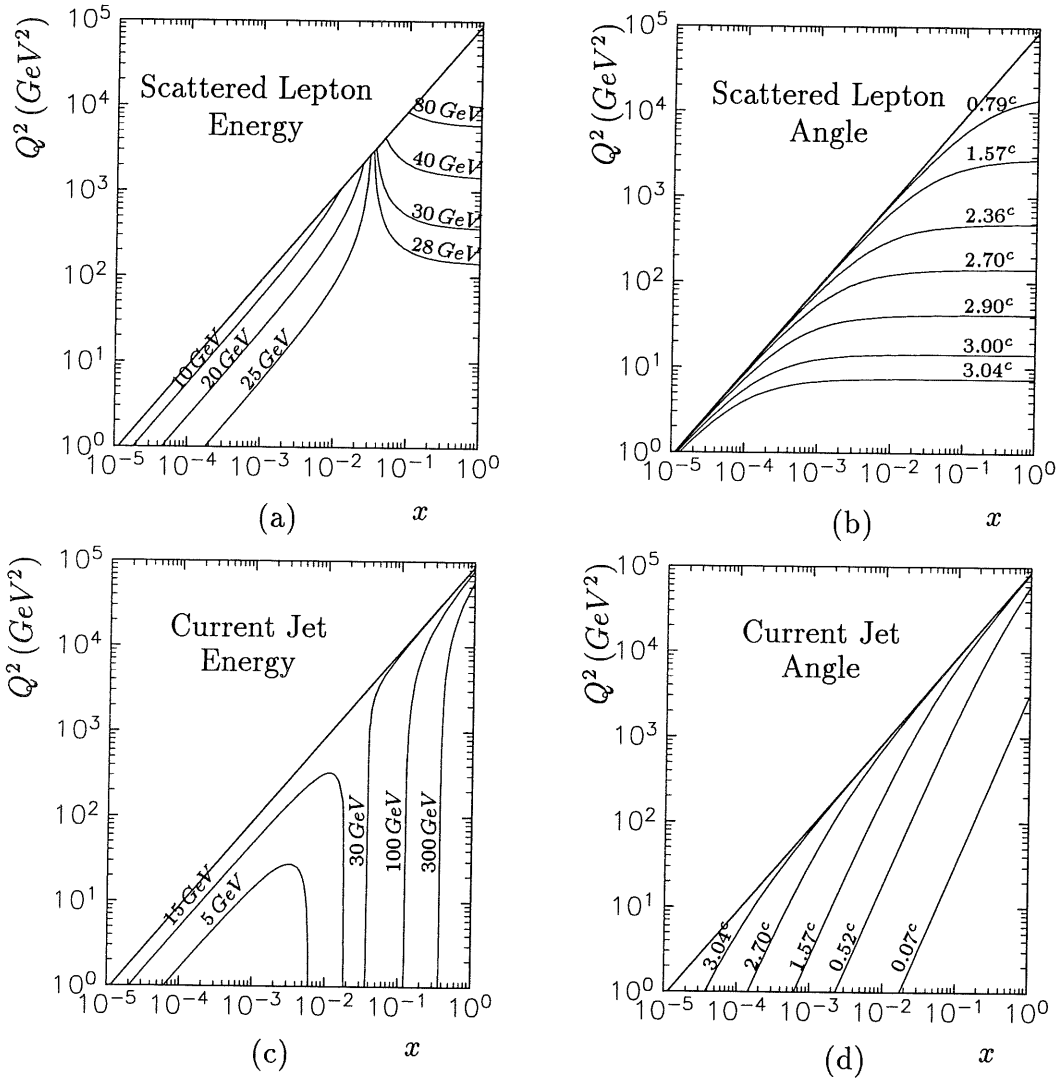


Figure 2.3: The mapping of scattered lepton and jet energies and angles onto the $x, Q^2$ plane. Lines of constant $y$ are straight lines, parallel to the kinematic limit.

of a DIS event is determined by two variables, the system is overconstrained. Thus, there exist many other methods of calculating the kinematics of a given event, including fitting and allowing for particles lost down the beam pipe in the backward direction (eg radiation of a photon from the electron) [2, 3, 4].

## 2.3 Inclusive DIS Cross Section

The cross section for the inclusive inelastic scattering of one spin-1/2 particle off another can be written as

$$\frac{d^2\sigma}{dE'd\Omega} = \frac{\alpha^2}{Q^4}\frac{E'}{E}L_{\mu\nu}W^{\mu\nu} \tag{2.14}$$

where $E$, $E'$ are the incoming and outgoing energy of the scattered particle. In the case of low $Q^2$ deep inelastic neutral current electron-proton scattering, where photon exchange dominates, $L_{\mu\nu}$ is the standard leptonic tensor as given by QED, and $W^{\mu\nu}$ parameterizes the lack of knowledge of the proton vertex. If only photon exchange is considered, the lepton tensor is symmetric, so only the symmetric terms of the hadronic tensor contribute. Demanding that the cross section is Lorentz invariant requires that $W^{\mu\nu}$ be constructed as the symmetric combinations of the only available four-vectors, the four-momenta of the exchanged boson and proton, and $g^{\mu\nu}$, the metric tensor in four-space. The four-momentum of the final state is not included because it can be constructed from the the boson and proton four-momenta. There are four possible independent symmetric combinations of these variables,

$$W^{\mu\nu} = -W_1 g^{\mu\nu} + \frac{W_2}{M^2}P^\mu P^\nu + \frac{W_4}{M^2}q^\mu q^\nu + \frac{W_5}{M^2}(P^\mu q^\nu + q^\mu P^\nu) \tag{2.15}$$

where $M$ is the proton mass, $P^\mu$ and $q^\mu$ are the proton and exchanged boson four-momenta respectively (see figure 2.1). Current conservation at the hadronic vertex,

$$q_\mu W^{\mu\nu} = q_\nu W^{\mu\nu} = 0 \tag{2.16}$$

then reduces the number of unknown parameters to two. The cross section can then be written as

$$\frac{d^2\sigma}{dxdQ^2} = \frac{4\pi\alpha^2}{xQ^4}\left(y^2 x F_1(x,Q^2) + (1-y)F_2(x,Q^2)\right) \tag{2.17}$$

where $F_1$ and $F_2$ are the 'structure functions' of the proton and $x$, $y$, and $Q^2$ are as defined in the previous section. If the effects of the weak neutral boson, the $Z^0$, are included then a third term, $(y - \frac{y^2}{2})F_3(x,Q^2)$ has to be added. This

comes from the anti-symmetric terms in the hadronic tensor which arise when the requirement of parity invariance is not included.

The above discussion of the general form of the differential cross section makes no assumption about the structure of the proton. It provides a set of experimentally measureable quantities, namely the structure functions, but there is no further predictive power in the formalism.

The parton model adds predictive power to the formalism. The model assumes that the proton consists of free point-like fermions, whose distribution in the proton is described by the parton density functions, $f_i(x, Q^2)$, which are constrained by the normalization condition that

$$\sum_i \int_0^1 dx\, x f_i(x) = 1 \tag{2.18}$$

where the sum is over the different free partons.

Since the partons are assumed to be free, the probabilities, $f_i(x)$, should depend only on the fraction of the proton's momentum carried by the parton, namely $x$. The assumption that the structure function is independent of $Q^2$ is known as 'scaling' or 'scale invariance'. The differential cross section can be written in terms of electron-parton scattering, $\frac{d\sigma^2_{eq_i}}{dxdQ^2}$, together with the probability of finding a parton in the proton.

$$\frac{d\sigma^2_{ep}}{dxdQ^2} = \sum_i \int_0^1 d\epsilon\, f_i(\epsilon) \frac{d\sigma^2_{eq_i}}{dxdQ^2} \tag{2.19}$$

The electron-parton scattering cross section can be evaluated as the elastic scattering of charged, point-like fermions,

$$\frac{d\sigma^2_{eq_i}}{dxdQ^2} = \frac{2\pi\alpha^2 e_i^2}{Q^4} \left(1 + (1-y)^2\right) \delta(x - \epsilon) \tag{2.20}$$

where $e_i$ is the charge of the struck parton and $\epsilon$ is the fraction of the proton's momentum carried by the struck parton. Inserting equation 2.20 in 2.19 gives

$$\frac{d\sigma^2_{ep}}{dxdQ^2} = \frac{4\pi\alpha^2}{xQ^4} \sum_i \int_0^1 d\epsilon \left(\frac{y^2}{2} + (1-y)\right) e_i^2 x f_i(\epsilon) \delta(x - \epsilon) \tag{2.21}$$

Comparing the terms of $y^2$ and $(1-y)$ in equations 2.17 and 2.21 shows that

$$\frac{F_2}{x} = \sum_i \int_0^1 d\epsilon\, e_i^2 f_i(\epsilon) \delta(x - \epsilon) \tag{2.22}$$

and that

$$F_2 = 2xF_1 \tag{2.23}$$

the Callan-Gross relation. This relation is a direct result of the spin-$\frac{1}{2}$ nature of the partons. The cross section is often rewritten in terms of $F_2(x,Q^2)$ and a parameter, $R$, such that $R=0$ corresponds to the validity of equation 2.23:

$$\frac{d\sigma^2_{ep}}{dxdQ^2} = \frac{2\pi\alpha^2}{xQ^4}\left(2\cdot(1-y)+\frac{y^2}{1+R}\right)F_2(x,Q^2) \tag{2.24}$$

$$R(x,Q^2) = \frac{F_2(x,Q^2)-2xF_1(x,Q^2)}{2xF_1(x,Q^2)} \tag{2.25}$$

Assuming that the partons are quarks introduces even more predictive power to the model. The proton is then considered to comprise of three 'valence' quarks, and a 'sea' of quark-antiquark pairs. If the valence quark density distributions are written as $u^p_v(x)$ for the up quarks and $d^p_v(x)$ for the down, and the sea is denoted by $f^p_s(x)$ for the quarks and $\overline{f}^p_s(x)$ for the antiquarks ($f=u,d,\ldots$ for the different flavours) then the the proton structure function can then be written as

$$\begin{aligned}\frac{F_2^{ep}}{x} &= \left(\frac{2}{3}\right)^2\left(u^p_v+u^p_s+\overline{u}^p_s\right)+\left(-\frac{1}{3}\right)^2\left(d^p_v+d^p_s+\overline{d}^p_s\right)+\left(-\frac{1}{3}\right)^2\left(s^p_s+\overline{s}^p_s\right)\\ &= \left(\frac{4}{9}\right)\left(u(x)+\overline{u}(x)\right)+\left(\frac{1}{9}\right)\left(d(x)+\overline{d}(x)\right)+\left(\frac{1}{9}\right)\left(s(x)+\overline{s}(x)\right)\end{aligned} \tag{2.26}$$

where the charges of the quarks (2/3 for the up, -1/3 for the down and strange) have been inserted, and the possibility of a large fraction of heavy qaurks (charm, bottom) in the proton has been neglected. The protons charge, isospin and strangeness constrain the parton density distributions,

$$\begin{aligned}\int_0^1 dx\left(u(x)-\overline{u}(x)\right) &= 2\\ \int_0^1 dx\left(d(x)-\overline{d}(x)\right) &= 1\\ \int_0^1 dx\left(s(x)-\overline{s}(x)\right) &= 0\end{aligned} \tag{2.27}$$

Since the proton and neutron form an isospin doublet, an analogous equation to 2.26 can be written for the neutron, but with the up-quark distribution given by the proton down-quark distribution and vice-versa i.e.

$$\frac{F_2^{en}}{x} = \left(\frac{4}{9}\right)\left(d(x)+\overline{d}(x)\right)+\left(\frac{1}{9}\right)\left(u(x)+\overline{u}(x)\right)+\left(\frac{1}{9}\right)\left(s(x)+\overline{s}(x)\right) \tag{2.28}$$

Subtracting the two equations and integrating over $x$, the Gottfried sum rule [5] is obtained

$$\int_0^1\frac{dx}{x}\left(F_2^{ep}-F_2^{en}\right) = \frac{1}{3}\int_0^1 dx\left(u-d+\overline{u}-\overline{d}\right)$$

$$= \frac{1}{3}\int_0^1 dx\left((u-\overline{u})-(d-\overline{d})\right)+\frac{2}{3}\int_0^1 dx\left(\overline{u}-\overline{d}\right)$$
$$= \frac{1}{3} \qquad (2.29)$$

if the up and down 'sea' quark distributions are the same. Other sum rules can be constructed in a similar way [6]. However, these sum rules, which also consider other possible nucleon–lepton DIS measurements, do not allow the individual parton density distributions to be obtained, only combinations of them.

Scale invariance is observed to be approximately true for $x \approx 0.3$, but variations of the structure function with $Q^2$ over a larger range of $x$ are found. This implies that the quarks are not entirely free, structureless particles. Early experiments also showed that charged particles could not entirely account for the proton's structure, when it was found that the 'momentum sum rule' was violated. This sum rule,

$$\int_0^1 dx\,(xp)(u+\overline{u}+d+\overline{d}+s+\overline{s}) = p \qquad (2.30)$$

expresses the fact that the sum of the momenta of the individual partons must be the momentum of the proton, $p$.

These problems of the parton model are overcome with quantum chromodynamics, QCD. Bosons, called gluons, are introduced into the theory to mediate the force between the quarks. In QCD, the strength of the coupling between particles, $\alpha_s(Q^2)$, is assymptotically free, that is it tends to zero as $Q^2$ tends to infinity. The violation of scaling then has a simple interpretation. As the virtuality of the probe increases, it can resolve smaller scales within the proton. Since the quark can radiate a gluon, probing with a higher $Q^2$ photon results in a higher probability for finding a softer quark at a lower $x$. Formally this is calculated using the Gribov, Lipatov, Alterelli, Parisi (GLAP) evolution equations [7]. Considering only the radiation of a single gluon from the struck quark (either in the initial or final state), the proton structure function is modified from equation 2.22 to

$$\frac{F_2(x,Q^2)}{x} = \sum_i e_i^2 \int_x^1 \frac{dy}{y} f_i(y)\left(\delta\left(1-\frac{x}{y}\right)+\frac{\alpha_s}{2\pi}P_{qq}\left(\frac{x}{y}\right)\log\frac{Q^2}{\mu^2}\right) \qquad (2.31)$$

where $P_{qq}(y)$ (a 'splitting function') represents the probability of quark radiating a gluon, reducing its momentum by a fraction $y$ and $\mu^2$ is a regularization parameter to avoid infra-red divergences. This equation is the first two terms of an expansion in terms of $\alpha_s$, which has a dependence of $(\log Q^2)^{-1}$. However, $\alpha_s$ is multiplied by a factor of $\log Q^2$ and so the series may not converge for large $Q^2$ as might have been expected from the decrease in the strength of the coupling. In order to overcome this, the parton density distribution is first redefined as a 'bare' density,

$q(y)$ and a term depending on $Q^2$,

$$\begin{aligned}\frac{F_2(x,Q^2)}{x} &= \sum_i e_i^2 \int_x^1 \frac{dy}{y}\left(q(y)+\Delta q(y,Q^2)\right)\delta\left(1-\frac{x}{y}\right)\\ &= \sum_i e_i^2\left(q(x)+\Delta q(x,Q^2)\right)\end{aligned} \tag{2.32}$$

where

$$\Delta q(x,Q^2) = \frac{\alpha_s}{2\pi}\log\left(\frac{Q^2}{\mu^2}\right)\int_x^1 \frac{dy}{y}\,q(y)P_{qq}\left(\frac{x}{y}\right) \tag{2.33}$$

The bare distribution function is unknown. However, by differentiating equation 2.33 with respect to $Q^2$, the change of the parton distribution functions can be calculated. To calculate the full equations, the possibility of a gluon spilting into a quark or gluon pair need to be included (see figure 2.4). The splitting

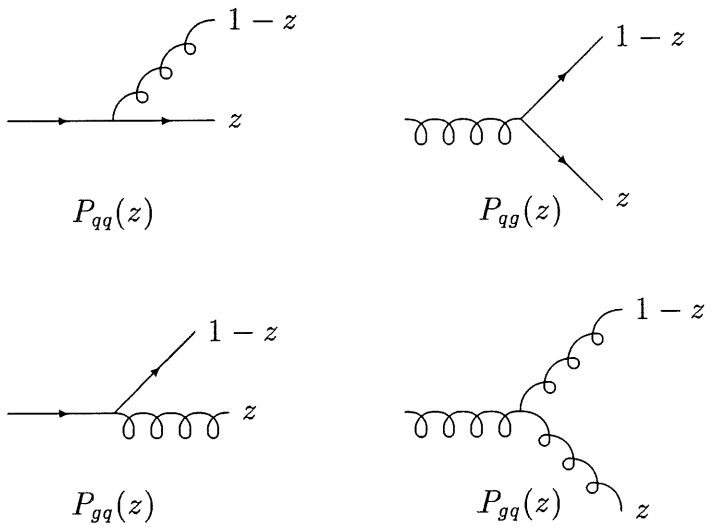


Figure 2.4: The Feynmann diagrams corresponding to the splitting functions.

functions thus calculated are divergent as the fraction of the emitted parton's momentum ($z$) tends to 0. However, the inclusion of virtual corrections (figure 2.5) cancels these divergences and the full equations can be written as

$$\begin{aligned}\frac{dq_i(x,Q^2)}{d\log Q^2} &= \frac{\alpha_s}{2\pi}\int_x^1 \frac{dy}{y}\left(q_i(y,Q^2)P_{qq}\left(\frac{x}{y}\right)+g(y,Q^2)P_{qg}\left(\frac{x}{y}\right)\right)\\ \frac{dg(x,Q^2)}{d\log Q^2} &= \frac{\alpha_s}{2\pi}\int_x^1 \frac{dy}{y}\left(\sum_i q_i(y,Q^2)P_{gq}\left(\frac{x}{y}\right)+g(y,Q^2)P_{gg}\left(\frac{x}{y}\right)\right)\end{aligned} \tag{2.34}$$

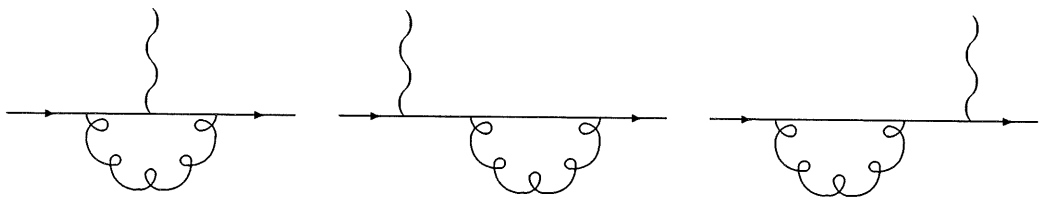

Figure 2.5: Virtual QCD corrections required in the calculation of the splitting functions.

The equations 2.34 are known as the leading-log($Q^2$) equations. By taking moments it is possible to show that taking the leading term in $\alpha_s \log Q^2$ is equivalent to summing up a ladder of parton emissions from the initial bare parton with the virtualities of the partons being strongly ordered. Referring to figure 2.6, this implies that $k_{\perp 1}^2 \ll k_{\perp 2}^2 \ll \cdots \ll k_{\perp i}^2 \ll \cdots \ll Q^2$. Although only gluons are shown in the ladder, the evolution equations include the possibility of quarks.

Thus, given a set of parton density distributions which describe the proton structure function, $F_2(x, Q^2)$, (equation 2.26) at a given $Q_0^2$ for all $x$, they can be evolved to higher $Q^2$ values to predict the proton structure function. Since the GLAP equations are now known to next to leading order (NLO, terms of the form $\alpha_s^n \log^{n-1} \frac{Q^2}{\mu^2}$), this can be done very accurately. However, since the parton density distributions are only known for a small range of $x$, any extrapolation to low $x$ will require theoretical input that will determine the shape of the structure functions at small $x$. Figure 2.7 shows the measured values of $F_2^{\mu p}$ from both the NMC experiment [8] and the BCDMS experiment [9], along with the prediction of one of the NLO parton density distribution parameterizations that has been fitted to the data including the GLAP evolution. Only data at $Q^2 > 5\,GeV^2$ is shown, as this is the $Q_0^2$ taken for the start of the GLAP evolution for the parton density distributions.

The behaviour of the parton distribution functions as $x \to 1$ is usually taken to be [10]

$$f_i(x) \sim (1-x)^\eta \tag{2.35}$$

The low $x$ behaviour is traditionally considered as the Regge limit, ($x = \frac{Q^2}{2P\cdot q} \to 0$ at fixed $Q^2$, implying that $P \cdot q \sim s_{\gamma P} \to \infty$). In this limit, the valence quark distributions are expected to have the form

$$x q_v \sim x^{\frac{1}{2}} \tag{2.36}$$

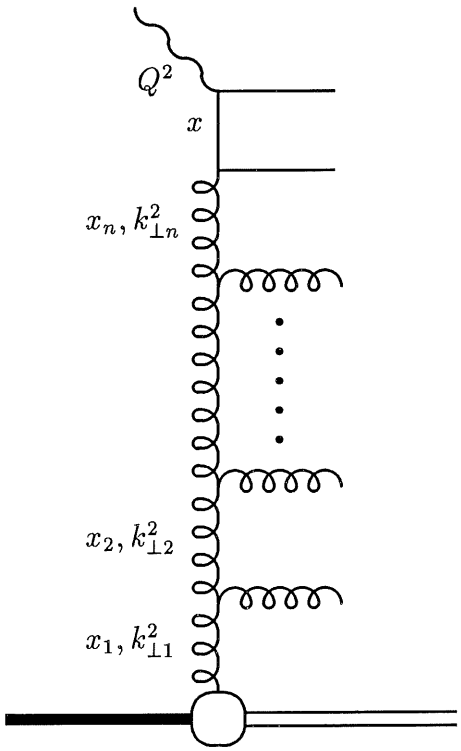


Figure 2.6: Diagram of the gluon ladder contribution the proton structure function. The GLAP evolution corresponds to strongly ordered virtuality along the ladder, $k^2_{\perp 1} \ll k^2_{\perp 2} \ll \cdots \ll k^2_{\perp i} \ll \cdots \ll Q^2$. The double leading logarithm demands in addition strong ordering of the longitudinal momenta along the ladder, $x_1 \gg x_2 \gg \cdots \gg x_i \gg \cdots x$. The Lipatov evolution equation relaxes the strong ordering in $k_\perp$ and demands only ordering in $x$.

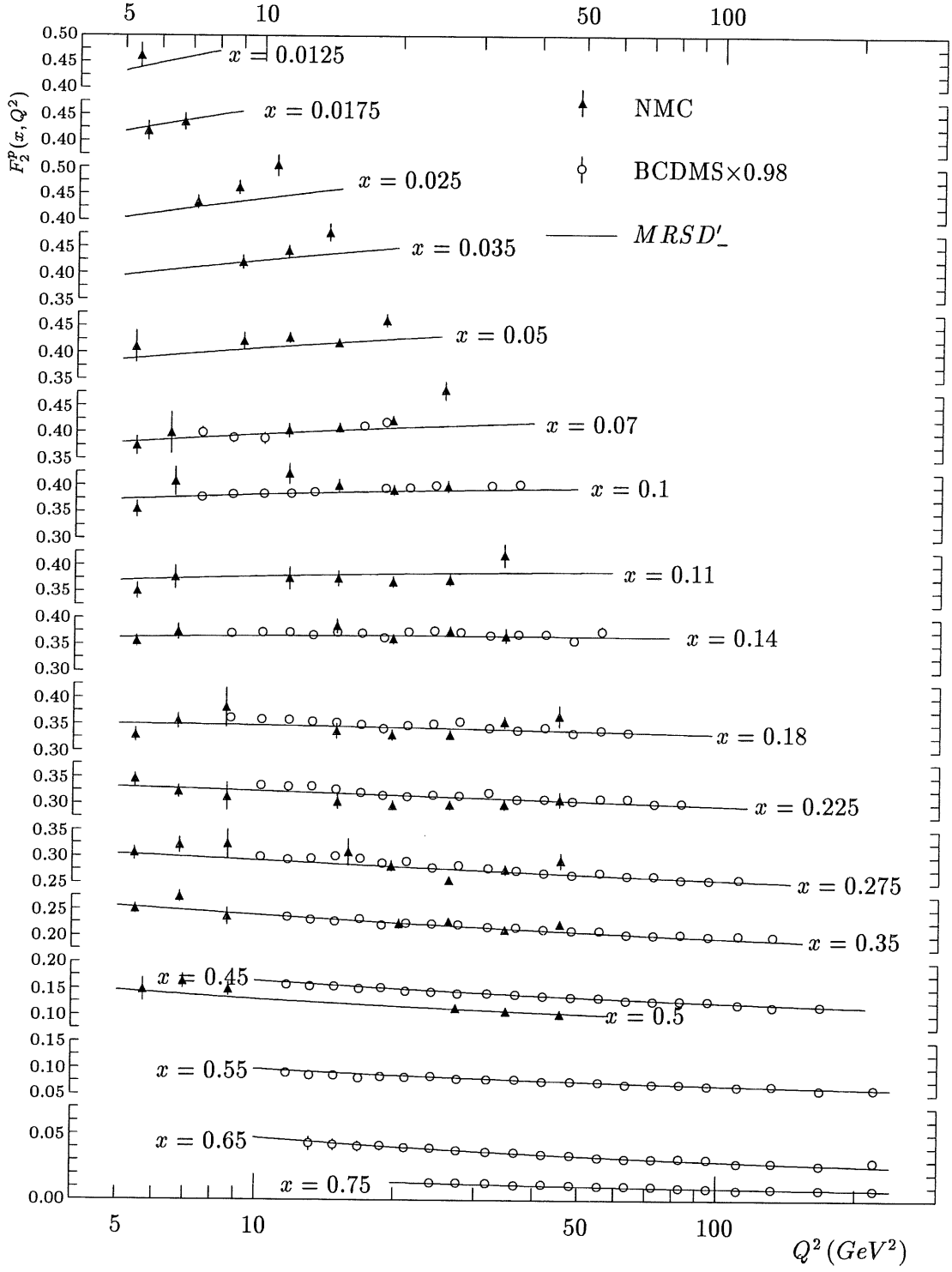


Figure 2.7: $F_2^p(x, Q^2)$ from NMC and BCDMS for $Q^2 > 5\,GeV^2$. Also shown is the prediction using the $MRSD'_-$ parton density distributions. In the fit of the $MRS$ distributions it was found that the BCDMS data needed to be scaled by a factor of 0.98.

and the sea and gluon distributions to tend to

$$xg, xq_s \sim x^0 \tag{2.37}$$

However recent work has suggested that this might not be the case. Owing to the high probability of soft gluon emission, it might be expected that the gluonic terms in the evolution equations would dominate at smaller values of $x$. If this is the case, then the splitting function, $P_{gg}(z)$ approximates to $\frac{6}{z}$. Equation 2.34 then becomes

$$\begin{aligned} \frac{dg(x,Q^2)}{d\log Q^2} &= \frac{\alpha_s}{2\pi}\int_x^1 \frac{dy}{y} P_{gg}\left(\frac{x}{y}\right) g(y,Q^2) \\ &= \frac{3\alpha_s}{x\pi}\int_x^1 \frac{dy}{y} y g(y,Q^2) \end{aligned} \tag{2.38}$$

giving

$$\frac{dxg(x,Q^2)}{d\log Q^2} = \frac{3\alpha_s}{\pi}\int_x^y \frac{dy}{y} y g(y,Q^2) \tag{2.39}$$

It can be seen that this gives rise to terms of order $\alpha_s \log\left(\frac{1}{x}\right)\log Q^2$, which for small $x$ and large $Q^2$ may be of the order of unity. In this case, the ladders summed are those with both strongly ordered transverse and longitudinal momenta, with reference to figure 2.6, $k_{\perp 1}^2 \ll k_{\perp 2}^2 \ll \cdots \ll k_{\perp i}^2 \ll \cdots \ll Q^2$ and $x_1 \gg x_2 \gg \cdots \gg x_i \gg \cdots \gg x$. Assuming a fixed $\alpha_s$, the solution to equation 2.39 is

$$xg(x,Q^2) \sim exp\left(2\left(\frac{3\alpha_s}{\pi}\log\left(\frac{1}{x}\right)\log\left(\frac{Q^2}{Q_0^2}\right)\right)^{\frac{1}{2}}\right) \tag{2.40}$$

This is known as the double-leading log approximation (DLLA).

Whilst the DLLA is valid at large $Q^2$, at smaller values of $Q^2$, the terms proportional to $\alpha_s \ln\frac{1}{x}$ will dominate (the leading log $1/x$, LL$(1/x)$ approximation). This then requires that the ladder diagrams calculated allow for all values of $Q^2$ in the evolution, whilst retaining the strong ordering in longitudinal momenta. In relaxing the constraint of strong ordering of the virtuality of the partons along the ladder, one has to work with the unintegrated gluon distribution, $f(x,k^2)$, defined by

$$xg(x,Q^2) = \int_0^{Q^2} \frac{dk^2}{k^2} f(x,k^2) \tag{2.41}$$

In the LL$(1/x)$ approximation, $f(x,k^2)$ satisfies the Balitzkij–Fadin–Kuraev–Lipatov (BFKL) equation [11],

$$-x\frac{df}{dx} = \frac{3\alpha_s(k^2)}{\pi}k^2\int_{k_0^2}^{\infty}\frac{dk'^2}{k'^2}\left(\frac{f(x,k'^2)-f(x,k^2)}{|k'^2-k^2|} + \frac{f(x,k^2)}{(4k'^4+k^4)^{\frac{1}{2}}}\right) \tag{2.42}$$

where $k_0^2$ is a cut-off to avoid infra-red divergences when the coupling constant is allowed to vary with $k^2$ (it is allowed to 'run'). The equation can be solved analytically for a fixed $\alpha_s$ and $k_0^2 = 0$, and the solution has the form

$$f(x, k^2) \sim x^{-\lambda} \tag{2.43}$$

where

$$\lambda = \frac{12 \ln 2}{\pi} \overline{\alpha}_s \tag{2.44}$$

where $\overline{\alpha}_s$ is the fixed value of the coupling constant. Allowing the coupling constant to run introduces a cut-off dependence of $\lambda$, but it can be shown that [12]

$$\frac{3.6}{\pi} \alpha_s k_0^2 \leq \lambda \leq \frac{12 \ln 2}{\pi} \alpha_s k_0^2 \tag{2.45}$$

$\lambda$ potentially has a large value, up to 0.5, giving very different small $x$ behaviour from the traditional Regge like behaviour.

## 2.4 Parton Density Distribution Functions

The nucleon structure functions are measured in many experiments using muon, electron and neutrino scattering off protons and nuclei. The extraction of set of a parton density distribution functions from these data then requires theoretical assumptions. A brief review of some of the newer parton density distribution analyses is given below.

### 2.4.1 The MRS parton distributions

In order to give an estimate of the range of possible values for the parton density distribution functions, two different sets of MRS (Martin, Roberts, Stirling) distributions have been calculated [13], one with the singular 'Lipatov' behaviour of the gluon density function, $MRSD'\_^2$, and one with the traditional flat behaviour, $MRSD_0'$. The density distribution functions are parameterized at a fixed $Q_0^2$ $(4\,GeV^2)$ such that $Q_0^2$ is sufficiently large for perturbative calculations.

The NMC experiment has measured the Gottfried sum rule [14] (equation 2.29) and found a result significantly different from one third, suggesting that the up

[2]The prime distinguishes the functions from the earlier set of MRS partons which were calculated using preliminary data

and down sea parton distributions are different. In the MRSD parameterizations this difference is parameterized as

$$x(\overline{u} - \overline{d}) = Ax^{\frac{1}{2}}(1-x)^{\eta_{sea}} \tag{2.46}$$

The strange sea is determined using the CCFR dimuon data [15]. This reaction, $\nu N \rightarrow \mu^+\mu^- X$, is dominated by the QCD sub-process $\nu s \rightarrow \mu^-(c \rightarrow \mu+)$. Motivated by the rate for this reaction, the strange sea is taken to be suppressed by a factor of two with respect to the up and down sea distributions.

The gluon distribution is difficult to determine because DIS data relies on the probe coupling to a charged constituent in the target. However, the gluon density has been measured in the WA70 experiment [16]. This uses events with photons of large transverse momentum produced by $pp \rightarrow \gamma X$, for which the dominant QCD sub-process is $qg \rightarrow \gamma q$. This data determines the gluon content at $x \sim 0.4$. The momentum sum rule can then be used to extrapolate this value in $x$.

Neglecting the (small) charm and bottom contributions leaves four density distributions that can be extracted from the data, the up and down valence distributions, the gluon distribution and the sum of the up and down sea distributions. These are parameterized by the form

$$xf_i(x, Q_0^2) = A_i x^{\alpha_i}(1-x)^{\beta_i}(1 + \gamma_i x^{\frac{1}{2}} + \delta_i x) \tag{2.47}$$

It is assumed that the gluon density distribution drives the sea quark distributions, and the same value of $\alpha_i$ is used. This then leaves 15 free parameters to be fitted to the data, using the NLO GLAP evolution equations to evolve the parton distributions to higher values of $Q^2$. The parton density distributions are compared in figure 2.8.

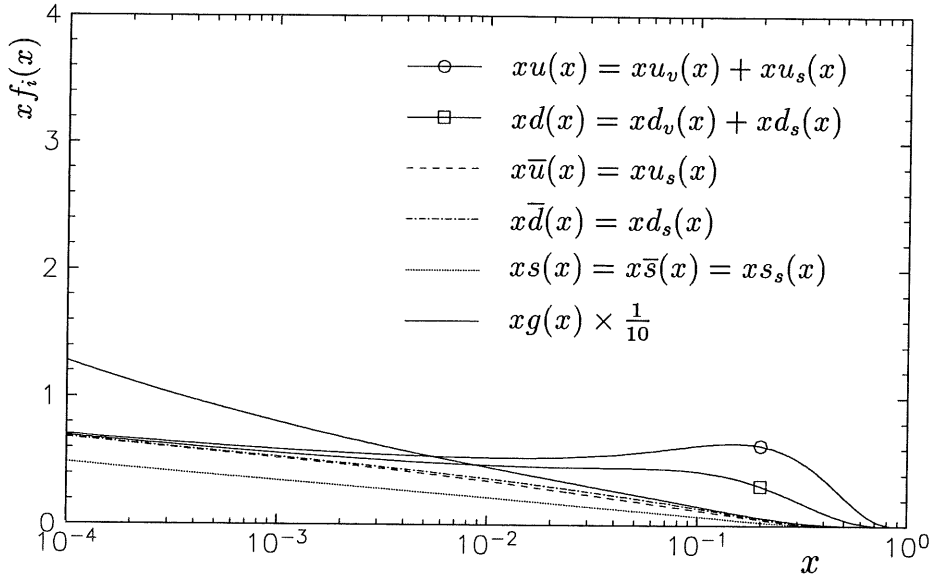


(a)

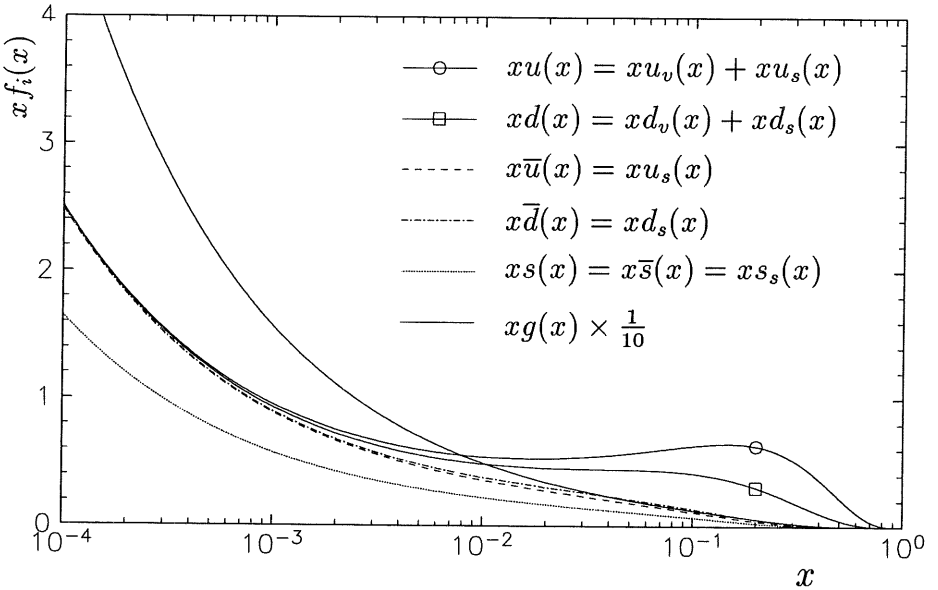


(b)

Figure 2.8: The MRS parton distributions at $Q^2 = 20\,GeV^2$. Figure (a) shows the $MRSD'_0$ distribution for which $xg(x) \sim x^0$ as $x \to 0$, figure (b) the singular $MRSD'_-$ for which $xg(x) \sim x^{-\frac{1}{2}}$ as $x \to 0$. The 'sea' quark distributions are driven by the gluon distribution and have the same $x$ dependence. Note the change of scale for the gluon distribution, $xg(x)$.

### 2.4.2 The CTEQ parton distributions

The CTEQ (Coordinated Theoretical/Experimental Project on QCD Phenomenology and Tests of the Standard Model) collaboration have also fitted a set of parton density distributions [17] to basically the same set of data as the MRS group. In this analysis, the sea quark distributions were unconstrained, resulting in a larger number of free parameters (over 30). The CTEQ1MS distributions include the 'Lipatov' ($x^{-0.5}$) behaviour of the gluon distribution, the CTEQ1M include the 'Regge' $x$ dependence. The sea quarks are not forced to have the same behaviour as the gluon distribution, and relatively little difference is seen between the two sets of distributions (see figure 2.9). The other major difference between the CTEQ and MRS distributions is in the treatment of the strange sea, with the CTEQ distributions having a much higher fraction of strange quarks. The CTEQ strange sea distribution is in reasonable agreement with estimates from DIS data, but it appears to overshoot the CCFR di-muon data [6].

### 2.4.3 The GRV parton distributions

The parton distributions of Glück, Reya and Vogt (GRV) [18] are an attempt at generating the parton distributions without assuming their shape at small $x$. The idea was to take a set of parton distributions for only the valence quarks at a very small $Q_0^2$ ($0.3\,GeV^2$) and to evolve the distributions using the double leading-log formulae. The distributions are then fitted to the MRS valence parton distributions to give a prediction for all $x$. Unfortunately, in order to describe the $x$ shape of $F_2^{\mu p}$ data and to account for the WA70 data, it was found necessary to input some intrinsic gluon and sea quark contributions at the initial conditions.

The GRV parton distribution functions are shown in figure 2.10. It can be seen that they rise steeply as a function of $x$, similarly to the $MRSD'\_$ distributions. This rise is due to the very small $Q^2$ at which the evolution is started. With $Q_0^2 = 0.3\,GeV^2$, and $Q^2 = 20\,GeV^2$, the double leading log approximation (equation 2.40) simulates a gluon distribution which rises as $x^{-0.4}$ [19].

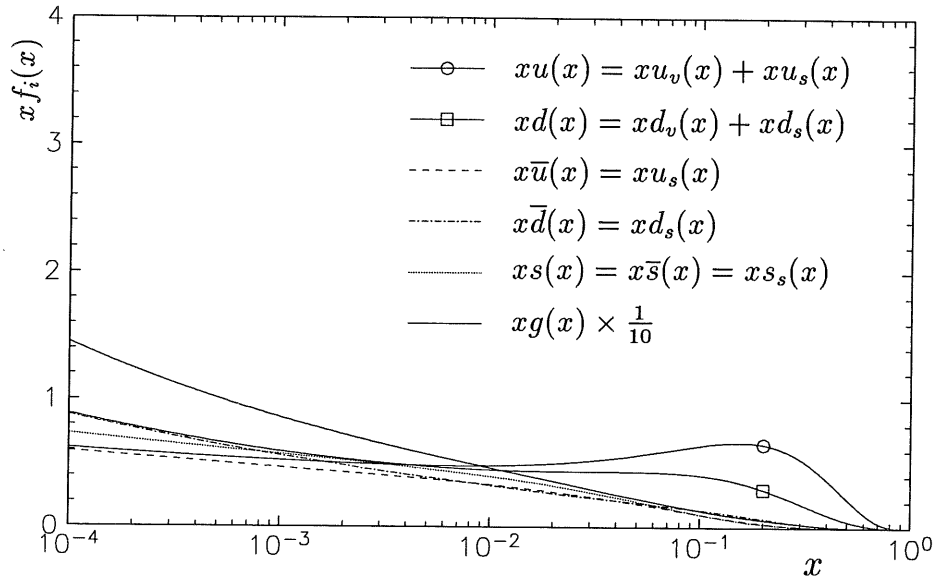


(a)

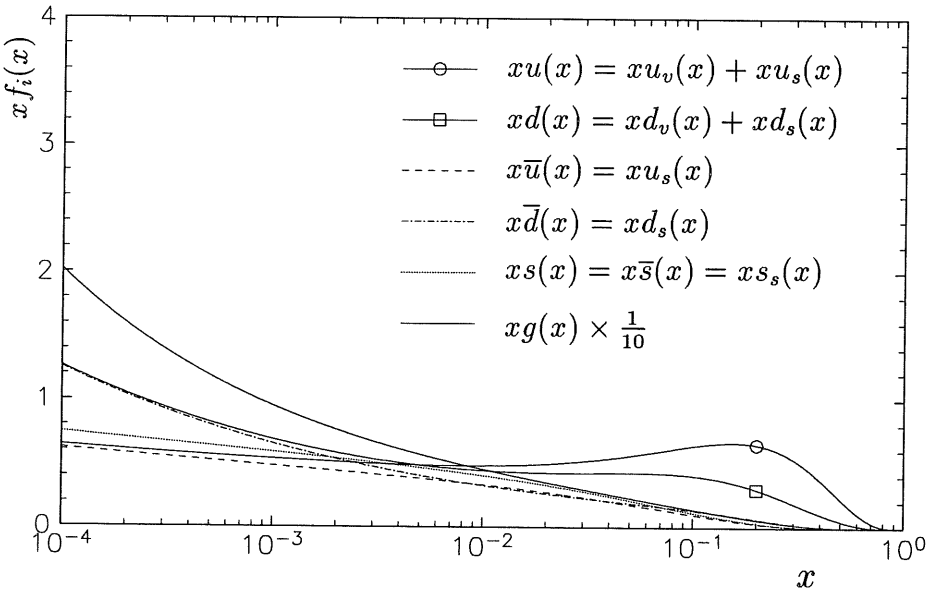


(b)

Figure 2.9: The CTEQ parton distributions at $Q^2 = 20\,GeV^2$. Figure (a) shows the $CTEQ1M$ distribution for which $xg(x) \sim x^0$ as $x \to 0$, figure (b) the singular $CTEQ1MS$ for which $xg(x) \sim x^{-\frac{1}{2}}$ as $x \to 0$. The 'sea' quark distributions are freely fitted and not forced to have the same $x$ dependence as the gluon. Note that scale change for the gluon distribution, $xg(x)$.

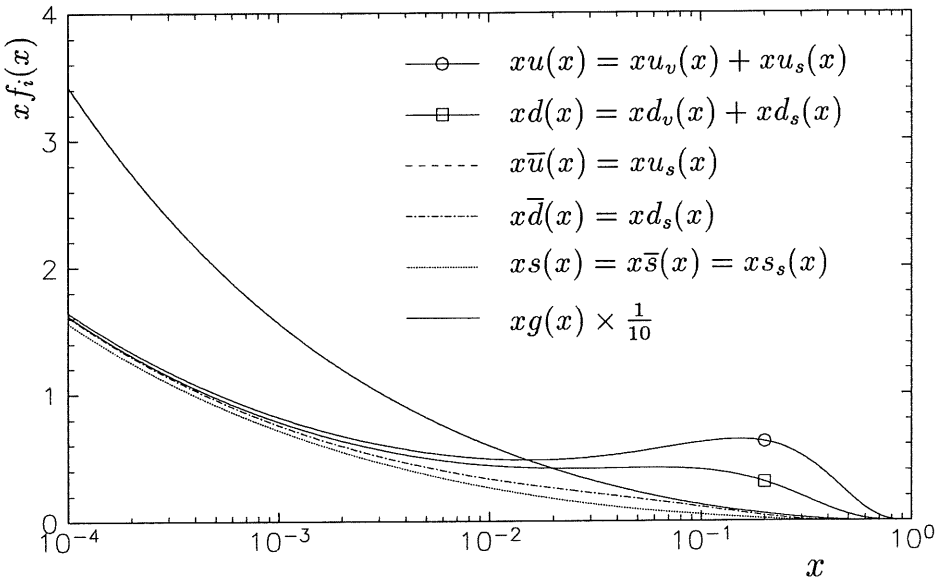


Figure 2.10: The GRV parton distributions at $Q^2 = 20\,GeV^2$. The singular behaviour of the parton distributions is generated from evolution of the DLLA equations from a very small initial $Q^2$. Note the change of scale for the gluon distribution, $xg(x)$.

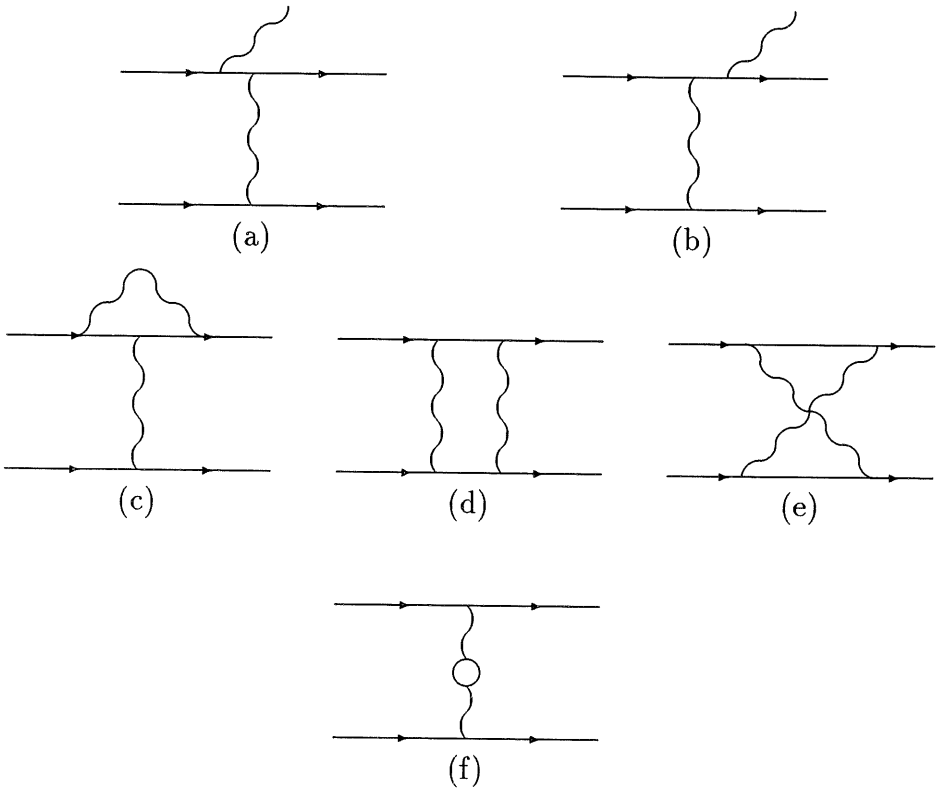


Figure 2.11: $\mathcal{O}(\alpha_{EM}^3)$ corrections to the DIS differential cross section. Figures (a) and (b) show initial (final) state radiation of a photon from either the electron or quark (bremsstrahlung). Figures (c)–(f) show the virtual corrections.

## 2.5 QED Radiative Corrections

So far, only QCD effects have been considered. However, the cross section derived in section 2.3 assumed single photon exchange, with no radiation from the lepton. If the electron is used to determine the kinematics of an event, the measured cross section is not the true, Born, cross section, but the radiative cross section. To order $\alpha_{EM}^3$, corrections to the measured cross section include virtual corrections to the propagator, but are dominated by the emission of a photon by the electron (see figure 2.11). In reconstructing the kinematics of an event from the scattered electron, it is assumed that the incident energy of the electron is the beam energy. This is no longer true in the case of initial state radiation. The radiative corrections have to take into account the migrations of events between different bins of $x$. The corrections increase as the energy of the scattered electron is reduced (going to higher calculated $y$). This is easily understood because if the scattered

electron has an energy close to the beam energy, then kinematically it could not have radiated a photon.

In this analysis, the event generator DJANGO [20] is used for the generation of DIS events with full electro-weak corrections of order $\alpha$. The event generation is done in two steps, firstly HERACLES [21] is used to generate events of the form $ep \rightarrow e'X(\gamma)$ at the parton level, and then LEPTO [22] is used for the hadronization of the partons. The bremsstrahlung of a photon from the lepton is split into two parts to avoid problems with the divergence of the cross section due to the emission of soft photons. For soft photon emission, where the energy of the radiated photon is much less than the experimental resolution (approximately $10\,MeV$), the cross section is calculated analytically and used to correct the Born cross section. For harder photon emission, the cross section is split into four parts corresponding to collinear emission of a photon from the electron in the initial or final state, emission of a photon from the quark line, and the QED Compton (scattering of the electron from an almost real photon collinear with the quark). The corrections as calculated from DJANGO have been compared with other analytical calculations and found to be in good agreement [23].

## 2.6 Photoproduction

The cross section for electron proton scattering is dominated by photoproduction, the scattering of a nearly real photon off the proton. As well as having a very large cross section, there is a significant probability that particles from an interaction could 'fake' an electron in the H1 detector. An understanding of photoproduction is therefore required to fully control the level of background events in a DIS event sample.

Photoproduction can be divided into two classes of events, soft and hard. Soft processes are those in which there is only a small transfer of transverse momentum between the proton and photon, which means that perturbative QCD cannot be used. The events can however be described using the VDM (vector dominance model) of the photon, in which the photon forms a vector meson ($\rho, \omega, \phi, \ldots$) which then interacts with the proton. For this analysis, the RAYVDM [24] Monte-Carlo generator was used to generate soft events.

In hard photoproduction, there is a large transverse momentum transfer, and calculations can be made using perturbative techniques. The sub-processes involved in hard photoproduction (see figure 2.12) include the direct coupling of the photon to the proton ($\gamma$ gluon fusion, $\gamma g \rightarrow q\overline{q}$, and QCD Compton $\gamma q \rightarrow qg$) and resolved processes in which the the photon is considered to have hadronic

structure, and one of the partons in the photon interacts with the proton. The latter category of events gives rise to a photon structure function. In calculating the cross section for hard processes, a cut-off in transverse momentum is required to prevent the cross section diverging. In this analysis, the PYTHIA [25] Monte-Carlo is used to generate hard photoproduction processes.

## 2.7 Summary

The proton structure function, $F_2^p(x, Q^2)$, is well measured for $x > 10^{-2}$ at $Q^2 = 5.5\,GeV^2$. Figure 2.13 shows the latest DIS results from the NMC and BCDMS experiments at this scale. As has been pointed out in this chapter, the substantial increase in the centre of mass energy of $ep$ collisions at HERA means that genuinely deep inelastic measurements ($Q^2 > 4\,GeV^2$) are possible in the new low $x$ region of $10^{-4} < x < 10^{-2}$. In this region there are exciting theoretical suggestions that new QCD phenomena, associated with high gluon densities, may be visible in the proton structure. In the following chapters, a first measurement of $F_2^P(x, Q^2)$ in this new low $x$ region is presented.

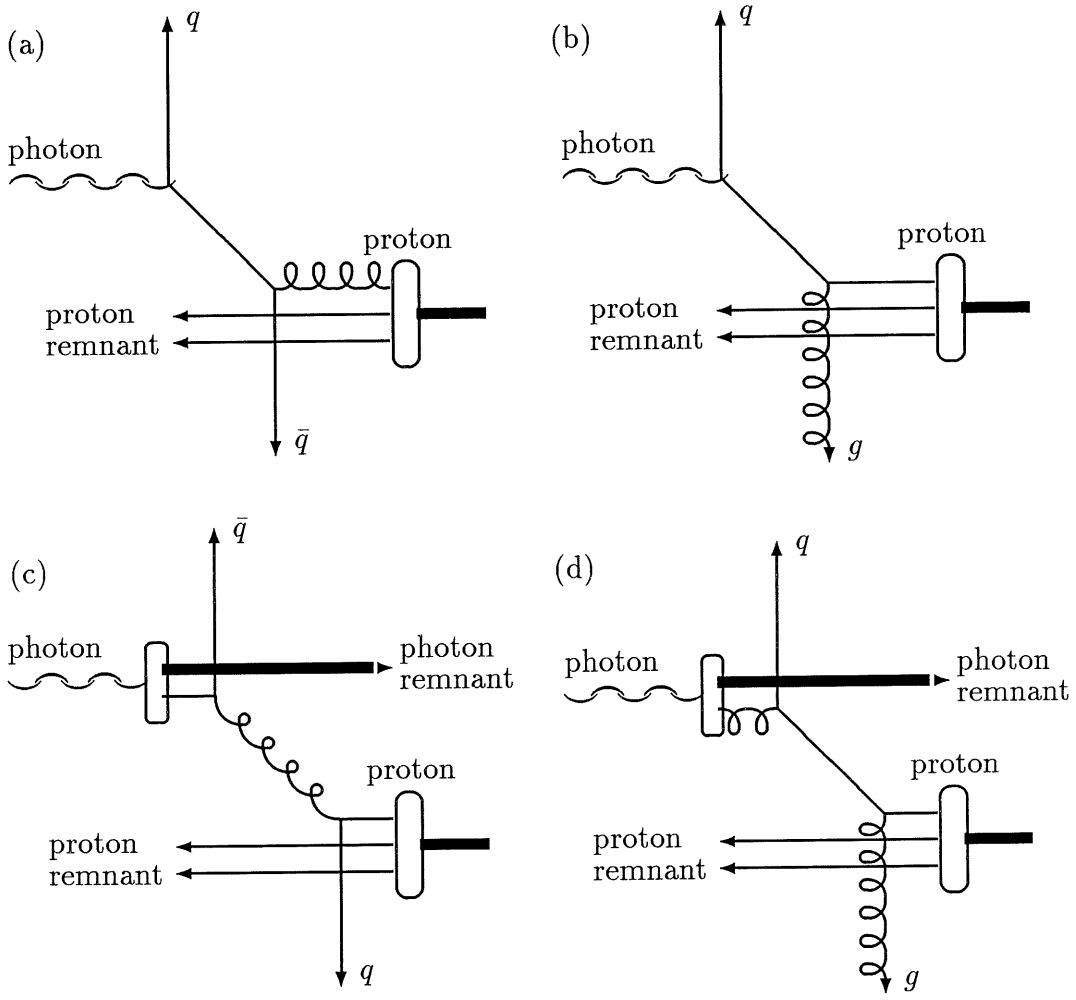


Figure 2.12: Some hard photoproduction sub-processes. (a) Photon-gluon fusion, (b) QCD Compton, (c) and (d) resolved processes.

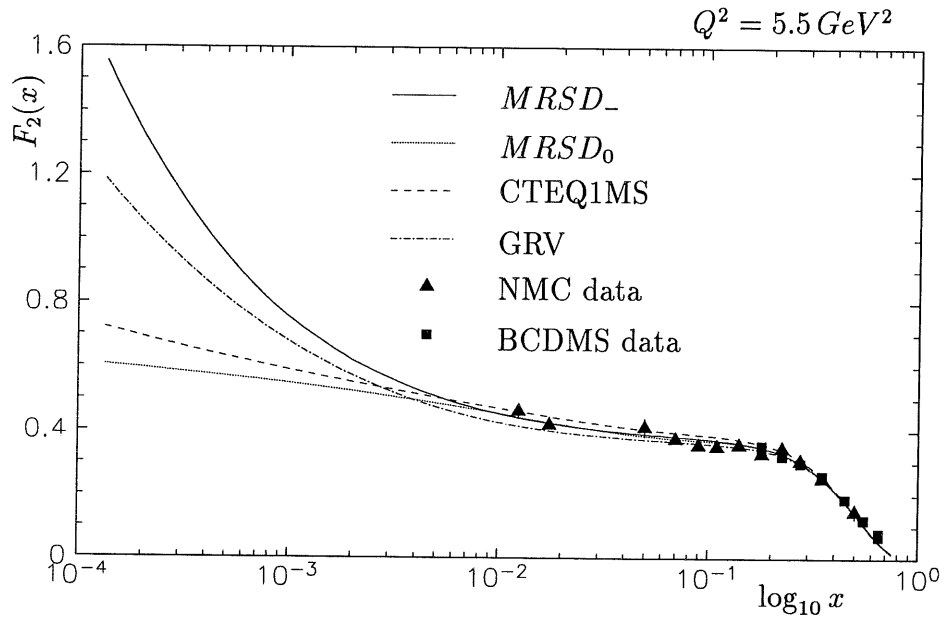


Figure 2.13: Theoretical predictions for $F_2(x, Q^2)$ at $Q^2 = 5.5\,GeV^2$ compared with NMC and BCDMS data. Whilst the structure function measurements constrain the parameterizations at high $x$, the distributions vary widely at low $x$.

# Chapter 3

# HERA and the H1 Detector

## 3.1 The HERA Machine

The HERA machine is designed to accelerate bunches of electrons to 30 $GeV$ and bunches of protons to 820 $GeV$. Owing to their different rest masses, the particles have to be accelerated and stored in separate rings. The rings are situated in the same tunnel, and brought together at four interaction points. Some of the design parameters of the machine, and the status of HERA during autumn 1992 are shown in table 3.1.

| | Design | Autumn 1992 |
|---|---|---|
| Electrons | | |
| Beam energy ($GeV$) | 30 | 26.7 |
| Number of bunches | 210 | 10 |
| Current per bunch ($\mu A$) | 290 | 280 |
| Protons | | |
| Beam energy ($GeV$) | 820 | 820 |
| Number of bunches | 210 | 10 |
| Current per bunch | 760 | 200 |
| Global | | |
| Luminosity ($cm^{-2}s^{-1}$) | $1.5 \cdot 10^{31}$ | $3.0 \cdot 10^{29}$ |
| Integrated luminosity ($nb^{-1}$ years$^{-1}$) | $10^5$ | 32 |

Table 3.1: A comparison of the design parameters of the HERA machine and those achieved in the autumn of 1992.

Of the $2 \times 10$ bunches, only $2 \times 9$ were paired such that they collided in the interaction region. The other bunches (one electron and one proton bunch), known as 'pilot' bunches, were used to study the backgrounds due to the beam particles hitting the beam pipe (beam-wall interactions) and residual gas particles (beam-gas interactions).

Both beams are small in transverse size (of the order of $0.3\,mm \times 0.1\,mm$). The electron bunches had a full width at half maximum (FWHM) of approximately $10\,mm$. The length of the interaction region was therefore determined by the length of the proton bunches (FWHM $\approx 200\,mm$). The proton bunch length is controlled using $52\,MHz$ and $208\,MHz$ RF systems, but during 1992, the latter was not routinely used. Unfortunately, in compressing the proton bunches, some of the tails of the bunches formed small secondary bunches (satellite bunches), $8\,ns$ from the main bunch.

## 3.2 Overview of the H1 detector

The H1 detector is a general purpose detector consisting of a mixture of tracking chambers and calorimetry. Some of the major concerns for the detector design were:

- A high efficiency for electron identification and a high resolution is required for studies of deep inelastic neutral current physics.
- For charged current analysis the production of a neutrino must be inferred from 'missing' energy that is not detected, requiring a high degree of hermeticity as well as good energy measurement resolution.
- Tracking is required to assist in particle identification, to study energy flow and to compliment calorimetry by accurately measuring the momentum of soft charged particles.
- Muon identification is important in searches for the decay of both heavy flavour mesons as well as of many exotic particles of interest at HERA.
- The high boost of the centre of mass of collisions necessitates an asymmetric detector.
- The short interval between colliding bunches ($96\,ns$) and high rates from proton induced background require sophisticated triggering. Background rejection must occur as early as possible in the data chain to limit the dead time of the experiment.

The detector is shown in figure 3.1. The liquid argon (LAr) calorimetry provides hermetic coverage for particle detection from $0.07^c$ (4°) to $2.7^c$ (155°). The angular coverage of the detector is increased to $0.01^c$ (0.7°) in the forward region by the plug calorimeter and in the backward region to $3.04^c$ (174°) by the backward electromagnetic calorimeter (BEMC). Inside the calorimeters, the interaction region is surrounded by an array of drift chambers for momentum measurement and proportional chambers for triggering. A superconducting coil, situated outside the calorimeter, provides a magnetic field of $1.15T$. This field is highly uniform over the H1 tracking volume, deviating at most by 4.5% [27]. The iron return yoke of the magnet is instrumented with streamer tubes for muon detection. In the forward region this is supplemented by a series of drift chambers and a toroidal magnet. Luminosity measurement is provided by a photon detector and an electron tagger at very large angles (ie very small angles with respect to the electron direction) situated at approximately $100\,m$ along the beam line.

## 3.3 Tracking

A drift chamber consists of many drift cells. Each cell has a set of anode ('sense') wires, separated by field wires, in the middle of cathode wires or planes. The electrostatics of the cell are chosen such that there is a uniform electric field across the cell. When a charged particle passes through the cell, it ionizes atoms of the gas filling the chamber. The ions drift towards the cathodes, the electrons towards the sense wires. In the vicinity of the sense wires, the field strength increases and the electrons gain sufficient energy to further ionize the gas, amplifying the signal that is collected on the sense wire. There is then a direct mapping of the time taken for the electrons to drift to the wire and the distance from the wire to the path of the particle. The charge deposited on the wire is proportional to the amount of initial ionization produced by the particle, which in turn is dependent on the velocity of the particle. Low velocity particles can then be distinguished by comparing the total charge deposited along the length of a track and the particles momentum ($dE/dx$ measurement).

In H1, the sense wires are read out via flash digital to analogue converters (FADC) [26], with a sampling frequency of $104\,MHz$. This allows the time of arrival of the first electrons to be determined to an accuracy of a few nanoseconds, resulting in a precision in the drift distance of about $200\,\mu m$. Owing to the symmetry of the cells, there remains an ambiguity as to which side of the wire the particle passed ('drift sign ambiguity'). This is overcome by staggering the sense wires about the nominal mid-point of the cell. By using resistive wire and reading out both ends of the sense wire, the distance from the end of the wire to the point at which the ionization arrived can be calculated from the ratio

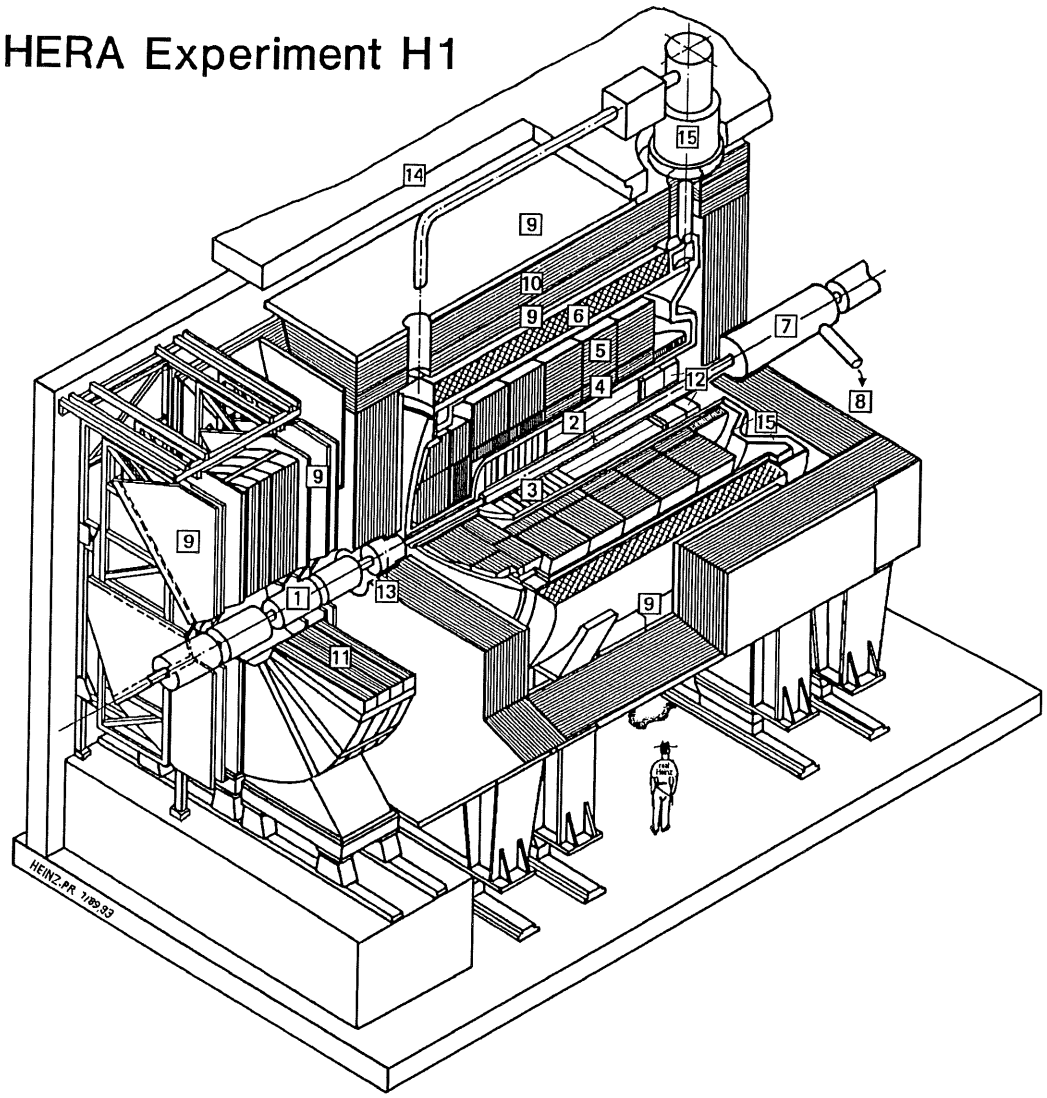


[1] Beam pipe and beam magnets
[2] Central track detector
[3] Forward track detector
[4] Electromagnetic calorimeter
[5] Hadronic calorimeter
[6] Super conducting coil ($1.2T$)
[7] Compensating magnet
[8] Helium cryogenics
[9] Forward muon chambers
[10] Instrumented iron
[11] Forward muon toroid magnet
[12] Backward electromagnetic calorimeter
[13] Plug calorimeter
[14] Concrete shielding
[15] Liquid argon cryostat

Figure 3.1: A cut away view of the H1 detector. [4] and [5] are cold, liquid argon calorimeters, whilst [12] and [13] are warm.

of the charges at each end ('charge division'). The resolution on this co-ordinate is typically of the order of 1% of the sense wire length.

Any particle going through a multi-wire proportional chamber (MWPC) passes through a region close to the wire in which the electric field is very high and the amplification occurs. Either the cathodes or anodes may be read out. Due to the short maximum drift distance, the signal arrives very shortly after the particle traverses the chamber, of the order of tens of nanoseconds, making the chambers useful for triggering.

The H1 tracking system (shown in figure 3.2) consists of the forward track detector (FTD) covering the angular range from $0.09^c$ (5°) to $0.44^c$ (25°), the central track detector (CTD), covering the range from $0.44^c$ to $2.7^c$ (155°) and the backward proportional chamber (BPC) which covers from $2.7^c$ to $3.04^c$ (174°). Both the FTD and CTD consist of a mixture of drift chambers for track reconstruction and multi-wire proportional chambers for triggering.

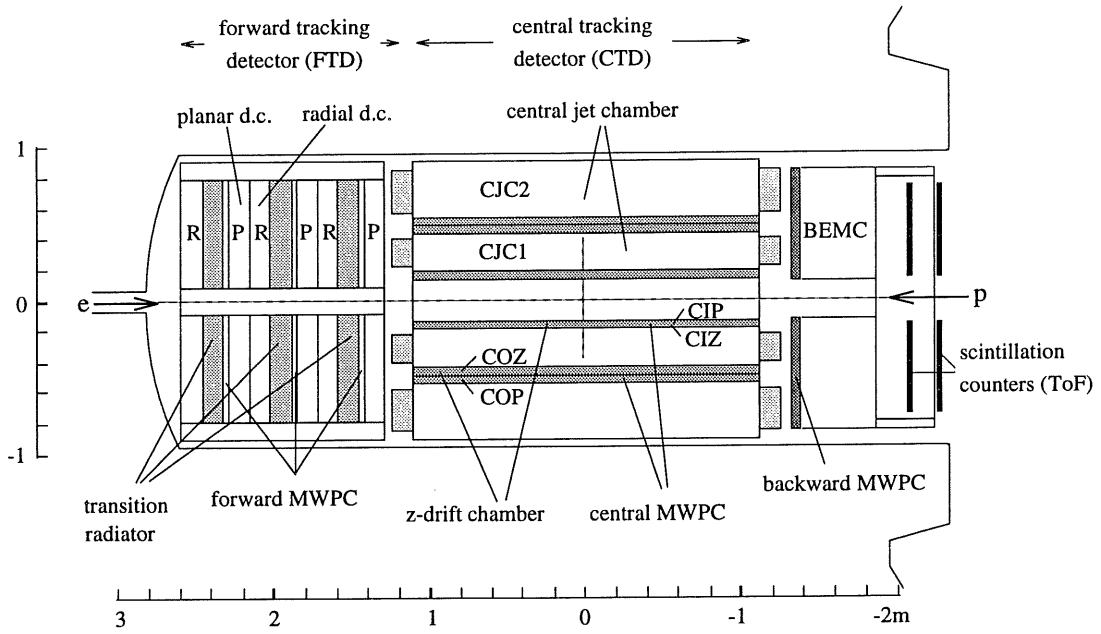


Figure 3.2: An $r - z$ projection of the H1 trackers.

### 3.3.1 The Forward Track Detector

The FTD consists of three repeated 'supermodules'. In order of increasing $z$, each supermodule contains a planar wire drift chamber (PWDC), a forward multi-wire

proportional chamber (FMWPC), a passive transition radiator and a radial wire drift chamber (RWDC).

In the PWDCs, the sense wires are strung perpendicular to the beam axis. Each PWDC contains three planes, each of four wires in $z$, rotated at $\frac{\pi}{3}^c$ to each other. The wires are separated by $6\,mm$ in $z$ and the drift cells are $56\,mm$ wide. Since the sense wires are only read out at one end, hits from each of the planes must be combined to give an accurate line segment. These segments can be linked together with segments found in the radial chambers and in the CTD to produce tracks.

The cathode pads of the FMWPCs are read out to give a fast trigger signal. The radial size of the pads varies between $18\,mm$ at the inner radius to $32\,mm$ at the outer. The inner 16 pads cover an azimuthal angle of $\frac{\pi}{8}^c$, the outer 4 cover $\frac{\pi}{16}^c$. There are two planes of cathode pads in $z$ that are read out, the pads being offset by one half of the pad size in $r$ to increase the effective polar angle resolution.

When a relativistic particle crosses a boundary between two media with different dielectric constants there is a (small) probability that the particle will emit a transition radiation (TR) photon. Since the probability is small, many interfaces are required to ensure efficient TR production. In H1, the transition radiator chosen is an array of polypropylene layers. The final yield of TR photons depends not only on the dielectric constant of the propylene, but also the layer thickness and separation. Since the TR photons are emitted at a small angle to the particle, they are observed in the RWDCs as a higher integrated charge. The front window of the RWDCs has to be carefully chosen to be gas tight and to be as X-ray transparent as possible.

In the RWDCS, the sense wires are strung radially. Each RWDC is divided azimuthally into 48 drift cells, resulting in a maximum drift length that varies from $10\,mm$ at the inner radius to $50\,mm$ at the outer. Each cell has 12 wires in $z$, separated by $10\,mm$. The sense wires are connected in pairs around the hub of the chamber, and both ends of the pair of wires are read out, allowing space point reconstruction from each hit. Track segments can then be reconstructed in the radial chambers and linked to the planar segments giving tracks through the whole of the forward tracker. Particle identification from both $dE/dx$ and TR detection is then possible.

### 3.3.2 The Central Track Detector

A section through the CTD is shown in figure 3.3

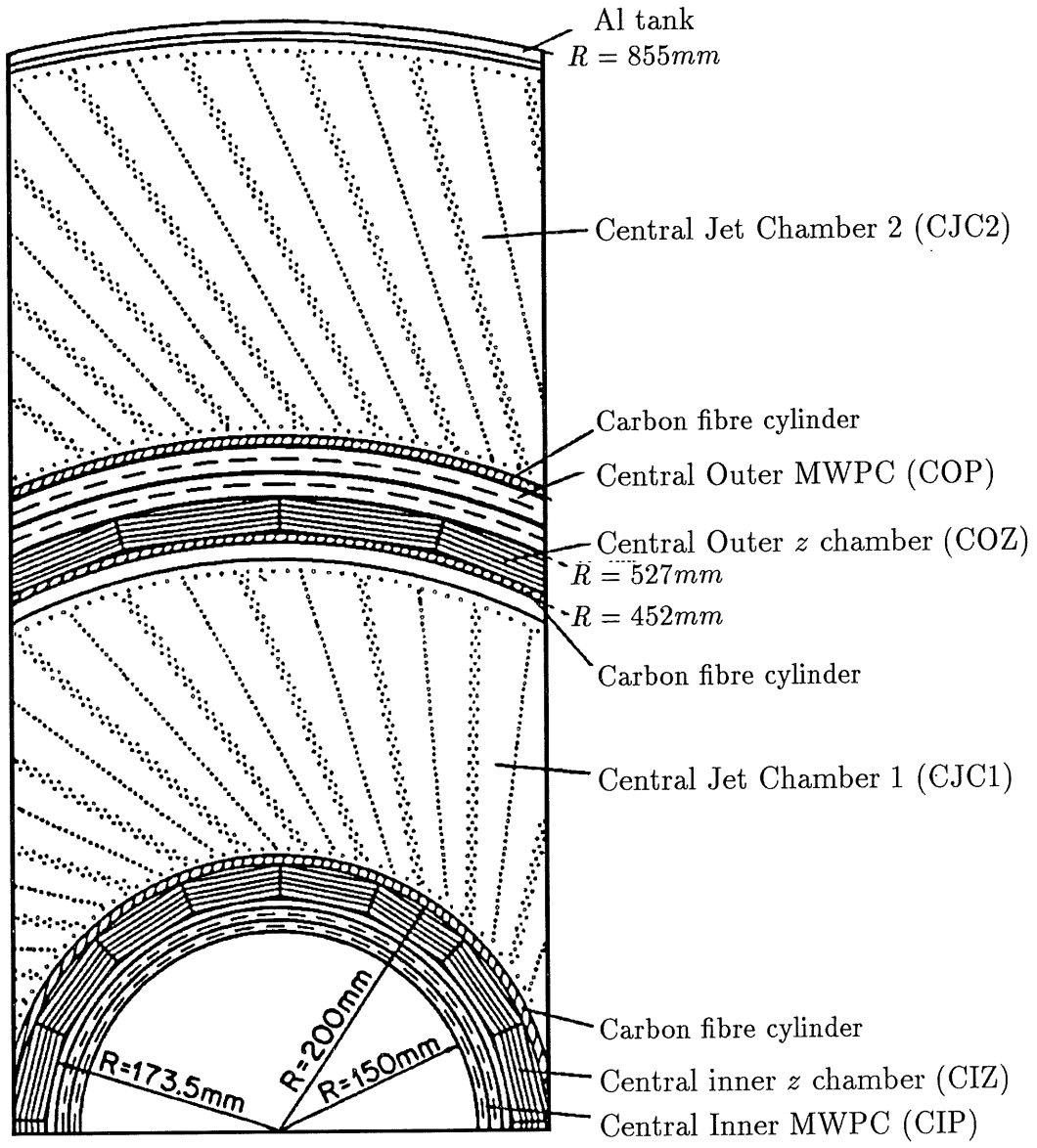


Figure 3.3: A section through the central track detector, perpendicular to the beam. The wires in the CJC are parallel to the beam axis and the drift cells are tilted at an angle of $\frac{\pi}{6}^c$ to the radial direction.

The main components of the CTD are the central jet chambers, CJC1 and CJC2. The sense wires are parallel to the beam axis and the drift cells are tilted at an angle of $\frac{\pi}{6}^c$ to the radial direction. The drift time gives an accurate point in the $r$–$\phi$ plane, and since both ends of the sense wires are read out, the $z$ coordinate of the hit can be found using charge division. CJC1 is divided into 30 cells in $\phi$ and has 24 sense wires per cell, CJC2 has 60 cells with 32 sense wires per cell. Owing to the tilt of the drift cells, a stiff track will cross at least one sense wire plane and may well cross a cathode plane as well. This aids resolving the drift sign ambiguity and allows the calculation of the time at which the event occurred.

In order to improve the $z$ resolution of the tracks found in the CTD, there are two $z$ chambers. The inner $z$ chamber (CIZ) is situated at the inner radius of CJC1, the outer (COZ) is between CJC1 and CJC2. The $z$ chamber drift cells form 'rings' around the beam axis, with the 4 sense wires per cell at different radii. The drift time gives the $z$ coordinate of the hit, charge division gives the $\phi$. The CIZ consists of 15 drift cells, with the 'rings' forming a 16 sided polygon around the beam line; the COZ has 24 drift cells and forms a 24 sided polygon.

The CTD contains two MWPCs for triggering on tracks that point to the interaction region. The inner of these two chambers, the CIP, is inside the CIZ, the outer is between CJC1 and the COZ. Each chamber consists of two concentric layer chambers, with the cathode pads being read out. In the CIP, the pads cover an angle of $\frac{\pi}{4}^c$ with the two layers rotated by one half pad to increase the effective angular resolution. Each $\phi$ sector is divided into 60 pads in $z$, making the pads $36.6\,mm$ long. The COP is divided into 18 pads in $z$ (a pad length of $120\,mm$) and each pad covers an angle of $\frac{\pi}{16}^c$.

### 3.3.3 The Backward Multi-wire Proportional Chamber

At large angles (greater than about $2.7^c$) charged tracks are not efficiently reconstructed in the central tracker. The backward multi-wire proportional chamber (BPC) is designed not only for triggering, but also to give accurate space point reconstruction. This is achieved by reading out the anode wires as opposed to the cathode pads, and by having four planes of wires orientated at $\frac{\pi}{4}^c$ to each other. The chamber is directly in front of the BEMC. The active region of the chamber extends from an inner radius of $135\,mm$ to $650\,mm$, giving an angular coverage of about $2.7^c$ (155°) to $3.04^c$ (174.5°). The BPC has an angular resolution of about $0.5 \cdot 10^{-3}\,^c$, of the same order as errors due to multiple scattering in front of the chamber [27]. The position of the chamber with respect to the rest of the H1 detector has been checked by using events in which track segments in the central tracker could be linked to a BPC hit. Using this method, the systematic angular

error on the space points was found to be less than $5 \cdot 10^{-3\,c}$ [28].

## 3.4 Calorimetry

Calorimeters consist of layers of material that cause a particle to shower, interleaved with sensitive regions to measure the development of the shower.

The interactions of high energy electrons and photons with a thick absorber are dominated by bremsstrahlung and pair production [29]. The particles created then undergo the same reactions, causing a shower of particles. The interactions of electromagnetic particles with matter is characterized by the radiation length, $X_0$, which is the mean distance in which a high energy electron loses all but $e^{-1}$ of its initial energy due to bremsstrahlung. As the energy of the particles in the shower decreases, the main loss of energy is through excitation and ionization. Provided that the shower is contained in the calorimeter, the amount of ionization is a measure of the energy of the incident particle.

When a strongly interacting particle interacts with matter, both elastic and inelastic scattering between the incident particle and nucleons occur. This results in secondary hadrons being produced and a shower forms. The characteristic length of such a shower is the interaction length, $\lambda_i$, which is usually much larger than $X_0$ (for lead $\lambda_I \approx 30X_0$ [30]. The cascade ends when the hadrons in the shower have energies that are sufficiently small for them to be stopped by ionization or nuclear capture. Hadronic showers typically penetrate much deeper into the calorimeter, and have a larger lateral size. In most calorimeters (called non-compensating calorimeters), about 20% of the energy of an incident hadron is lost through nuclear excitation or break up [29]. The difference in calorimeter response between electromagnetic and hadronic particles of the same energy has then to be corrected.

The resolution of an ideal calorimeter is limited only by the statistical fluctuations of the number of particles in the shower, giving $\sigma_E/E \sim E^{-\frac{1}{2}}$. In a real calorimeter, the resolution will also be affected by noise, non-containment of the showers, absolute calibration and internal calibration of different cells.

### 3.4.1 The Plug Calorimeter

The plug calorimeter is situated very close to the beam pipe in the forward direction. It consists of nine layers of copper absorber interleaved with eight layers of silicon detectors. When fully operational, the plug should have an energy

resolution of about $\sigma_E/E = 150\%/\sqrt{E}$, when $E$ is measured in $GeV$. This relatively poor resolution is due to coarse sampling, leakage and the large amount of 'dead' material in between the plug and the interaction region. During the 1992 running, only four of the silicon detectors were operational, and the plug was not used in this analysis.

### 3.4.2 The Liquid Argon Calorimeter

The liquid argon (LAr) calorimeter is divided into two sections, the electromagnetic calorimeter (EMC) and the hadronic calorimeter (HAC). These are housed inside a single cryostat, minimizing the amount of 'dead' material in front of the calorimeter. The EMC consists of $2.4\,mm$ thick plates of lead interleaved with $2.35\,mm$ gaps filled with liquid argon, with the signals being taken from a plane of pads within each gap. The HAC consists of stainless steel plates, $19\,mm$ thick. Double gaps of liquid argon, each $2.4\,mm$ thick, separate the plates. The signals are read out from planes of pads on either side of the board that separates the two liquid argon volumes. In total, the EMC is between $20\,X_0$ and $30\,X_0$, and the HAC is between $5\,\lambda_I$ and $7\,\lambda_I$. In order to allow for compensation of the difference between the electromagnetic and hadronic response of the calorimeter, it is highly segmented. The shapes of showers are then used to determine whether it was initiated by a hadronic or electromagnetic particle, and appropriate calibration factors are applied [31]. The fine granularity also allows for noise suppression by applying different noise cuts in a cluster of cells than to individual cells.

The resolution of the electromagnetic calorimeter is approximately $\sigma_E/E = 12\%/\sqrt{E} \oplus 1\%$ ($E$ measured in $GeV$) and of the hadronic calorimeter is $\sigma_E/E = 50\%/\sqrt{E} \oplus 2\%$ [31]. Much of the calibration of the detector was done using test beams at CERN. This was cross checked using electrons produced by cosmic muons and looking at the energy balance between the scattered electron and the measured hadronic energy in DIS events. The absolute scale of the electromagnetic calorimeter has been determined to 3%, and the hadronic calorimeter to 7% [28].

### 3.4.3 The Backward Electromagnetic Calorimeter

The BEMC is divided into 88 stacks, 64 of which are square with a side length of $159\,mm$. The around the outer edge of the BEMC the stacks are trapezoidal and triangular in shape, and around the beam pipe are the four 'triangle' stacks (see figure 3.4). The stacks are divided longitudinally into $2.5\,mm$ plates of lead interspersed with $4\,mm$ thick sheets of scintillator, giving a total of 50 sampling

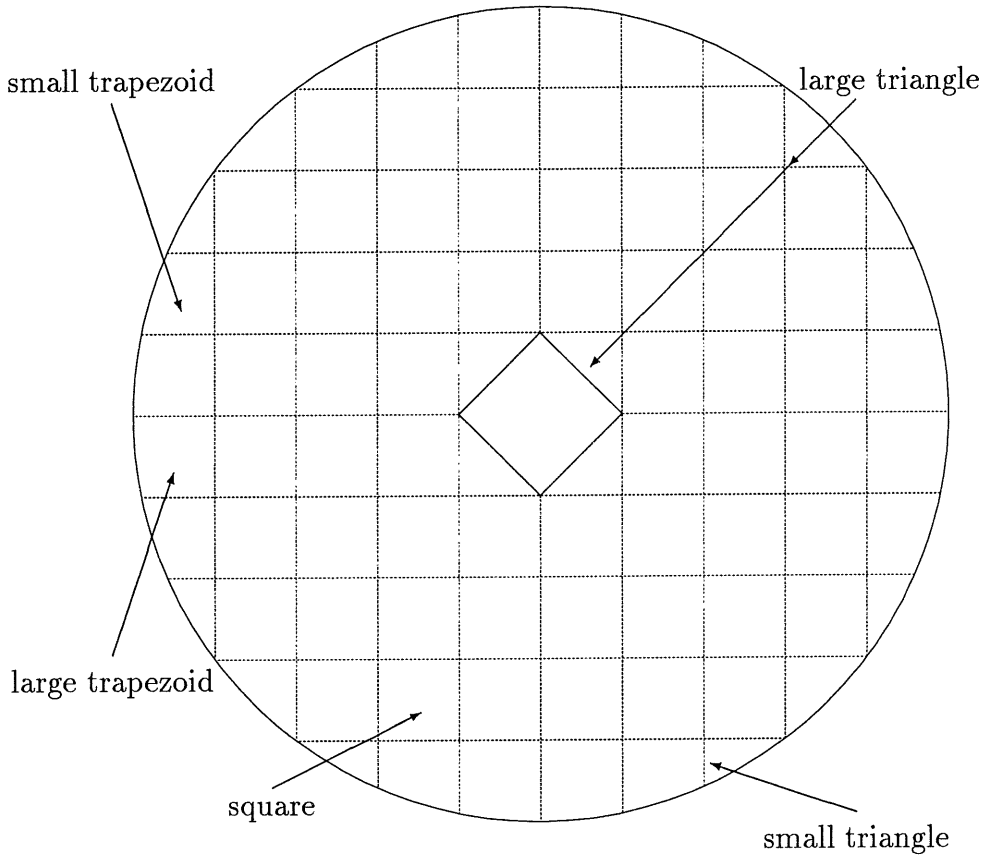


Figure 3.4: An $r$–$\phi$ view of the BEMC showing the different stacks. The large triangle stacks around the beam pipe are often just referred to as the 'triangle' stacks.

layers. The scintillators are read out from the side by wavelength shifters (WLS). For the 'square' and 'trapezoid' stacks, there are four $8\,mm$ wide WLS that run the entire length of the stack, two on one side of the stack, and two on the opposite side. Using the sharing of energy between the WLS, it is possible to find the position of the centre of gravity of a cluster in the BEMC with a precision of approximately $15\,mm$ [27]. On the other two sides of the 'square' and 'large trapezoid' stacks WLS of $160\,mm$ width are used to read out the last 15 sampling layers, allowing some calculation of the shower depth. The 'triangle' stacks the WLS run the entire length of the stack, but are on the two short sides of the triangle.

The BEMC has a total depth of $22.5\,X_0$ and $0.97\,\lambda_I$. This results in excellent containment of electromagnetic showers, but a very poor response to hadronic particles (approximately 30% of incident hadrons leave no significant signal in the BEMC, and only about 30% of the energy of interacting hadrons is contained [27]).

The resolution of the BEMC is $\sigma_E/E = 10\%/\sqrt{E} \oplus 0.42/E \oplus 0.03$ where $E$ is in $GeV$. The scale of the BEMC is found using the 'kinematic peak' (section 2.2). The peak can be clearly seen in figure 3.5 (a), which shows energy spectrum of electron candidates found in the BEMC. Also shown is the predicted energy spectrum for two different structure function parameterizations. As can be seen, the shape of the peak is dependent on the parameterization used, but the high energy edge of the peak is determined by the resolution of the BEMC. The second method that has been used is to use the hadrons to select events in the kinematic peak. This is done be demanding that the angle of the current jet, as calculated from the hadrons (section 2.2, equation 2.13), is less than $\frac{\pi}{3}^c$. The resulting energy spectrum is shown in figure 3.5 (b), and is compared with the predictions using two different structure function parameterizations. Whilst this method is less sensitive to the parameterization used, it is is more sensitive to the model used for the hadronization and the efficiency of the trackers (as a vertex is required to calculate the current jet angle). With these methods, the energy scale of the BEMC was determined to $\pm 2\%$. It was also found that the Monte-Carlo did not fully take into account the stack to stack inter-calibration uncertainties, and the energy as found from the Monte-Carlo had to be smeared by an additional $2.5\% \pm 2\%$.

The BEMC is also used for triggering events. The most important trigger from the BEMC is the BEMC single electron trigger (BSET). In this, the analogue signals from the four long WLS on each stack are summed and analyzed to provide the energy deposited in the stack and the bunch crossing of the collision giving the energy. The stack energies are then compared to two thresholds. The lower of these thresholds is just above the noise level (typically $1.3\,GeV$), the higher

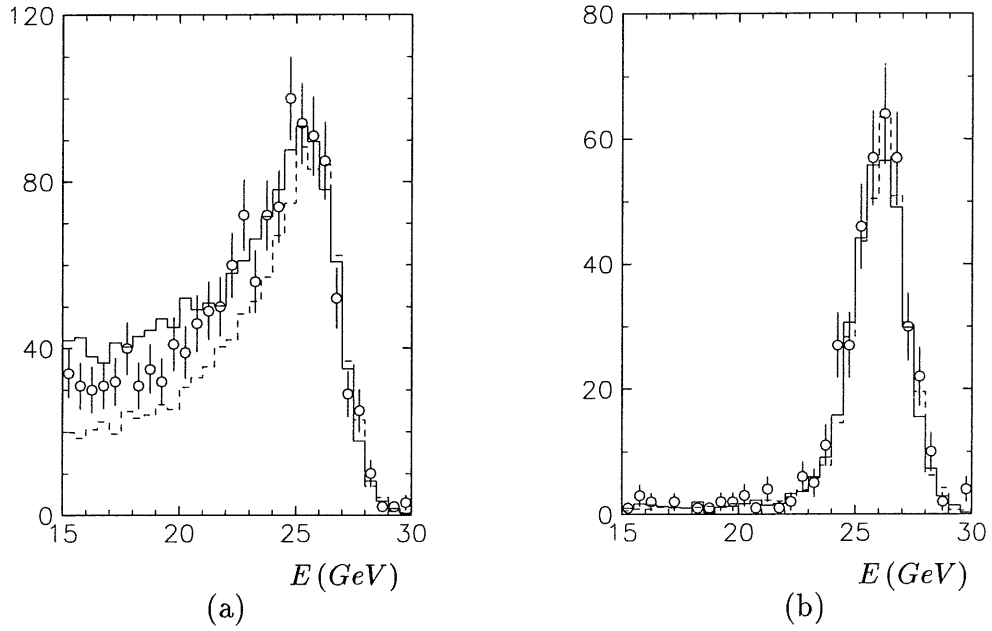


Figure 3.5: BEMC energy calibration plots. Figure (a) shows the BEMC cluster energy spectrum for all electron candidates for data (circles), the DJANGO Monte-Carlo with the $MRSD\_$ (solid line) and $MRSD_0$ (dashed line) structure function parameterizations. The shape of the kinematic peak is structure function dependent, but the high energy edge is determined mainly by the calibration. Figure (b) shows the BEMC cluster energy spectrum for events in which a vertex was reconstructed, and the angle of the current jet (as predicted by the hadrons) is less than $\frac{\pi}{3}^c$. This selects events in the kinematic peak, but is dependent on the hadronization models used in the Monte-Carlos, as well as the vertex finding efficiency.

is used as a cluster seed threshold (typically $2.3\,GeV$). If a stack has an energy greater than the high threshold then all the energies of all neighbouring stacks whose energy is above the low threshold are added to define a cluster. Trigger bits are then set on the basis of there being a cluster above a third threshold. In 1992, the BSET trigger was run with a cluster threshold of $2.5\,GeV$ [27].

### 3.4.4 The Tail Catcher

As well as providing muon detection, the pad readout of the muon chambers (section 3.5) acts as a tail catcher, providing an energy measurement of any

hadrons that are not fully contained inside the calorimeter. The system has a resolution of approximately $\sigma_E/E = 100\%/\sqrt{E}$, where $E$ is measured in $GeV$.

## 3.5 Muon Detection

As has been mentioned, the iron return yoke for the H1 magnet is instrumented with limited streamer tubes (LSTs). The iron is divided into three regions, the forward and backward endcaps where the iron is perpendicular to the beam line, and the barrel region where the iron is parallel to the beam line.

The streamer tubes consist of plastic tubes with a square cross section, $10\,mm \times 10\,mm$, with a single wire held at ground potential running down the middle. Three of the sides of the tube are painted with low resistivity graphite paint, to which the high voltage is applied. The fourth side is coated with a much higher resistivity paint. Depending on the position of the LST in the detector, either strips or pads are glued to this side. The wires, strips and pads are all read out. The resolution of hits on the wires is of the order of $4\,mm$. The strips are perpendicular to the wires and have a resolution of about $10\,mm$. The pad sizes are of the order of $400\,mm \times 500\,mm$ in the barrel region, and $280\,mm \times 280\,mm$ in the endcaps.

Muon detection in the forward region is enhanced by the forward muon detector (FMD). This is designed to detect muons in the angular range $0.05^c$ (3°) to $0.3^c$ (17°) with a momentum greater than $5\,GeV$. The system consists of a toroidal magnet sandwiched between two sets of drift chambers, and provides a momentum measurement for muons up to approximately $200\,GeV$.

## 3.6 The Time of Flight counters

The time of flight counters (ToF) is situated behind the BEMC, at $z \approx -2\,m$ (see figure 3.2). It consists of two planes of scintillators which cover an area equivalent to that of the BEMC and provide timing with an accuracy of about $4\,ns$. The plane nearest to the interaction point is divided into 16 counters, the other into 8. To prevent damage by synchrotron radiation each plane is sandwiched by lead plates and the inner counters can be moved away from the beam line using a system of pneumatic rams.

Comparison of the time of particles passing through the ToF with the time at which the beams cross gives powerful rejection of proton induced background. If

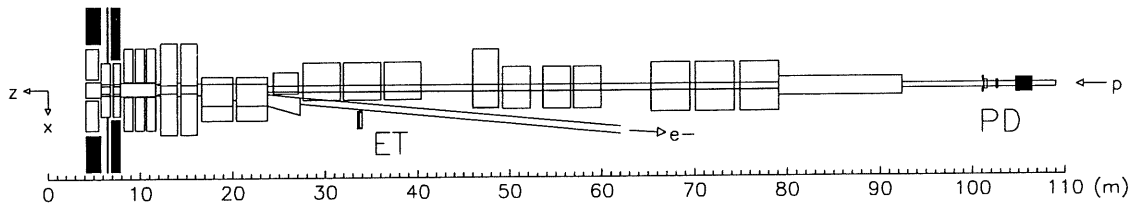


Figure 3.6: The H1 luminosity system.

a proton interacts with either residual beam gas or the beam wall before entering the H1 detector, the particles from such an interaction will pass through the ToF at approximately the same time as the proton bunch passes the ToF. For collisions that occur inside the detector, the collision fragments will reach the ToF later by a time of $2\Delta z/c$, where $\Delta z$ is the distance of the collision from the ToF. For collisions occurring in the interaction region, this time difference is of the approximately $13\,ns$, but varies owing to the proton bunch length (2–$3\,ns$).

For the identification of background and $ep$ collision events, three time 'windows' are defined. The 'global' time window is $96\,ns$ wide and contains all the hits from a single bunch crossing. The 'background' time window is within the global window and is about $25\,ns$ wide. The interaction time window immediately follows the background window and has a width of $13\,ns$.

The ToF background signals were used as a veto on some events triggered by other parts of the detector (a fraction of the triggers were not vetoed to allow the efficiency of the ToF to be monitored). This vetoing reduced the trigger rate by 99% [27] in 1992, without which the detector would have been swamped by constantly processing background events.

## 3.7 The Electron Tagger and Photon Detector

The H1 luminosity system (figure 3.6) consists of two Čerenkov calorimeters, the photon detector (PD) at $z \approx -100\,m$ and the electron tagger (ET) at $z \approx -33\,m$, situated very close to the beam line. The luminosity is calculated from the rate of bremsstrahlung of the electron, $ep \rightarrow ep\gamma$, by demanding a coincidence between the two detectors. At low $Q^2$, where the structure of the proton is not

resolved, the cross section for this reaction is very well known so that measuring the rate for such collisions and knowing the acceptance of the detectors provides a measurement of the luminosity. Backgrounds to the measurement come from bremsstrahlung interactions of the electron and residual beam gas, synchrotron radiation and proton beam halo.

Both detectors are made of arrays of crystals that have a square cross section and are $200\,mm$ ($\approx 22X_0$) deep. The PD covers an area $100\,mm \times 100\,mm$ with 25 crystals; the ET covers an area of $154\,mm \times 154\,mm$ with 49 crystals. They have a position resolution of better than $1\,mm$ and an energy resolution of $10\%/\sqrt{E} \oplus 1\%$ [27]. A $2\,m$ iron wall behind the PD protects it from proton beam halo. Synchrotron radiation is removed by a $2X_0$ lead plate in front of the PD. A water Čerenkov counter between the lead and PD is used to reject events in which the bremsstrahlung photon interacts with the lead. The background due to residual beam gas is calculated from the rate of of events recorded from the electron 'pilot' bunch. The greatest uncertainty to the luminosity measurement is due to the uncertainty on the acceptance (about 5.5% as of December 1993), and it is anticipated that the systematic error on the luminosity can be reduced from the current value of 7% to approximately 5% [27].

As well as providing data for luminosity measurement, the system can be used to tag photoproduction events with $Q^2 < 0.01\,GeV^2$ by demanding a detected electron and using the photon detector as a veto. This greatly reduces the proton induced background in the photoproduction sample. The photon detector can also be used to look for DIS events with hard initial state radiation.

## 3.8 The Trigger

At HERA, the time between bunches colliding is just $96\,ns$. Since it takes $1\,ms$ to read out all the subdetectors, the trigger has to be able to select interesting physics events before the read out process starts. The trigger central trigger receives elements from many of the subdetectors. Trigger elements include

- the ToF (see section 3.6).
- coincidences between hit planes in the BPC.
- coincidences between hits in the CIP
- the $z$-vertex trigger. 'Rays' are formed by finding coincidences between hits in the CIP, COP and first FMWPC. The projection of these rays onto the beam axis is used to fill a histogram. For an event from the interaction

region, this is expected to have a peak, whereas if the event came from outside the interaction region it is expected to be flat,

- the forward ray trigger. Hits in the FMWPCs and CIP are linked to form rays that point towards the interaction region.

- the electron tagger and photon detector.

- the calorimeter trigger. Calorimeter cells of the LAr, BEMC and plug are grouped into a set of 'big towers' that point back to the interaction region. The energy in the hadronic and electromagnetic sections of the big towers are summed separately. Triggering is then done on the basis of the total energy, the transverse energy, the 'missing' transverse energy. An electron trigger is also available by finding big towers with a large energy deposit in the electromagnetic part of the tower, and a small deposit in the hadronic.

- the BEMC single electron trigger (section 3.4.3)

- the instrumented iron trigger. Coincidences between hits in the muon chambers are used to select events with muon candidates.

- the forward muon trigger. The forward muon drift chambers also provide muon trigger signals.

It takes many bunch crossings (BC) before all the signals can be collected and the first 'level' of the trigger decision is only available after 24 BC. In order that data are not lost, data from successive bunch crossings are stored in a 'pipe-line'. The pipe-lines for the subdetectors vary in length, but hold information for the previous 27 to 35 bunch crossings. Thus once the first level trigger has decided that an *ep* collision may have occurred (an L1 keep), the pipe-lines have to be stopped from taking any more data.

Following an L1 keep, the detector is 'dead'. In order to minimize the 'dead-time', two more levels of triggering of increasing complexity are available before the detector is read out. These two levels were not commissioned for the 1992 running, but were not required as the HERA machine was not running with the design beam currents, and the level 1 trigger was able to reduce the rate of events to a rate that could be accepted by the data acquisition system (DAQ).

The DAQ collects all the data from the experiment and sends it to the fourth level trigger (L4). Once the data has been sent, the pipe-lines are restarted and the experiment can take data. L4 consists of a 'farm' of fast processors that run in parallel. In 1992, there were fourteen processors, each of which could process one event at a time. In order to minimize the time required for processing an event, the L4 code consists of various logical modules which are run only if their

output is required for a decision to be made. A small fraction of events (1%) that were rejected by the farm were kept for efficiency calculations.

## 3.9 The Data Acquisition System

The data acquisition system (DAQ) is based around the VMEbus system [32]. A brief description of the DAQ is given here, full details can be found in [33]. Once the level two trigger has decided that an event should be kept, subdetector read out is initiated. Each of the twelve subdetectors compresses the data and sends it via an optical fibre ring to the central data acquisition system (CDAQ). This 'builds' an event from the subdetector data and passes it to the level 4 farm, and to permanent store on the IBM if the event is accepted. It also allows data to be taken for monitoring purposes, such as the online event display and histograms. At the subdetector level, there are some twenty seven thousand channels and approximately $3\,M$bytes of raw data. After compression the data is transfered around the fibre ring at a rate of typically $1.5 Mb/s$ [27]. The data is finally written to the IBM at a rate of about $0.6 Mb/s$ (5-10 events/s).

## 3.10 Summary

The H1 detector has been designed to cope with the challenging environment of the HERA collider. The detector has to cope with bunches of electrons and protons colliding every $96\,ns$, and very high rates of background events with respect to interesting physics. This has been successfully achieved, as shown by the results on both DIS and photoproduction that have been produced.

# Chapter 4

# Event Selection

The data used in this analysis were taken in the autumn of 1992 and correspond to a useful integrated luminosity of approximately $22.6\,nb^{-1}$. Only runs during which the CJC, BPC, LAr calorimeter, ToF, BEMC and trigger were fully operational are considered. The data from the first period of H1 running (June-July 1992) which corresponded to an integrated luminosity of $\approx 1.3\,nb^{-1}$ are not included as differences in efficiencies of the detector components in the two periods would increase the systematic errors at the expense of only a small gain in statistics.

## 4.1 Principles of Event Selection in H1

After satisfying all the trigger requirements, data from the H1 experiment are sent to the IBM for storage on permanent cartridge. Once the calibration constants of the detectors have been checked and, if necessary, corrected, the data are passed to the level 5 'trigger'. This consists of two powerful Silicon Graphics computers which reconstruct events using the H1REC [34] program and also classify events using parts of the H1PHAN [35] package. The results of the classification are written into the event record key [36], allowing users fast selection of events. Two stages of classification are done, the first loose classification is for the POT (Physics On Tape) cartridges, the second tighter cuts for the DSTs (Data Summary Tapes). The POT cuts are loose such that if and when improved versions of the reconstruction package are released, it is necessary only to reconstruct the POT tapes, a much quicker job than a complete reconstruction of all the raw data. For the autumn 1992 running, this amounts to approximately 2500 IBM cartridges which is too large a data sample for analysis, requiring a second stage of selection. After the DST selection, the data for most classes are able to

reside on disk allowing easy access. The DST selection then provides a common basis for the analysis of a given class of physics events.

## 4.2 Selection of Neutral Current DIS Events

For this thesis, neutral current DIS events are distinguished from other classes of events in HERA by the detection of the scattered electron. Electron candidates are initially chosen by finding electromagnetic ($EM$) clusters in the calorimeters. Kinematic constraints then lead to several possibilities for finding the scattered electron based on the four vectors of the measured particles. In a DIS collision the transverse energy of the electron is balanced by that of the struck parton. However in the hadronization of the parton that follows the energy is shared between many particles and so it is expected that in many cases the electron will have a higher transverse energy than any other single particle in the event. For low $y$ events, the current jet goes forward in the detector and the electron backwards. Thus another possible discriminator is to select the particle with the largest negative component of longitudinal momentum [37]. In practice this method works at all but very high values of $y$, because even when the current jet is also in the backward region individual particles usually have relatively small energies. Thus for the selection of low $Q^2$ events, a high energy $EM$ cluster is expected in the backward region of the detector.

Similar arguments lead to the expectation that searching for high energies in the backward region will also lead to the rejection of background events. In photoproduction events the electron escapes along the beam pipe. From energy–momentum considerations, the total longitudinal momentum of the rest of the system is higher than for the e–p collision. This results in only a small fraction of events having large energy deposits in the backward region of the detector and the energy spectrum of particles incident on the BEMC falls rapidly becoming negligible above about $16\,GeV$. However it must be remembered that the rate of photoproduction events is much higher than the rate for DIS due to the $\frac{1}{Q^4}$ term in the differential cross section (see equation 2.17 in section 2.3) and so accepting only a small fraction of the total number of photoproduction events could still lead to a high level of background.

In the case of beam proton interactions with residual gas or the beam pipe in the interaction region, the collision rest frame will be boosted along the proton direction and so a steeply falling energy spectrum of particles incident on the BEMC is expected. If the collision occurs upstream (ie. large negative–z) of the detector and the event is not vetoed by the ToF then larger energy deposits may be detected. Electron–beam gas collisions are the scattering of the electron off

a stationary proton, so the rate will be dominated by photoproduction off the proton. Since the centre of mass energy of these collisions is smaller than for the beam-beam interactions the energy spectrum of particles incident on the BEMC will also be expected to be relatively small.

It can thus be seen that the demand of a high energy cluster in the BEMC will not only select DIS events but will also reject many background events. The purity of the event sample is monitored using events from the pilot bunches (section 3.1) to estimate the background due to interactions of beam particles with the beam wall and residual beam gas, and events with a signal in the electron tagger for photoproduction background.

Two classes of events are considered for this analysis, classes 10 ('NCHAD' - DIS candidates for hadron studies) and 11 ('NCLQSQ' - low $Q^2$ DIS candidates) [38]. There is a large overlap between the two samples. Class 10 is used mainly for studies of hadronic energy flow and so demands other activity in the detector besides the electron. Class 11 is designed more for low $Q^2$ structure function studies. The initial selection is of events with at least one energetic cluster in the backward region of the detector. The most energetic (leading) cluster is then the electron candidate. The electron finding as described is very simple giving a high efficiency for selecting DIS events but with a low purity, the main sources of background for low $Q^2$ events being due to beam interactions.

After the first level of event selection the background is then reduced by associating tracking information with the leading cluster to ensure that the $EM$ cluster is from a single charged particle. Tight cuts are placed on the position of the electron to ensure that the cluster is fully contained in the detector. To ensure that the kinematics of the event are correctly reconstructed and to eliminate backgrounds from events originating outside the interaction region the final sample of events contains only those events for which a vertex could be reconstructed from the tracking chambers. Photoproduction events are removed and $EM$ radiative corrections are reduced by cutting on the energy undetected in the backward direction.

## 4.3 Selection of Monte-Carlo events

Two sets of Monte-Carlo DIS events were generated using DJANGO (section 2). Approximately $72 \cdot 10^3$ events were generated in the range $x_{bj} > 4 \cdot 10^{-5}$ and $Q^2 > 3\,GeV^2$ with the $MRSD\_$ (see section 2.4.1) parameterization as the assumed structure function, corresponding to a cross section in this kinematic region is

$515 \pm 3\,nb$. The sample is therefore equivalent to an integrated luminosity[1] of approximately $140\,nb^{-1}$. Another $50 \cdot 10^3$ events were generated in the same way using the $MRSD_0$ parameterization. This event sample corresponds to a cross section of $358 \pm 1\,nb$ ($\mathcal{L}_{MC} \approx 140\,nb^{-1}$).

Only those events in which the electron was scattered at angles of less than 175° (reducing the samples to $30 \sim 40 \cdot 10^3$ events) were then passed through the simulation program, H1SIM [39], before being reconstructed and classified using the same programs as for the data. Figure 4.1 show the electron energy spectrum and scattering angle as simulated using the different parameterizations.

Two Monte-Carlos were used for the generation of the photoproduction background. Approximately $180 \cdot 10^3$ 'soft' (section 2.6) $\gamma P$ events, corresponding to a cross section of $6.3\,\mu b$ were generated using RAYVDM ($\mathcal{L}_{MC} \approx 30\,nb^{-1}$). $120 \cdot 10^3$ hard $\gamma P$ events were generated using PYTHIA with $\hat{p}_T^{min} > 2.5\,GeV/c$, a cross section of $2.4\,\mu b$ ($\mathcal{L}_{MC} \approx 48\,nb^{-1}$).

Only a small fraction of all the photoproduction events provide a background to the DIS signal. In order to save processing time and to allow easy access to this sample of events the simulation was done in two stages. Initially only particles at angles of greater than 150° were simulated. The simulation was completed only if there was a BEMC cluster of greater than $5\,GeV$ and a BPC hit within $20\,cm$ of the cluster. This reduced the event samples to approximately 3000 and 2000 events for the 'hard' and 'soft' samples respectively. Figure 4.2 show the energy and angular distributions of the electron candidates after reconstruction of the selected background events.

## 4.4 Online Selection

The main first level trigger used for this analysis is the BCL2 trigger (section 3.4.3). The raw rate for this trigger is dominated by interactions of protons with residual beam gas and the beam wall downstream of the H1 detector. Most of these events are vetoed by the ToF (section 3.6). The ToF veto was not applied to all trigger bits so that losses could be monitored. For the period of running in consideration, the BCL2 trigger thresholds were set such that the efficiency was $\approx 80\%$ at $4\,GeV$, rising to over 99% for energies greater than $10\,GeV$ [27]. The level two and three triggers had not been commissioned for the 1992 data taking period. The final stage of online triggering is the filter farm (section 3.8).

From possible DIS candidate events this rejects events from outside the fiducial

[1] A Monte-Carlo 'luminosity' can be defined in an analogous way to that for the experiment, $\mathcal{L}_{MC} = \frac{Number\ of\ events\ generated}{Cross\ section\ of\ process}$

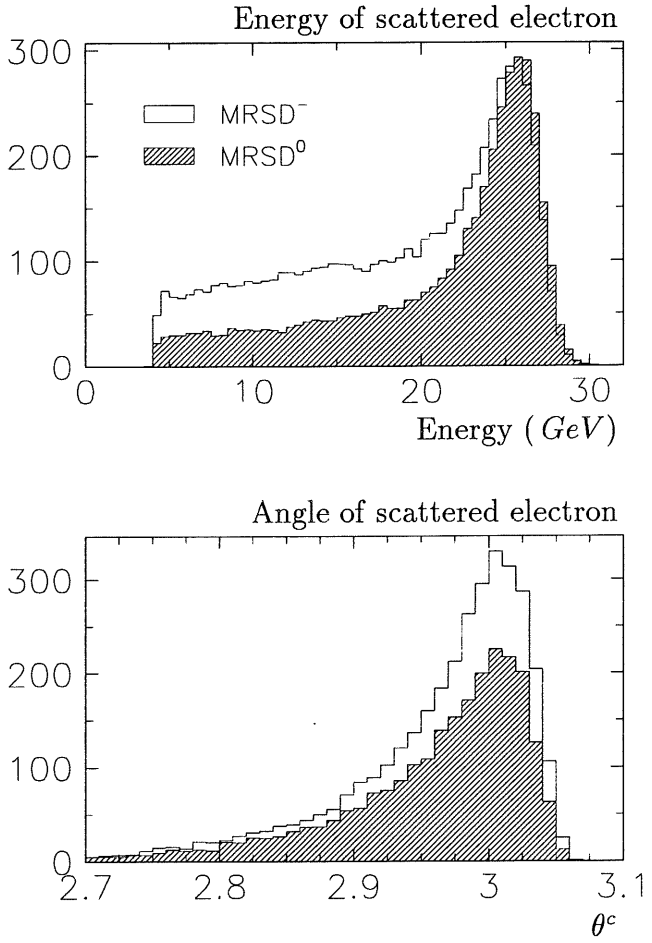


Figure 4.1: Energy and angular distributions of the scattered electron for DIS events after simulation and reconstruction, normalized to $22.6\,nb^{-1}$. The hatched histogram shows the distributions using the $MRSD_0$ parameterization, the solid line is for $MRSD\_$.

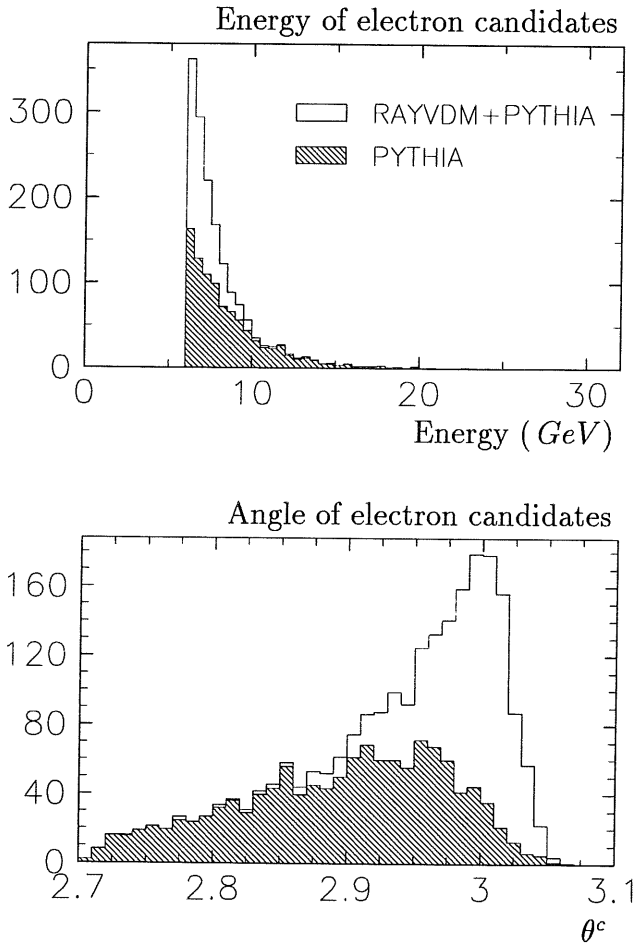


Figure 4.2: Energy and angular distributions of electron candidates for $\gamma P$ events after simulation and reconstruction, normalized to $22.6\,nb^{-1}$. The hatched histogram shows the distributions from PYTHIA, the solid line shows the sum of the PYTHIA and RAYVDM events.

volume of the detector and events with a large fraction ($> 90\%$) of the leading cluster's energy in one photodiode of the BEMC. For a particle showering in the BEMC, having such a large fraction of light collected in one wavelength shifter is highly unphysical. Studies have shown that these events are caused by synchrotron radiation photons directly hitting a wavelength shifter.

## 4.5 POT Selection

Class 10 events are required to have an *EM* cluster and a 'good' track, whilst class 11 events require only an *EM* cluster in the backward region of the detector ($\theta > 150°$). An *EM* cluster is defined as either

1. a BEMC cluster with energy greater than $4\,GeV$

or

2. a LAr cluster with a transverse energy greater than $8\,GeV$ and

   (a) less than one half of its energy in the hadronic part of the calorimeter

   or

   (b) its impact is such that it lies within 5° of a $\phi$ crack

and a 'good' track is either a track found in the central tracking chambers with

1. transverse momentum greater than $0.2\,GeV$,
2. more than 16 hits in the CJC,
3. a distance of closest approach to the beam axis ($DCA$) of less than $2\,cm$,
4. a distance from the nominal interaction point to the point of $DCA$ of less than $50\,cm$,
5. a start radius (the distance from the beam axis to the first point on the track) of less than $30\,cm$,

or a forward track with

1. a $DCA$ that is less than ten times the error on the $DCA$.

The tracking cuts were designed so as not to select events on the basis of tracks that came from outside the interaction region, such as from beam wall

collisions, or tracks that were poorly reconstructed. The tighter cuts on the class 10 events results in a cleaner sample of events but also rejects some true DIS events, especially in the kinematic peak (low $y$) region, where there is very little hadronic activity.

## 4.6 DST selection

For both classes 10 and 11 tighter cuts are made on the ToF signals to further reduce the background from upstream collisions. For an event to be rejected there had to be either

1. one or more hits in the background time window and no hit in the interaction time window,

or

2. more than two hits in the background time window.

The losses of true DIS events due to the ToF veto and the off-line cuts have been studied in great detail [40]. It is found that $4 \pm 3\%$ true DIS events are rejected and this is included in the normalization corrections to the measurement.

No further cuts were made to the class 10 selection. For class 11 further background rejection was made on the basis of linking BPC hits to clusters. Since the measurement of hadronic energy in the BEMC is poor, with a relatively large fraction of energy leaking out of the detector, many of the high energy clusters in the BEMC come from photons (either directly or from $\pi^0$ decay). Since photons are not detected in the BPC, demanding a BPC hit in the vicinity of the cluster reduces the backgrounds. A loose cut is made such that there is a BPC point within $15\,cm$ of the centre of gravity[2] of the BEMC cluster for clusters with energies less than $22\,GeV$. No cut is made on higher energy clusters so as to keep as many events in the 'kinematic peak' (section 2.2) as possible and to allow monitoring of the BPC efficiency, since the background in this region is negligible.

The 'hardware' efficiency of the BPC can be calculated using the ratio of the number of times the fourth wire plane is present given that a hit has been found using only three of the wire planes. This efficiency is then used in the Monte-Carlos for event simulation. The efficiency for accepting an event also depends

[2]For this selection the centre of gravity of the cluster is calculated by weighting the portion of the centre of a stack with its energy. Later tighter cuts are made using the wavelength shifter information (section 3.4.3). Owing to the loose nature of the cut no events that would be accepted by the tight cuts are lost.

on the average number of hits that an electron makes when it goes through the chamber. The electron can make more than one hit due to its synchrotron radiation converting in the material in the end wall of the CJC. The resulting efficiency of the DST selection has been well tuned in the Monte-Carlo to reproduce the data.

## 4.7 Final Selection

Classes 10 and 11 give a high efficiency for the selecting DIS events. The efficiency of class 11 is only affected by the hardware efficiency of the detector. Class 10 has an efficiency that depends on the models used for the hadronization of events. However the sample of events still contains a high proportion of background events, mainly from photoproduction. Further cuts are therefore required before a clean sample of well measured DIS events is isolated. Cuts are placed on:

1. The cluster position (the 'triangle' cut).
2. Identification of the electron.
3. the event kinematics,
4. reconstruction of an vertex within the interaction region,
5. the quality of the event.

### 4.7.1 The triangle cut

The first cut is to reject events with an electron in the 'triangle' stacks of the BEMC (section 3.4.3). These stacks do not initiate a cluster for the BSET trigger and hence the efficiency of the trigger for such events is difficult to calculate. There is also a high probability that the electron energy has not been fully contained within the calorimeter, resulting in poor reconstruction of the electron energy. Events are rejected if the leading stack in the cluster is one of the triangle stacks, or if the centre of gravity of the cluster[3] is within 16 $cm$ of the beam axis.

[3]This is now calculated using the wavelength shifters.

### 4.7.2 Electron identification

Electromagnetic particles deposit most of their energy in the forward part of the BEMC and have a small lateral spread, whereas hadronic particles are generally broader and penetrate to the rear of the calorimeter. These properties are used to purify the data sample by demanding that the leading cluster has

1. an energy weighted radius of less than $4\,cm$
2. a hadronic fraction of less than 0.2

Owing to the coarse granularity of the BEMC and the relatively high noise levels in the back wavelength shifters, these cuts are necessarily very loose so as not to reject true electron candidates unnecessarily.

A more powerful cut is made on associating the electron cluster with tracking information. The centre of gravity of the leading BEMC cluster, all BPC points and central tracks are projected from the vertex onto a common plane. Events are rejected if the minimum distance between the cluster position and the nearest tracking point is greater than $4\,cm$. The data are compared with DIS and background Monte-Carlos[4] in figure 4.3 For these plots only candidate electrons with energies greater than $16\,GeV$ were used in the comparison of data and DIS and with energies less than $10\,GeV$ when comparing data and photoproduction background.

### 4.7.3 Event kinematics

In an ideal detector, all the particles from the collision would be detected, and so energy and momentum conservation could be used to ensure that an event was indeed from a beam-beam collision. However since the proton remnant jet is not fully contained in the detector, not all the constraints can be used. Just as in the case of calculating $y$ from the hadrons using the Jacquet-Blondel method (section 2.2), where the sum of energy minus the longitudinal momentum of all hadrons in the event can be used, the total sum of all particles in the event including the electron ($\Sigma$) can be used as a check of the event. For a non-radiative DIS event, $\Sigma$ should be approximately twice the incoming electron energy, whilst for photoproduction events it will be smaller by twice the electron energy. In the case of interactions of protons with either the beam wall or beam gas particles $\Sigma$

[4]Unless otherwise stated Monte-Carlo DIS events are from DJANGO10 with the *MRSD_* structure function parameterization and background events are the sum of events from the RAYVDM and PYTHIA Monte-Carlos with the correct relative normalization.

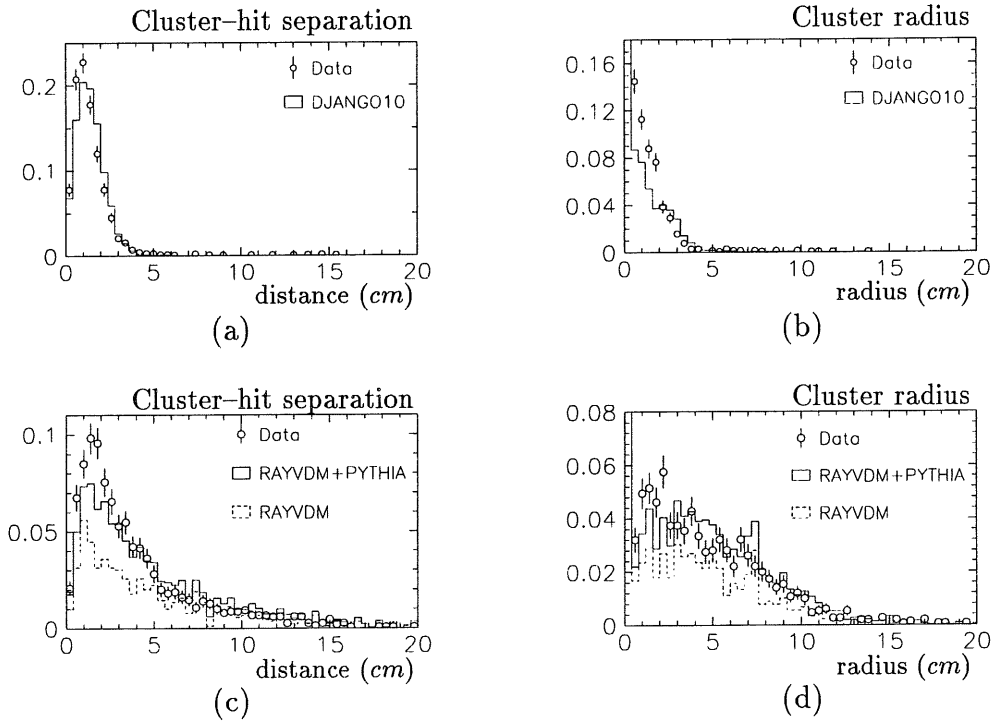


Figure 4.3: Comparison of data and Monte-Carlo distributions of BEMC cluster radius and cluster–BPC hit separation. For figures (a) and (b) a the candidate electron energy is greater than $16\,GeV$, for (c) and (d) it is less than $10\,GeV$. This is done to get reasonably pure samples of true DIS and photoproduction data.

should be small. The spectrum of $\Sigma$ for data is compared with Monte-Carlo in figure 4.4

### 4.7.4 Event vertex

To allow the event kinematics to be accurately reconstructed and to reduce the backgrounds due to non beam-beam interactions a cut is placed on the event vertex. The distribution of the vertex along the beam axis is shown in figure 4.5. The spread of the vertex allows the detection of electrons scattered at larger angles for collisions occurring further from the BEMC. Since the cross section is a strong function of angle, the mean of the distribution is seen to be shifted from the nominal interaction point. An unbiased vertex distribution can be obtained by demanding that the angle of the electron lies between 164° and 168° and that

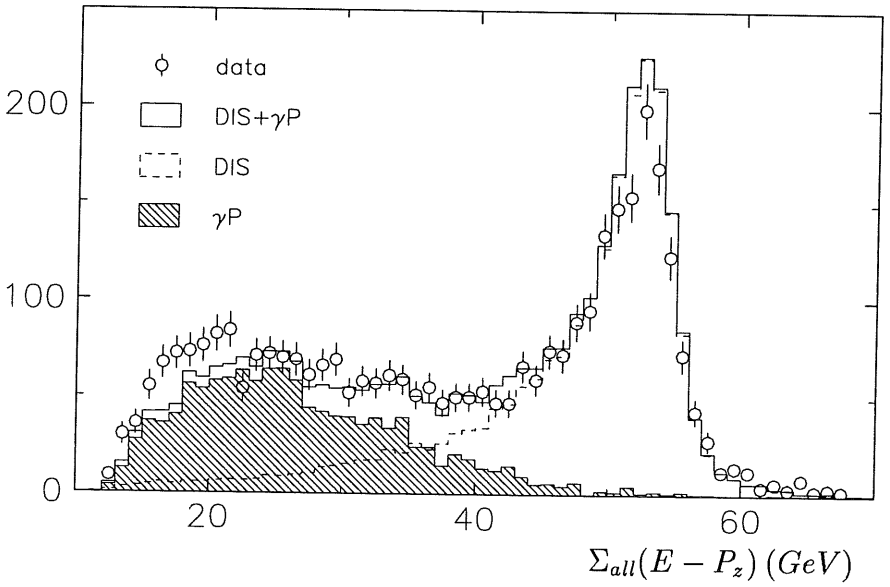


Figure 4.4: A comparison of $\Sigma_{all}(E-P_z)$ for data (points) and Monte-Carlo after demanding at least one BPC hit within 15 $cm$ of the leading BEMC cluster. The dash line is a DIS Monte-Carlo, the hatched histogram is for photoproduction and the solid line is the sum of the two.

the vertex lies within $\pm 50\,cm$ of the nominal interaction point. This was done and the distribution was found to be in agreement with that obtained from photoproduction events (where there is no bias). For the purposes of event simulation the vertex distribution was then parameterized as a Gaussian of width 25.5 $cm$ over a range of $\pm 70\,cm$.

Close study of the time distribution of hits in the ToF revealed an unexpected peak at $8\,ns$ from the nominal interaction time. This was identified as being due to collisions with the satellite bunches (section 3.1). These events can be seen in the vertex distribution as a small peak at about $120\,cm$ from the nominal interaction point. Such an event is shown in figure 4.6.

The efficiency of cutting on the position of a reconstructed vertex was broken down into two parts, a global factor due to events from outside the interaction region and local corrections due to the efficiency of reconstructing an event vertex. Using the ToF plots as well as the vertex distribution it was estimated that $10\pm 2\%$ of events were lost due to demanding that an event occur within $\pm 50\,cm$ of the nominal interaction point [41].

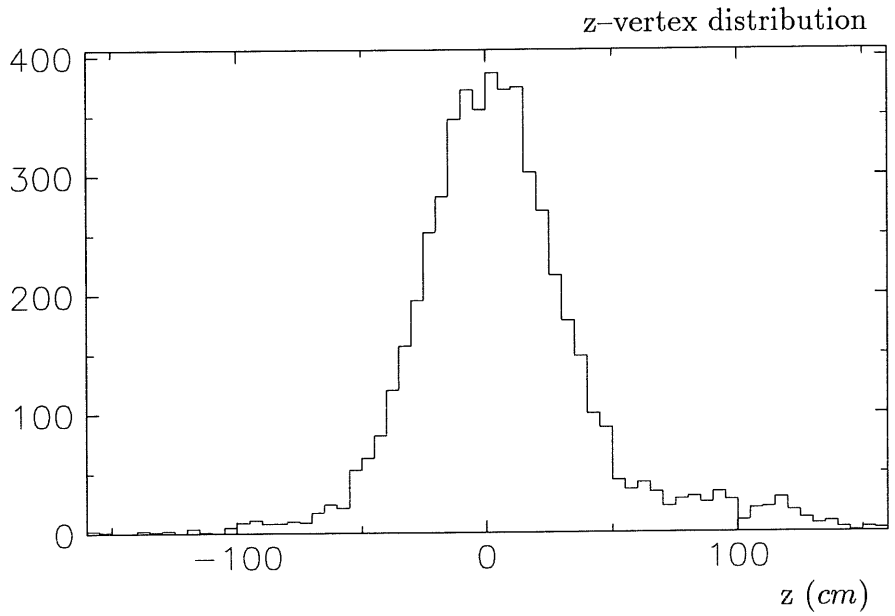


Figure 4.5: The z-vertex distribution for all DIS candidate events with a reconstructed. The main peak is asymmetric due to the $\frac{1}{Q^4}$ term in the cross section. A secondary peak due to the satellite bunches can be seen $z \approx 120\,cm$

The satellite bunches complicate the calculation of the efficiency for reconstructing a vertex because it is not known whether an event that does not have a reconstructed vertex occurred within the interaction region or not. Thus in order to calculate the efficiency, an independent method of vertex reconstruction is required. In this analysis the electron is used to form a vertex using a coincidence between the two planes in the CIP (section 3.3.2) and the BPC hit attached to the electron candidate. Two regions of $\phi$ had to be cut from the efficiency calculations due to hardware problems with the CIP. These are $-0.79^c < \phi < 0^c$ and $1.9^c < \phi < 2.8^c$, and can be clearly seen in figure 4.7 (a) which shows the distribution of found vertices as a function of $\phi$. The vertex distribution as a function of $z$ (figure 4.7 (b)) clearly shows a peak at $120\,cm$ due to the satellite bunch events.

The position of this vertex is given by the electron, whereas the main vertex found using the central jet chamber is found from the hadronic final state particles. The two methods of vertex finding are then independent and efficiencies for each can be calculated. The efficiency is found to be in close agreement with Monte-Carlo (within 5%, see figure 4.8), the differences being used to reweight the Monte-Carlo events.

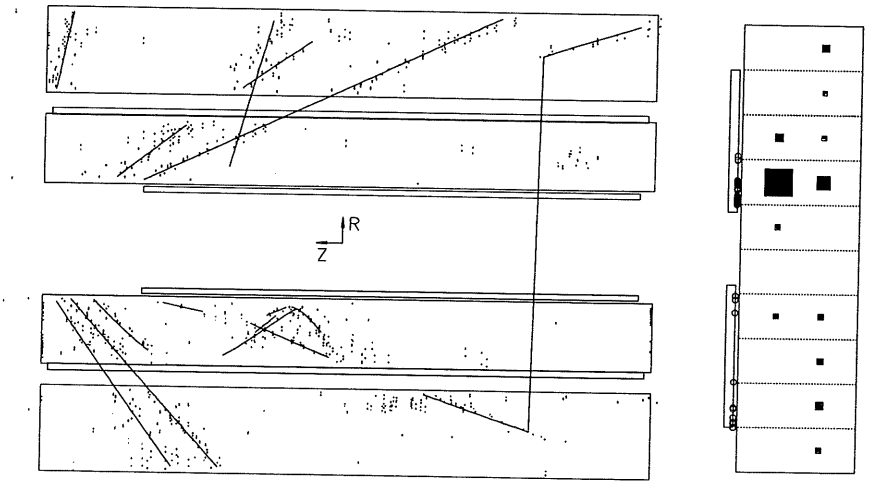


Figure 4.6: A side view of the central trackers and the BEMC showing a typical low $Q^2$ DIS event caused by a satellite bunch. The reconstructed vertex is at $117\,cm$ from the nominal interaction point.

### 4.7.5 Event Quality

Events with a large number of central tracks which do not come from the vertex (more than 75%) are rejected.

## 4.8 Residual Background

The main sources of background are from photoproduction and from the interaction of beam particles with residual gas or the beam wall.

Table 4.1 shows the numbers of pilot bunch events rejected by different cuts. As can be seen, no events survive the final selection. The background due to beam gas and beam wall interactions has been estimated at less than 0.3% [42].

## 4.9 Conclusion

The cuts used in selecting the DIS events are

- Time of flight requirement
- $10\,GeV \leq E_{BEMC} \leq 30\,GeV$
- the cluster centre of gravity is more than $16\,cm$ from the beam line
- $2.8^c \leq \theta_e \leq 3.01^c$
- Distance from cluster centre of gravity to the nearest BPC hit $< 4\,cm$
- Cluster radius $< 4\,cm$
- Hadronic fraction of BEMC cluster $< 0.8$
- $30\,GeV < \sum(E - P_z) < 70\,GeV$
- a vertex is reconstructed and $-50\,cm < Z_{vertex} < 50\,cm$
- More than 25% of tracks are fitted to the vertex

The distribution of the final event sample in the $x, Q^2$ plane is shown in figure 4.9, along with the boundaries defined by the energy and angle cuts.

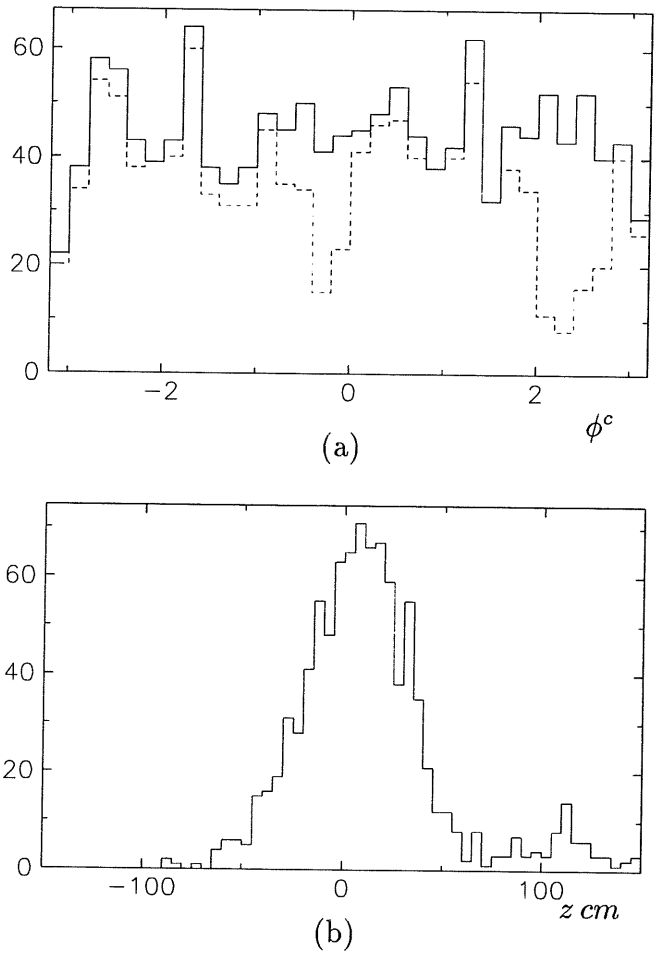


Figure 4.7: Figure (a) shows the $\phi$ of the scattered electron for all events (solid line) and for those with a CIP vertex (dashed line). Two regions of inefficiency due to hardware faults are clearly seen. Figure (b) shows the z distribution of the CIP vertices. The peak due to the satellite bunches is observed at $z \approx 120\,cm$.

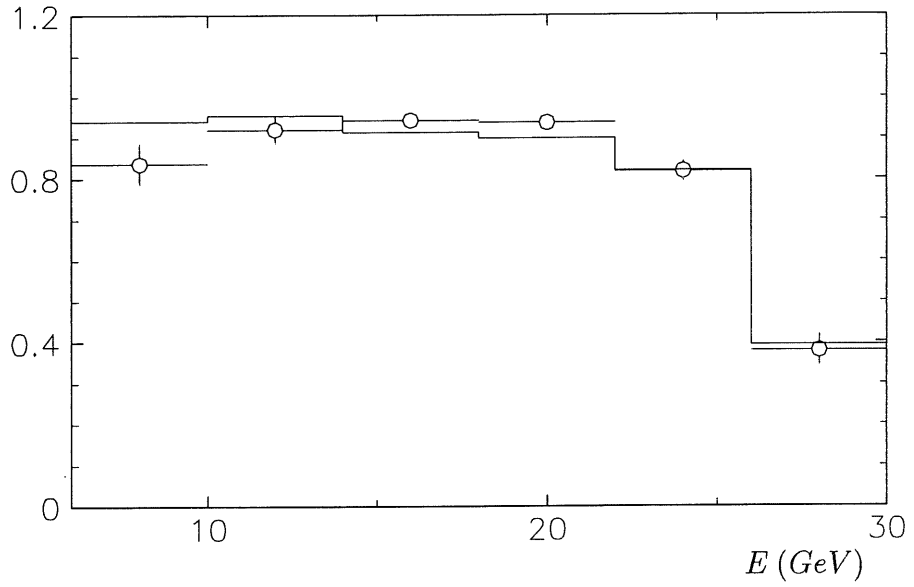


Figure 4.8: The vertex efficiency as calculated from data (points) compared with the DIS Monte-Carlo as a function of the candidate electron energy.

| | | Number of events remaining after cut | |
|---|---|---|---|
| Cut description | | Proton Pilot | Electron Pilot |
| 0 | DST class 11 | 165 | 34 |
| 1 | $6\,GeV < E_{BEMC} < 30\,GeV$<br>'Triangle' cut | 73 | 23 |
| 2 | Cut 1<br>$d(cluster - bpc) < 4\,cm$<br>Cluster radius $< 4\,cm$<br>Hadronic fraction $< 0.8$ | 21 | 6 |
| 3 | Cut 1<br>$\Sigma_{all}(E - P_z) < 30\,GeV$ | 35 | 3 |
| 4 | Cut 1<br>Reconstructed vertex<br>$-50\,cm < Z_{vertex} < 50\,cm$ | 8 | 3 |
| 5 | Cuts 1 & 2 & 3 | 1 | 3 |
| 6 | Cuts 1 & 2 & 3 & 4 | 0 | 0 |

Table 4.1: Numbers of events from pilot bunches that are removed by the cuts.

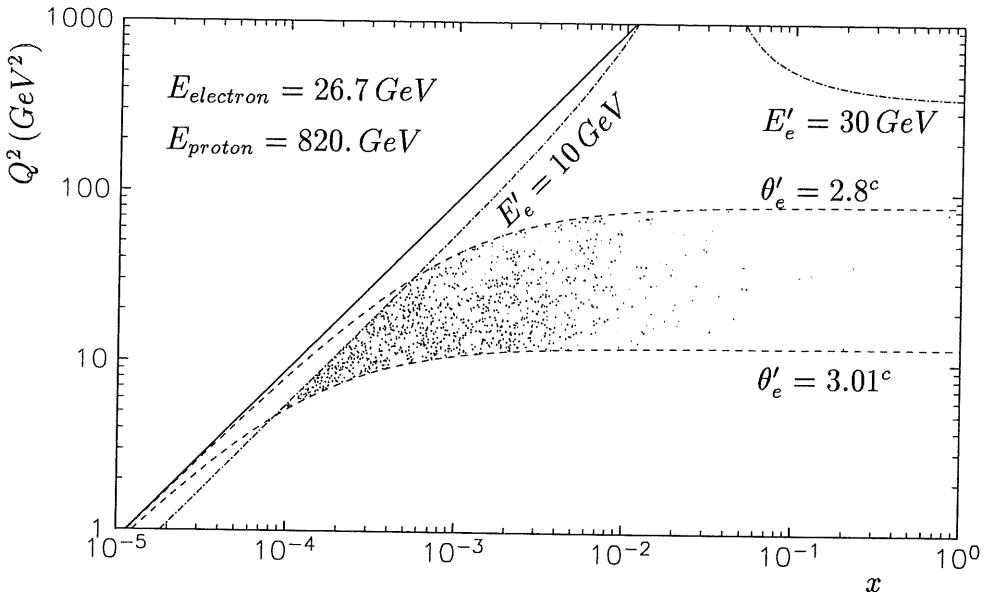


Figure 4.9: The distribution of events in the $x, Q^2$ plane for the final event sample. Also indicated are the cuts placed on energy and angle.

# Chapter 5

# The Proton Structure Function $F_2(x, Q^2)$ at low $x$

The determination of the proton structure function $F_2$ as a function of $x$ and $Q^2$ requires the determination of the event rate corrected for all sources of systematic bias. The technique used here is a general regularized unfolding procedure.

## 5.1 Unfolding

In this section only a brief discussion of unfolding is given, a more complete description is given in appendix A.

The extraction of a true rate of events from a measured rate is a non-trivial problem due to two main effects,

1. Limited acceptance resulting in the loss of events. This is due to the geometrical acceptance of the detector and the efficiency of selecting events.

2. Smearing. Not only are observable quantities measured with a limited resolution but their values may be shifted (for example due to energy leakage in a calorimeter).

The first effect causes a loss of events, the second a migration of events from one region of phase space to another. If the only effect is limited acceptance the procedure for extracting the true rate is relatively straightforward. However, if there are migrations then the problem becomes more complicated because the

acceptance of the detector as determined by Monte-Carlo will depend on the input structure function. Migrations also cause correlations between bins in unfolded distributions which can lead to wildly oscillating solutions from the unfolding. In this analysis these problems are overcome using the techniques of regularized unfolding as implemented in the program by V.Blobel [43]. The unfolding is only implemented in one dimension so that only $F_2(x)$ in a bin of $Q^2$ or $F_2(Q^2)$ in a bin of x can be determined.

The unfolding method consists of parameterizing the dependence of the Monte-Carlo input structure function parameterization on the unfolding variable $z$ (either $\log_{10}(x)$ or $\ln(Q^2)$) by a set of B-spline [47] functions. A histogram is made of a Monte-Carlo distribution and the acceptance for an input structure function equivalent to each of the B-splines is calculated. The Monte-Carlo histogram (plus a histogram of any background events) is then fitted to a histogram of the data using the maximum likelihood technique. Included in the fit is a term proportional to the total curvature of the calculated structure function. This term regularizes the result, suppressing statistically insignificant terms which oscillate rapidly in the solution. The solution is then in terms of a set of functions that are linear combinations of the B-splines, the sum of which gives the measured structure function, $F_2^{meas}(z)$. The average value of the structure function over a range of $z$ is then calculated from the integral of $F_2^{meas}(z)$. The range of $z$ is chosen such that correlations between bins are minimized. A very useful feature of the fitting procedure is that the Monte-Carlo events are re-weighted allowing distributions other than the ones used in the fit to be compared. The comparison of secondary distributions is an essential cross-check of the validity of the simulation of the events, as well as of the unfolding procedure.

In this analysis the DJANGO Monte-Carlo was used to generate DIS events including electroweak radiative corrections to order $\alpha_{EM}$. The main sample of events used for the unfolding was generated using the $MRSD\_$ structure function. Another sample, generated using the $MRSD_0$ parameterization was used to estimate any error in the method due to the assumed input structure function. For a non-radiative event, the event kinematics ($x$ and $Q^2$) at the event vertex are the same as those calculated from assuming a $26.7\,GeV$ incoming electron and the final state electron. For radiative events this is no longer true, as either the electron in the collision had a lower energy or the electron in the final state was more energetic after the collision. In the latter case the kinematics as calculated from the measured electron energy and angle in H1 is in fact the true kinematics at the event vertex (to within experimental errors) because the photon is almost always clustered with the final state electron due to the coarse granularity of the BEMC and because the radiated photon is emitted preferentially collinear to the electron. In the case of initial state radiation however, the kinematics will be wrongly determined. In the unfolding these effects are taken into account by

calculating the acceptance function between the true $x$ of the event and the $x$ as calculated from assuming an incident electron of $26.7\,GeV$ and the generated electron before any final state radiation.

The histogram for the fitting was chosen to be a two-dimensional histogram of the square root of the measured electron energy and the electron angle. This was chosen so that there would be no correlations between the measured quantities used in the fit and also so that the resolution would be approximately the same for all bins. The smallest bin size in the square root of the electron energy was $0.3\ \sqrt{GeV}$ ($cf\ \sigma_{BEMC}(E)/E \approx 0.1/\sqrt{(E)} \oplus 0.42/E$) and the smallest bin in angle was $20\,mrad$ ($cf$ BPC angular resolution $< 5\,mrad$).

## 5.2 Unfolding $F_2(x, Q^2)$ at fixed $Q^2$

Since the unfolding only unfolds the input distribution in one variable, it is necessary to bin the data in $Q^2$ in order to extract $F_2$ as a function of $x$. The bins are chosen to be much wider than the resolution of the detector to minimize the number of events migrating into the bin from other parts of the kinematic domain. Four bins are chosen, with limits of $Q^2$ (as measured from by the electron) of 5, 10, 20, 40 and 80 $GeV^2$. The values of $Q^2$ used in the unfolding are chosen to be the geometrical bin centre in all but the lowest $Q^2$ bin. In this case a value of $8.5\,GeV^2$ is chosen owing to the region of the kinematic domain that is selected.

### 5.2.1 $F_2(x)$ at $Q^2 = 8.5\,GeV^2$

The unfolding histogram was chosen to have 7 bins in $\sqrt{E_e}$, and 3 in $\theta_e$. The data sample contains 124 events, with a background estimated at $10 \pm 5$ events. Table 5.1 gives the results of the unfolding program, and figure 5.1 shows the comparison between data and unfolded Monte-Carlo events for various distributions.

The data are shown as hollow points, the DIS Monte-Carlo by a dashed line, the background events as a shaded histogram and the sum of the Monte-Carlos is shown by the solid line (see section 4.3 for details of the Monte-Carlos used). Figures (a) and (b) compare distributions of the square root of the electron energy and the electron scattering angle. Since these are the variables used in the fit, any significant discrepancy would be a cause for worry. Figures (c) and (d) are the electron energy and azimuthal angle and show that the modelling of the electron in the Monte-Carlos is reasonable. Figure (e) shows the distribution of the total hadronic final state as measured in the detector. This will depend on the fraction of the current jet that escapes the beam pipe and on the hadroniza-

| | $\log_{10}(x)$ | | $< F_2 >$ | stat | Error Correlations (%) | |
|---|---|---|---|---|---|---|
| | min | max | | error | Bin 1 | Bin 2 |
| Bin 1 | -3.82 | -3.61 | 1.333 | 0.219 | — | -18 |
| Bin 2 | -3.61 | -3.40 | 1.147 | 0.140 | -18 | — |

Table 5.1: Unfolding results for $Q^2 = 8.5\,GeV^2$.

tion model used in the Monte-Carlo. The transverse energy distribution shown in figure (f) should however be less sensitive to the hadronization as the total transverse energy in the event must be conserved. Large differences between the Monte-Carlo for this distribution or figure (h), the distribution of $y$ calculated from the hadrons, would indicate that the modelling of the kinematics of the events was poor.

### 5.2.2 $F_2(x)$ at $Q^2 = 15\,GeV^2$

The unfolding histogram was chosen to have 10 bins in $\sqrt{E_e}$, and 4 in $\theta_e$. The data sample contains 505 events, with a background estimated at $12 \pm 6$ events. The results of the unfolding are shown in table 5.2, and the comparison of data and Monte-Carlo is shown in figure 5.2. It is observed that the total hadronic energy in the final state (figure 5.2 (e)) shows some discrepancy between the data and Monte-Carlo. This is not fully understood. However, the observed energy is not used as a cut in the analysis. The smaller energy may imply a smaller vertex finding efficiency, but this is corrected for (section 4.7.4). Both transverse energy distribution and the distribution of $y_{hadrons}$ are reasonably described, giving confidence in the results obtained.

### 5.2.3 $F_2(x)$ at $Q^2 = 30\,GeV^2$

The unfolding histogram was chosen to have 10 bins in $\sqrt{E_e}$, and 3 in $\theta_e$. The data sample contains 340 events, with a negligible background. Table 5.3 shows the results from the unfolding. Figure 5.3 shows the comparison of data and Monte-Carlo. Here again some differences, that are not fully understood, are seen in the total hadronic final state energy. However, the $y_{hadrons}$ distribution is reasonably modelled, so the effect on the results should be small.

| | $\log_{10}(x)$ | | $< F_2 >$ | stat | Error correlations (%) | | | |
|---|---|---|---|---|---|---|---|---|
| | min | max | | error | Bin 1 | Bin 2 | Bin 3 | Bin 4 |
| Bin 1 | -3.59 | -3.33 | 1.435 | 0.125 | — | 14 | -10 | -2 |
| Bin 2 | -3.33 | -3.03 | 1.126 | 0.114 | 14 | — | -4 | 14 |
| Bin 3 | -3.03 | -2.53 | 0.903 | 0.105 | -10 | -4 | — | -47 |
| Bin 4 | -2.53 | -1.20 | 0.501 | 0.059 | -2 | 14 | -47 | — |

Table 5.2: Unfolding results for $Q^2 = 15\,GeV^2$.

| | $\log_{10}(x)$ | | $< F_2 >$ | stat | Error correlations (%) | | | |
|---|---|---|---|---|---|---|---|---|
| | min | max | | error | Bin 1 | Bin 2 | Bin 3 | Bin 4 |
| Bin 1 | -3.30 | -3.00 | 1.453 | 0.163 | — | 16 | 6 | 2 |
| Bin 2 | -3.00 | -2.69 | 1.228 | 0.144 | 16 | — | 0 | 16 |
| Bin 3 | -2.69 | -2.18 | 0.975 | 0.135 | 6 | 0 | — | -44 |
| Bin 4 | -2.18 | -1.40 | 0.583 | 0.101 | 2 | 16 | -44 | — |

Table 5.3: Unfolding results for $Q^2 = 30\,GeV^2$.

### 5.2.4 $F_2(x)$ at $Q^2 = 60\,GeV^2$

The unfolding histogram was chosen to have 4 bins in $\sqrt{E_e}$, and 5 in $\theta_e$. The data sample contains 132 events, with a negligible background. Table 5.4 shows the results from the unfolding. Figure 5.4 shows the comparison of data and Monte-Carlo.

| | $\log_{10}(x)$ | | $< F_2 >$ | stat | Error correlations (%) | |
|---|---|---|---|---|---|---|
| | min | max | | error | Bin 1 | Bin 2 |
| Bin 1 | -3.20 | -2.71 | 1.622 | 0.308 | — | 19 |
| Bin 2 | -2.71 | -2.00 | 1.142 | 0.118 | 19 | — |

Table 5.4: Unfolding results for $Q^2 = 60\,GeV^2$.

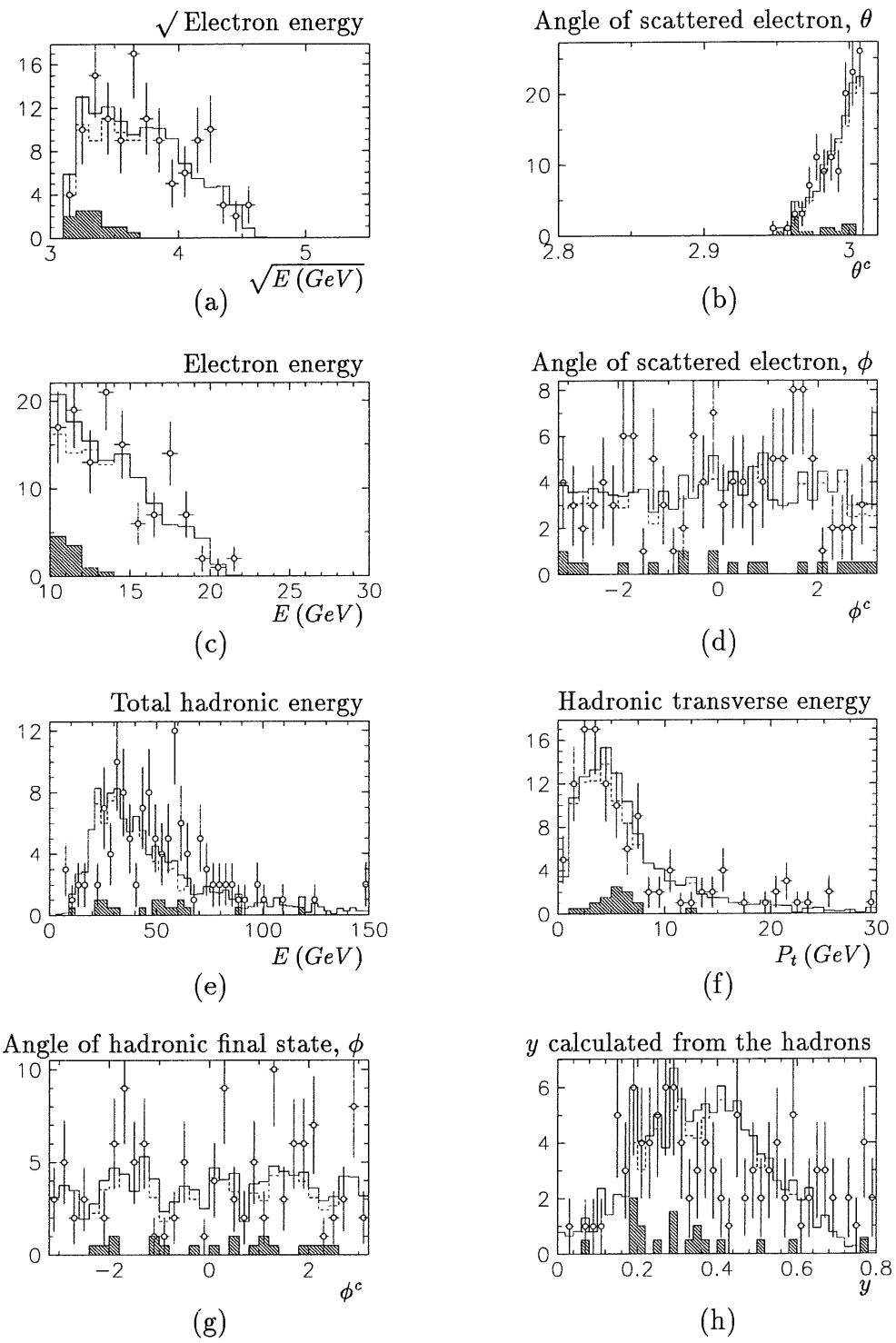


Figure 5.1: Plots comparing data and Monte-Carlo after the unfolding for $Q^2 = 8.5\,GeV^2$. The circles are the data points, the dash line is the DIS Monte-Carlo, the shaded histogram is the background and the solid line the sum of the Monte-Carlos. Figures (a)–(d) are of electronic variables, (e)–(h) are for the hadronic system.

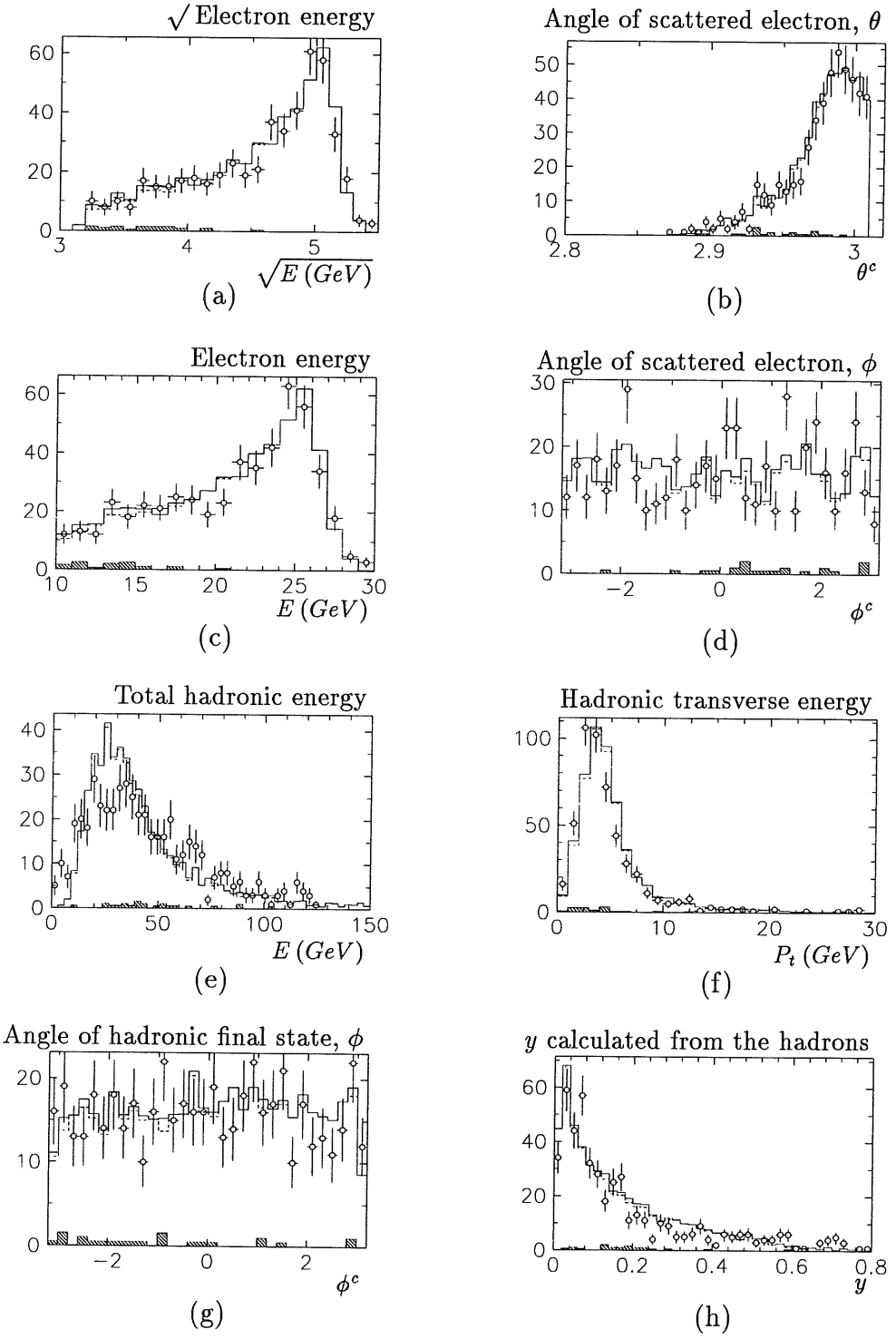


Figure 5.2: Plots comparing data and Monte-Carlo after the unfolding for $Q^2 = 15\,GeV^2$. The circles are the data points, the dash line is the DIS Monte-Carlo, the shaded histogram is the background and the solid line the sum of the Monte-Carlos. Figures (a)–(d) are of electronic variables, (e)–(h) are for the hadronic system.

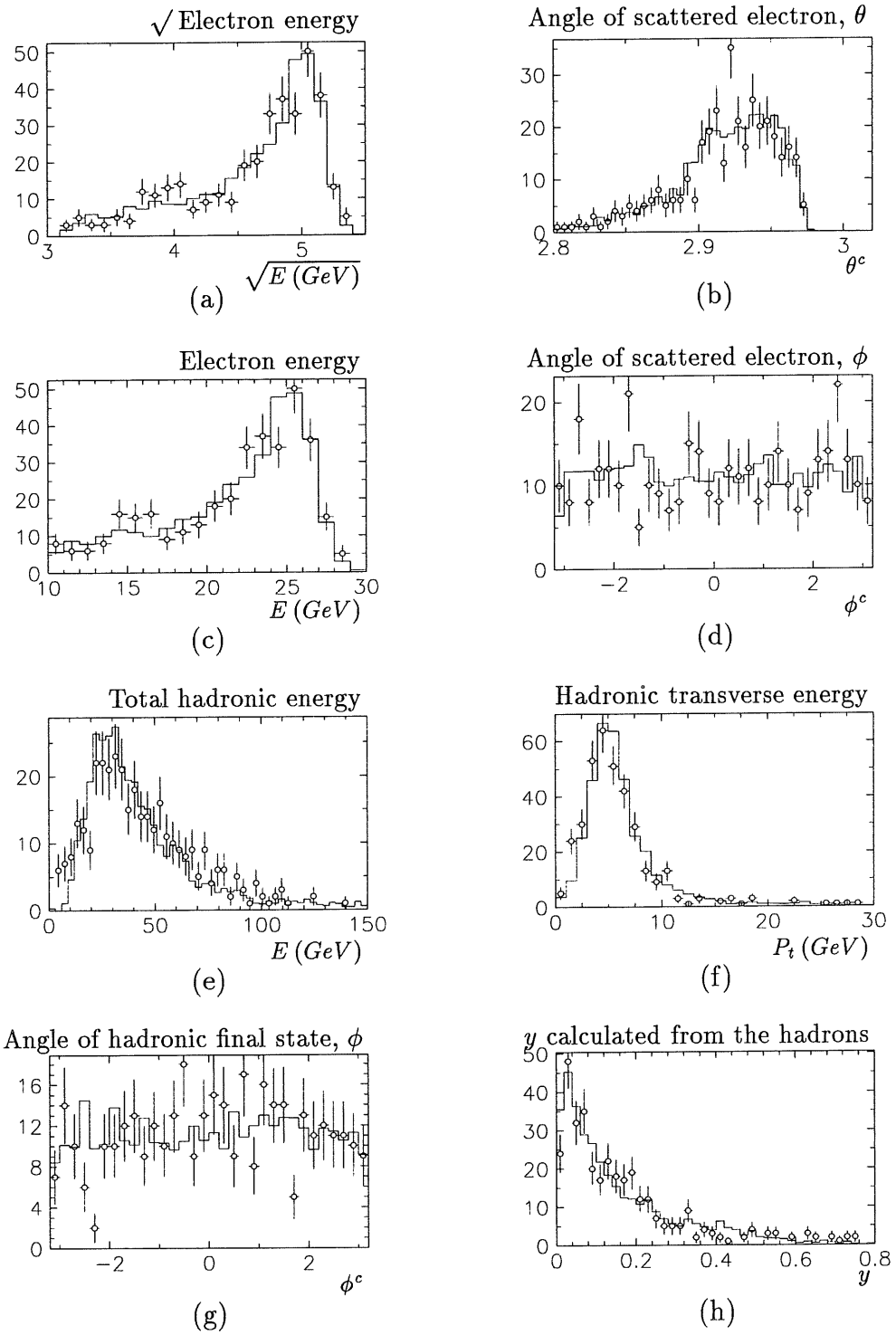


Figure 5.3: Plots comparing data and Monte-Carlo after the unfolding for $Q^2 = 30\,GeV^2$. The circles are the data points, the dash line is the DIS Monte-Carlo. No background events survived the cuts for this bin. Figures (a)–(d) are of electronic variables, (e)–(h) are for the hadronic system.

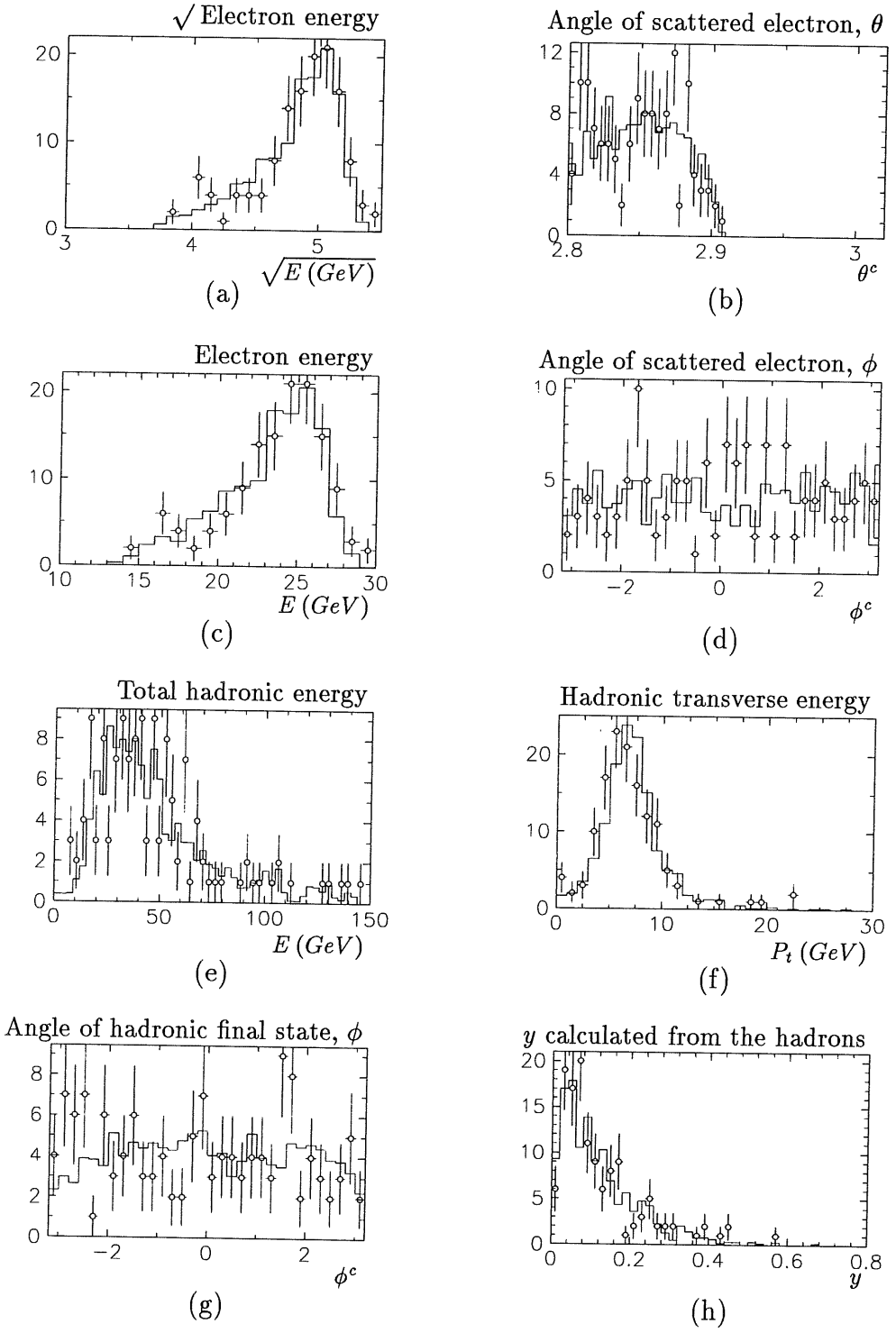


Figure 5.4: Plots comparing data and Monte-Carlo after the unfolding for $Q^2 = 60\,GeV^2$. The circles are the data points, the dash line is the DIS Monte-Carlo. No background events survived the cuts for this bin. Figures (a)–(d) are of electronic variables, (e)–(h) are for the hadronic system.

## 5.3 Sources of Systematic Error for the $x$ Dependence of $F_2$

Systematic errors that affect the whole data sample are

7% uncertainty in the luminosity. This far outweighs all uncertainties in the Monte-Carlo luminosity used for the normalization.

3% uncertainty in the ToF efficiency

2% uncertainty in the number of genuine DIS events lost due to demanding the reconstructed vertex be within $50\,cm$ of the nominal integration point.

giving an overall normalization uncertainty of 8%.

Other sources of error depend on the kinematics of the event and vary over the measured region. Several sources of systematic error due to the uncertainty of the calibration of the detector were considered, namely

- shifts of the energy scale by $\pm 2\%$
- the uncertainty in the resolution of the electron energy in the Monte-Carlo by $\pm 2\%$
- shifts of the electron angle by $\pm 5\,mrad$
- shifts of the energy scale used in the $\sum(E - P_z)$ cut of $\pm 7\%$

The above shifts were applied to the data and the unfolding was repeated. The systematic error was then taken to be the maximum of the difference of the nominal value from the values calculate with positive and negative shifts.

The uncertainty in the event selection also introduces sources of systematic error,

- the efficiency for event selection (electron identification, RVFIT) is only known to approximately $\pm 5\%$
- the vertex efficiency is only known to $5\% \rightarrow 7\%$

For these errors, the Monte-Carlo events were reweighted with efficiencies corresponding to the limits of the uncertainty. Again the maximum deviation from the nominal value was taken as the systematic error.

The error due to the photo-production background was included by repeating the unfolding using $\pm 0.5$ of the number of events from the Monte-Carlo.

The dependence of $F_2$ on the structure function used in the Monte-Carlo was investigated using a sample of events generated using DJANGO with the $MRSD_0$ structure function parameterization. The error was taken to be one half of the difference between the value calculated using $MRSD_0$ and that using $MRSD\_$. The effect of varying the parameters of the unfolding program was also investigated. The unfolding was repeated using different numbers of spline functions, but the effect was found to be smaller than the difference obtained by using different input structure functions in the Monte-Carlos provided that the number of splines was kept larger than the number of unfolded points.

The contribution to the total systematic error from each of the sources listed is shown in table 5.5, where the column headings have the following meanings:

- $E_e$, the electron energy scale,
- $\sigma(E_e)$, the resolution of the electron energy,
- $\theta_e$, the electron angle,
- ev. sel, the electron identification efficiency,
- Vtx, the vertex efficiency,
- $\gamma P$, the photo-production background,
- hadr. scale, the energy scale for the $\Sigma_{all}(E - P_z)$ cut,
- Str fun, the input structure function.

| $Q^2$ $(GeV^2)$ | bin | Tot sys | $E_e$ scale | $\sigma(E_e)$ | $\theta_e$ | ev. sel | Vtx | $\gamma P$ | hadr. scale | Str. fun |
|---|---|---|---|---|---|---|---|---|---|---|
| 8.5 | 1 | 0.25 | 0.15 | 0.02 | 0.15 | 0.06 | 0.08 | 0.06 | 0.01 | 0.03 |
| | 2 | 0.22 | 0.12 | 0.03 | 0.15 | 0.06 | 0.06 | 0.04 | 0.01 | 0.02 |
| 15.0 | 1 | 0.16 | 0.07 | 0.02 | 0.09 | 0.06 | 0.08 | 0.03 | 0.01 | 0.01 |
| | 2 | 0.16 | 0.10 | 0.03 | 0.08 | 0.05 | 0.07 | 0.01 | 0.01 | 0.02 |
| | 3 | 0.15 | 0.09 | 0.03 | 0.09 | 0.04 | 0.06 | 0.00 | 0.01 | 0.02 |
| | 4 | 0.12 | 0.06 | 0.05 | 0.06 | 0.04 | 0.05 | 0.00 | 0.02 | 0.01 |
| 30.0 | 1 | 0.21 | 0.13 | 0.03 | 0.13 | 0.07 | 0.08 | 0.02 | 0.01 | 0.03 |
| | 2 | 0.16 | 0.10 | 0.04 | 0.08 | 0.04 | 0.07 | 0.02 | 0.01 | 0.02 |
| | 3 | 0.14 | 0.07 | 0.03 | 0.10 | 0.05 | 0.05 | 0.01 | 0.01 | 0.01 |
| | 4 | 0.13 | 0.02 | 0.05 | 0.07 | 0.03 | 0.05 | 0.00 | 0.01 | 0.01 |
| 60. | 1 | 0.19 | 0.11 | 0.04 | 0.09 | 0.07 | 0.08 | 0.00 | 0.02 | 0.04 |
| | 2 | 0.21 | 0.16 | 0.04 | 0.09 | 0.05 | 0.07 | 0.00 | 0.01 | 0.03 |

Table 5.5: Systematic errors in the calculation of $F_2$ as a function of $x$ in bins of $Q^2$. The columns give the error due to the uncertainty in In addition to the above sources of error, there is an overall 8% normalization error.

## 5.4 Final Corrections

As has been mentioned, the values for $F_2(x, Q^2)$ extracted from the unfolding is an average value of $F_2(\log_{10}(x), Q^2)$ over a bin of $\log_{10}(x)$. The average value $\overline{F_2}$ can be converted to a value at a fixed $x$ using

$$F_2(x_0, Q_0^2) \approx F_2^{theory}(x_0, Q_0^2) \cdot \frac{\int_{bin} dz}{\int_{bin} F_2^{theory}(z, Q_0^2) dz} \cdot \overline{F_2} \tag{5.1}$$

where $z = \log(x)$, and $F_2^{theory}$ is a structure function parameterization. This can be calculated for a number of parameterizations and provided the differences are small the approximation can be assumed to be valid. The differences between the corrections as calculated using the $MRSD_-$ or the $MRSD_0$ structure function parameterization are less than one percent. The correction is small, always less than 5%. There remains one other correction due to possible effects of the longitudinal structure function, ie. the result calculated so far have the assumption that $R = 0$ in the differential cross section (equation 2.24, section 2.3). However, in order to allow a valid comparison with structure function parameterizations that are calculated to next to leading order in $\alpha_s$ a correction should be made. For this analysis, $R$ is calculated to NLO for the $MRSD_-$ parameterization using the EPOKEPIK [44] package at the chosen values of $x$ and $Q^2$ for the points. The value of $F_2$ is then corrected by a factor (cf equations 2.24 and 2.25)

$$\frac{2 \cdot (1 - y) + y^2}{2 \cdot (1 - y) + \frac{y^2}{1+R}}$$

This correction is always less than 8%. No error is assigned to this correction as it is a trivial problem to make better corrections should the value of $R$ be more accurately estimated.

The results with all corrections made are given in table 5.6 and compared with various structure function parameterizations in figure 5.5. The structure function is seen to rise with falling $x$ as predicted by some of the models with a high gluon density in the proton.

| $Q^2\,(GeV^2)$ | $x$ | $y$ | $F_2$ | $\sigma_{stat}$ | $\sigma_{syst}$ | $R$ |
|---|---|---|---|---|---|---|
| 8.5 | 0.00019 | 0.51 | 1.44 ± 0.36 | 0.24 | 0.27 | 0.52 |
| | 0.00031 | 0.31 | 1.18 ± 0.27 | 0.14 | 0.23 | 0.49 |
| 15.0 | 0.00035 | 0.49 | 1.52 ± 0.19 | 0.13 | 0.14 | 0.39 |
| | 0.00066 | 0.26 | 1.15 ± 0.19 | 0.11 | 0.16 | 0.36 |
| | 0.00167 | 0.10 | 0.92 ± 0.19 | 0.11 | 0.15 | 0.32 |
| | 0.01370 | 0.01 | 0.54 ± 0.14 | 0.06 | 0.13 | 0.21 |
| 30.0 | 0.0007 | 0.49 | 1.53 ± 0.28 | 0.17 | 0.22 | 0.30 |
| | 0.00143 | 0.24 | 1.25 ± 0.22 | 0.15 | 0.16 | 0.28 |
| | 0.00367 | 0.09 | 0.99 ± 0.20 | 0.14 | 0.14 | 0.24 |
| | 0.0162 | 0.02 | 0.60 ± 0.16 | 0.10 | 0.13 | 0.18 |
| 60.0 | 0.0011 | 0.60 | 1.78 ± 0.39 | 0.34 | 0.21 | 0.25 |
| | 0.0044 | 0.16 | 1.20 ± 0.25 | 0.12 | 0.22 | 0.21 |

Table 5.6: The fully corrected values of $F_2(x, Q^2)$ as a function of $x$ for different bins in $Q^2$. The total error is calculated by summing the statistical and systematic errors in quadrature. There is an additional 8% normalization error on all the points.

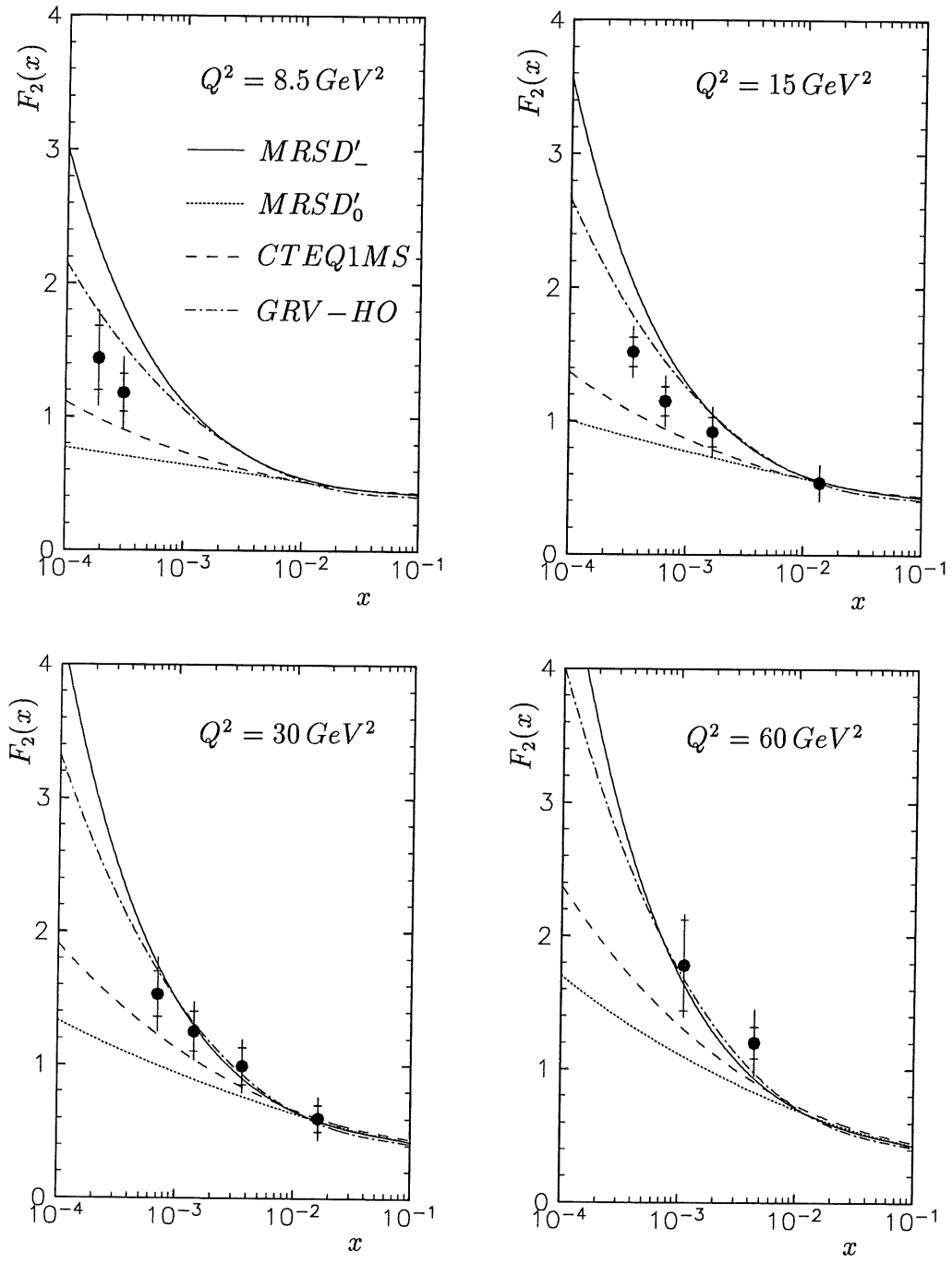


Figure 5.5: The measured structure function $F_2(x, Q^2)$ as a function of $x$ for bins of $Q^2$. The error bars show the statistical and total errors for the points, excluding an overall normalization uncertainty of 8%. The points are compared with some structure function parameterizations obtained from extrapolating fits of lower energy, higher $x$, data.

## 5.5 Unfolding $F_2(x, Q^2)$ at fixed $x$

For this analysis the events are binned into regions of $x$. Using the scattered electron to determine the value of $x$ results in the large variations in the resolution over the accessible kinematic region. The binning in $x$ was chosen such that the bins are always larger than the resolution in $x$ and such that the events were fairly uniformly distributed amongst the bins. The bin limits chosen were $\log_{10}(x)$ from -3.5 to -3.2, -3.2 to -2.9, -2.9 to -2.5 and -2.5 to -2.0. The values of $x$ used for the unfolding were chosen to be the geometrical centre of the $\log_{10}(x)$ bin. To remove very poorly events with very poorly reconstructed $x$, events with $y_{electron} < 0.05$ were removed. The other cuts used were the same as for the unfolding in $Q^2$.

### 5.5.1 $F_2(Q^2)$ at $\log_{10}(x) = -3.35$

The histogram used for the fitting had 4 bins in $\sqrt{E}$ and 6 in $\theta$. The data sample consists of 174 events with an estimated background of $13 \pm 6$ events. The results of the unfolding are shown in table 5.7 and the histograms comparing data and Monte-Carlo are shown in figure 5.6.

| | $\ln(Q^2)$ | | $< F_2 >$ | stat | Error Correlations (%) | |
|---|---|---|---|---|---|---|
| | min | max | | error | Bin 1 | Bin 2 |
| Bin 1 | 2.44 | 2.86 | 1.302 | 0.148 | — | 24 |
| Bin 2 | 2.86 | 3.42 | 1.398 | 0.285 | 24 | — |

Table 5.7: Unfolding results for $\log_{10}(x) = -3.35$. The values of $\ln(Q^2)$ are calculated with $Q^2$ in $GeV^2$.

### 5.5.2 $F_2(Q^2)$ at $\log_{10}(x) = -3.05$

The histogram used for the fitting had 2 bins in $\sqrt{E}$ and 6 in $\theta$. The data sample consists of 186 events with an estimated background of $1 \pm 1$ events. The results of the unfolding are shown in table 5.8 and the histograms comparing data and Monte-Carlo are shown in figure 5.7.

| | $\ln(Q^2)$ | | $< F_2 >$ | stat | Error correlations (%) | | | |
|---|---|---|---|---|---|---|---|---|
| | min | max | | error | Bin 1 | Bin 2 | Bin 3 | Bin 4 |
| Bin 1 | 2.27 | 2.76 | 1.053 | 0.119 | — | 2 | -6 | 3 |
| Bin 2 | 2.76 | 3.11 | 1.151 | 0.145 | 2 | — | 20 | -6 |
| Bin 3 | 3.11 | 3.47 | 1.212 | 0.165 | -6 | 20 | — | 10 |
| Bin 4 | 3.47 | 4.00 | 1.310 | 0.222 | 3 | -6 | 10 | — |

Table 5.8: Unfolding results for $\log_{10}(x) = -3.05$. The values of $\ln(Q^2)$ are calculated with $Q^2$ in $GeV^2$.

### 5.5.3 $F_2(Q^2)$ at $\log_{10}(x) = -2.70$

The histogram used for the fitting had 3 bins in $\sqrt{E}$ and 8 in $\theta$. The data sample consists of 257 events with negligible background. The results of the unfolding are shown in table 5.9 and the histograms comparing data and Monte-Carlo are shown in figure 5.8.

| | $\ln(Q^2)$ | | $< F_2 >$ | stat | Error correlations (%) | | | |
|---|---|---|---|---|---|---|---|---|
| | min | max | | error | Bin 1 | Bin 2 | Bin 3 | Bin 4 |
| Bin 1 | 2.37 | 2.84 | 0.925 | 0.106 | — | 22 | -5 | -2 |
| Bin 2 | 2.84 | 3.25 | 1.088 | 0.106 | 22 | — | 32 | -5 |
| Bin 3 | 3.25 | 3.58 | 1.219 | 0.128 | -5 | 32 | — | 14 |
| Bin 4 | 3.58 | 4.25 | 1.207 | 0.227 | -2 | -5 | -14 | — |

Table 5.9: Unfolding results for $\log_{10}(x) = -2.7$. The values of $\ln(Q^2)$ are calculated with $Q^2$ in $GeV^2$.

### 5.5.4 $F_2(Q^2)$ at $\log_{10}(x) = -2.25$

The histogram used for the fitting had 1 bins in $\sqrt{E}$ and 8 in $\theta$. The data sample consists of 191 events with negligible background. The results of the unfolding are shown in table 5.10 and the histograms comparing data and Monte-Carlo are shown in figure 5.9.

| | $\ln(Q^2)$ | | $< F_2 >$ | stat | Error correlations (%) | | | |
|---|---|---|---|---|---|---|---|---|
| | min | max | | error | Bin 1 | Bin 2 | Bin 3 | Bin 4 |
| Bin 1 | 3.03 | 3.42 | 0.648 | 0.121 | — | 22 | -7 | 1 |
| Bin 2 | 3.42 | 3.80 | 0.805 | 0.126 | 22 | — | 29 | -4 |
| Bin 3 | 3.80 | 4.12 | 0.906 | 0.140 | -7 | 29 | — | 11 |
| Bin 4 | 4.12 | 4.60 | 1.012 | 0.189 | 1 | -4 | 11 | — |

Table 5.10: Unfolding results for $\log_{10}(x) = -2.25$. The values of $\ln(Q^2)$ are calculated with $Q^2$ in $GeV^2$.

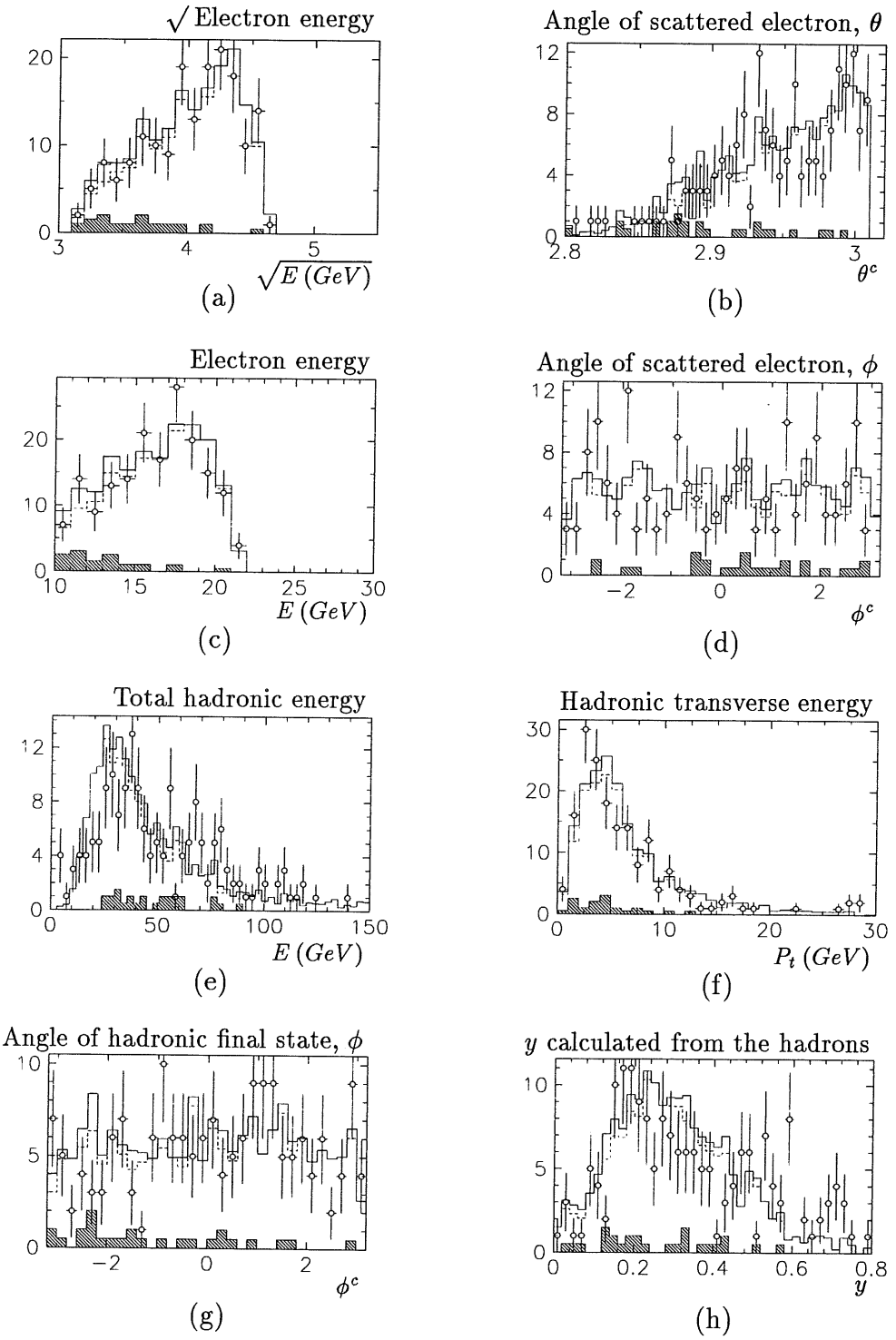


Figure 5.6: Plots comparing data and Monte-Carlo after the unfolding for $\log_{10}(x) = -3.35$. The circles are the data points, the dash line is the unfolded DIS Monte-Carlo, the shaded histogram is the background and the solid line the sum of the Monte-Carlos. Figures (a)–(d) are of electronic variables, (e)–(h) are for the hadronic system.

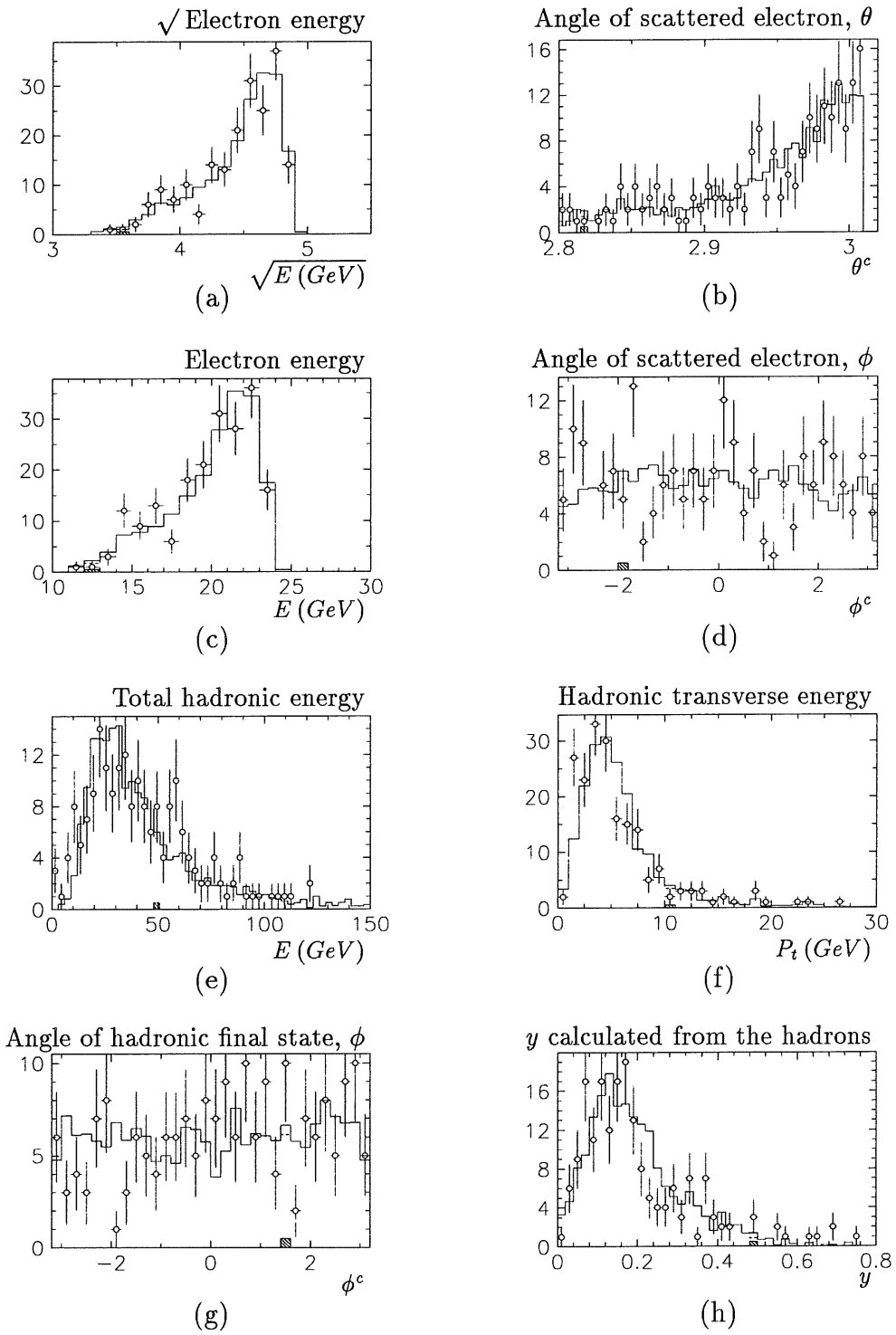


Figure 5.7: Plots comparing data and Monte-Carlo after the unfolding for $\log_{10}(x) = -3.05$. The circles are the data points, the dash line is the unfolded DIS Monte-Carlo, the shaded histogram is the background and the solid line the sum of the Monte-Carlos. Figures (a)–(d) are of electronic variables, (e)–(h) are for the hadronic system.

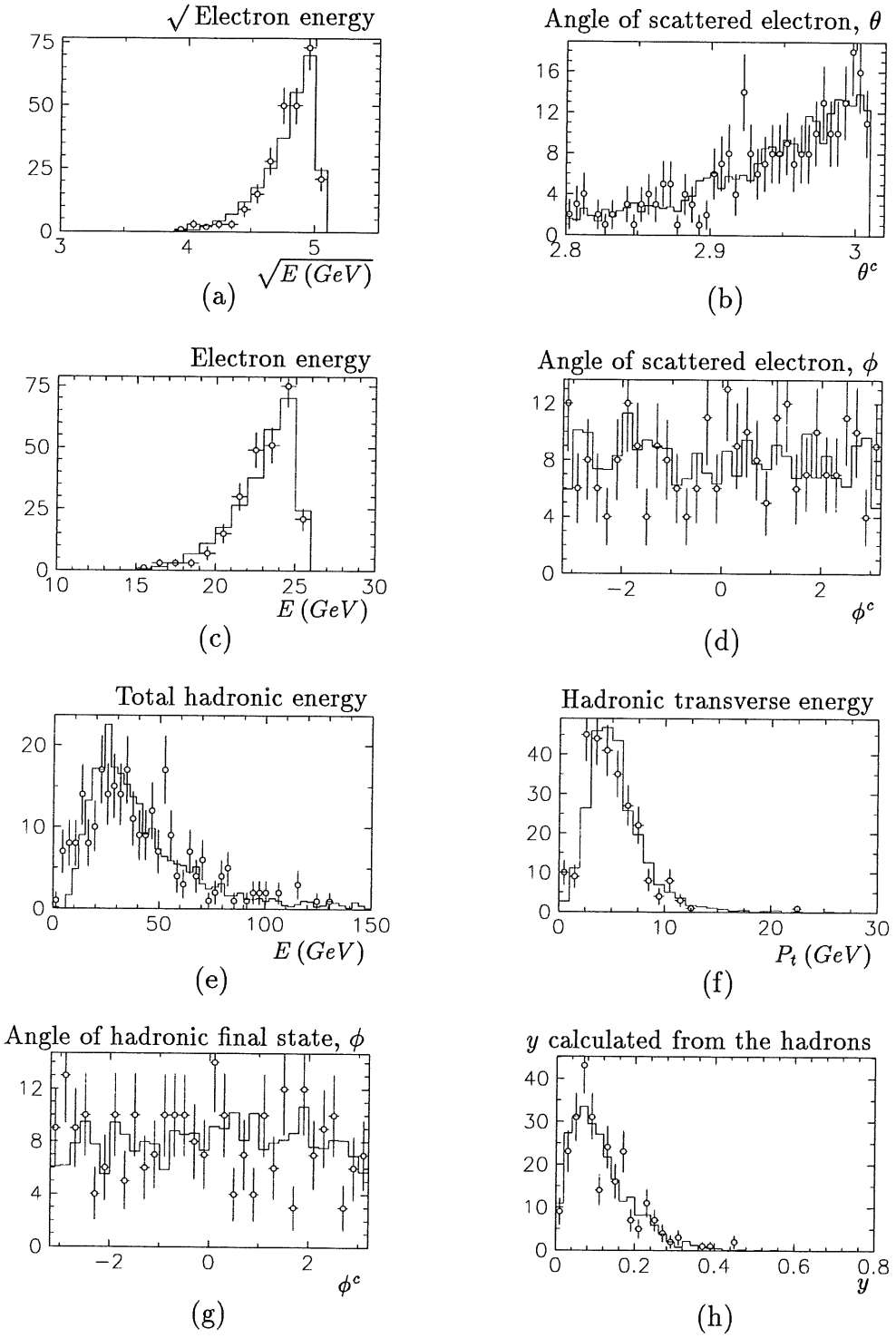


Figure 5.8: Plots comparing data and Monte-Carlo after the unfolding for $\log_{10}(x) = -2.7$. The circles are the data points, the solid line is the unfolded DIS Monte-Carlo. No background events survived the cuts for this bin. Figures (a)–(d) are of electronic variables, (e)–(h) are for the hadronic system.

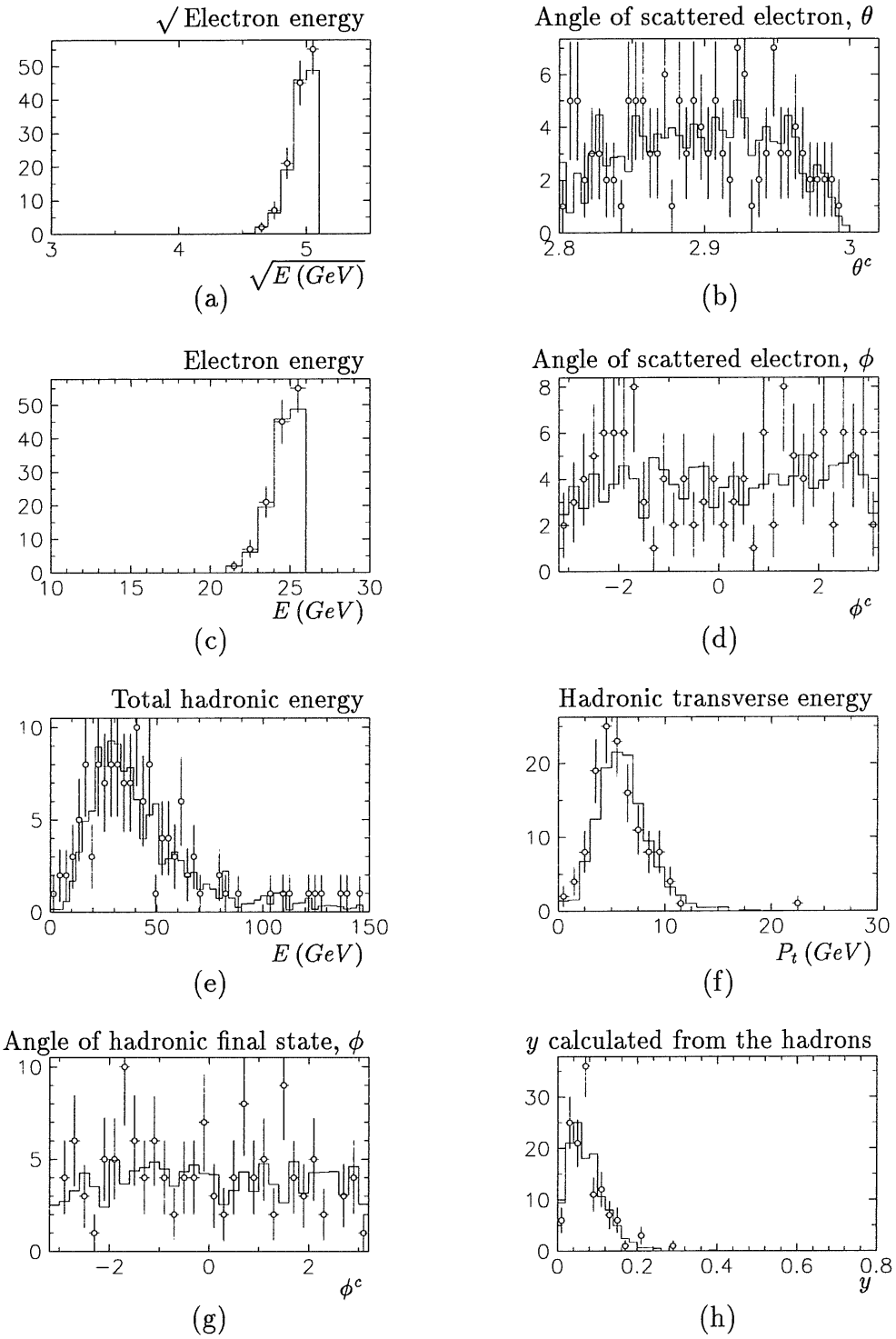


Figure 5.9: Plots comparing data and Monte-Carlo after the unfolding for $\log_{10}(x) = -2.25$. The circles are the data points, the solid line is the unfolded DIS Monte-Carlo. No background events survived the cuts for this bin. Figures (a)–(d) are of electronic variables, (e)–(h) are for the hadronic system.

## 5.6 Sources of Systematic Error for the $Q^2$ Dependence of $F_2$

The sources of systematic error as listed in section 5.3 were considered.

The contribution to the total systematic error from each of the sources listed is shown in table 5.11, where the column headings have the following meanings:

- $E_e$, the electron energy scale,
- $\sigma(E_e)$, the resolution of the electron energy,
- $\theta_e$, the electron angle,
- ev. sel, the electron identification efficiency,
- Vtx, the vertex efficiency,
- $\gamma P$, the photo-production background,
- hadr. scale, the energy scale for the $\Sigma_{all}(E - P_z)$ cut,
- Str fun, the input structure function.

| $\log_{10}(x)$ $(GeV^2)$ | bin | Tot sys | $E_e$ scale | $\sigma(E_e)$ | $\theta_e$ | ev. sel | Vtx | $\gamma P$ | hadr. scale | Str. fun |
|---|---|---|---|---|---|---|---|---|---|---|
| -3.35 | 1 | 0.18 | 0.07 | 0.04 | 0.09 | 0.08 | 0.08 | 0.05 | 0.02 | 0.04 |
| | 2 | 0.19 | 0.07 | 0.03 | 0.12 | 0.07 | 0.08 | 0.05 | 0.02 | 0.03 |
| -3.05 | 1 | 0.16 | 0.04 | 0.03 | 0.13 | 0.05 | 0.06 | 0.02 | 0.01 | 0.02 |
| | 2 | 0.14 | 0.04 | 0.03 | 0.10 | 0.05 | 0.06 | 0.02 | 0.02 | 0.01 |
| | 3 | 0.14 | 0.05 | 0.03 | 0.09 | 0.06 | 0.06 | 0.02 | 0.01 | 0.02 |
| | 4 | 0.13 | 0.07 | 0.04 | 0.05 | 0.05 | 0.06 | 0.01 | 0.02 | 0.01 |
| -2.7 | 1 | 0.18 | 0.13 | 0.03 | 0.08 | 0.05 | 0.06 | 0.00 | 0.01 | 0.02 |
| | 2 | 0.15 | 0.09 | 0.04 | 0.06 | 0.05 | 0.07 | 0.00 | 0.02 | 0.02 |
| | 3 | 0.18 | 0.09 | 0.04 | 0.11 | 0.06 | 0.07 | 0.00 | 0.01 | 0.02 |
| | 4 | 0.15 | 0.09 | 0.05 | 0.05 | 0.06 | 0.07 | 0.00 | 0.02 | 0.01 |
| -2.25 | 1 | 0.15 | 0.10 | 0.03 | 0.09 | 0.04 | 0.05 | 0.00 | 0.01 | 0.01 |
| | 2 | 0.16 | 0.09 | 0.04 | 0.09 | 0.05 | 0.06 | 0.00 | 0.01 | 0.02 |
| | 3 | 0.14 | 0.07 | 0.05 | 0.08 | 0.05 | 0.05 | 0.00 | 0.02 | 0.03 |
| | 4 | 0.14 | 0.06 | 0.05 | 0.09 | 0.05 | 0.05 | 0.00 | 0.01 | 0.03 |

Table 5.11: Systematic errors in the calculation of $F_2$ as a function of $Q^2$ in bins of $x$. In addition to the above sources of error, there is an overall 8% normalization error.

## 5.7 Final Corrections

As in the analysis of the $x$ dependence of the structure function, final corrections are made for the binning of the data and for $R$ (section 5.4), but in this case $z$ in equation 5.1 is now $\ln(Q^2)$. The resulting measurements of the $Q^2$ dependence of $F_2$ are given in table 5.12 and shown in figure 5.10.

## 5.8 Consistency of the Measurements of $F_2$

It has been stressed that the unfolding procedure is done only for one dimensional distribution but that the unfolding of the proton structure is a two dimensional problem. The validity of the results obtained using the unfolding has been checked comparing the values of the structure function obtained from unfolding as a function of $x$ with those from the unfolding in $Q^2$.

The comparison is shown in figure 5.11. The comparison is made at a two values of $Q^2$ where the two sets of results have data points that cover the same region of phase space. The solid triangles in the figure are the results of unfolding as a function of $x$. The hollow points are taken from the values of $F_2$ calculated in the unfolding as a function of $Q^2$. Where there was no measured value of $F_2$ at the required $Q^2$ it was calculated assuming a linear interpolation between the surrounding values. The 'error' bars are then taken to be the weighted average of the errors of the points used to calculate the $F_2$. The results appear to be consistent which is taken as evidence that binning the event sample in either $x$ or $Q^2$ did not bias the results from the unfolding procedure.

| $\log_{10}(x)$ | $Q^2(GeV)^2$ | $y$ | $F_2$ | $\sigma_{stat}$ | $\sigma_{syst}$ | $R$ |
|---|---|---|---|---|---|---|
| -3.35 | 14.2 | 0.36 | 1.34 ± 0.24 | 0.15 | 0.19 | 0.38 |
| | 23.1 | 0.591 | 1.49 ± 0.37 | 0.31 | 0.21 | 0.33 |
| -3.05 | 12.4 | 0.16 | 1.06 ± 0.20 | 0.12 | 0.16 | 0.37 |
| | 18.8 | 0.24 | 1.16 ± 0.21 | 0.15 | 0.15 | 0.32 |
| | 26.8 | 0.34 | 1.24 ± 0.22 | 0.17 | 0.14 | 0.30 |
| | 41.8 | 0.54 | 1.37 ± 0.27 | 0.23 | 0.14 | 0.27 |
| -2.70 | 13.5 | 0.08 | 0.93 ± 0.21 | 0.11 | 0.18 | 0.32 |
| | 21.0 | 0.12 | 1.09 ± 0.19 | 0.11 | 0.15 | 0.29 |
| | 30.4 | 0.17 | 1.22 ± 0.22 | 0.13 | 0.18 | 0.26 |
| | 50.2 | 0.29 | 1.22 ± 0.27 | 0.23 | 0.15 | 0.24 |
| -2.25 | 25.2 | 0.05 | 0.65 ± 0.19 | 0.12 | 0.15 | 0.23 |
| | 37.0 | 0.08 | 0.81 ± 0.21 | 0.13 | 0.16 | 0.22 |
| | 52.4 | 0.11 | 0.91 ± 0.20 | 0.14 | 0.14 | 0.20 |
| | 78.2 | 0.16 | 1.01 ± 0.24 | 0.19 | 0.14 | 0.19 |

Table 5.12: The fully corrected values of $F_2(x, Q^2)$ as a function of $Q^2$ for different bins in $x$. The total error is calculated by summing the statistical and systematic errors in quadrature. There is an additional 8% normalization error on all the points.

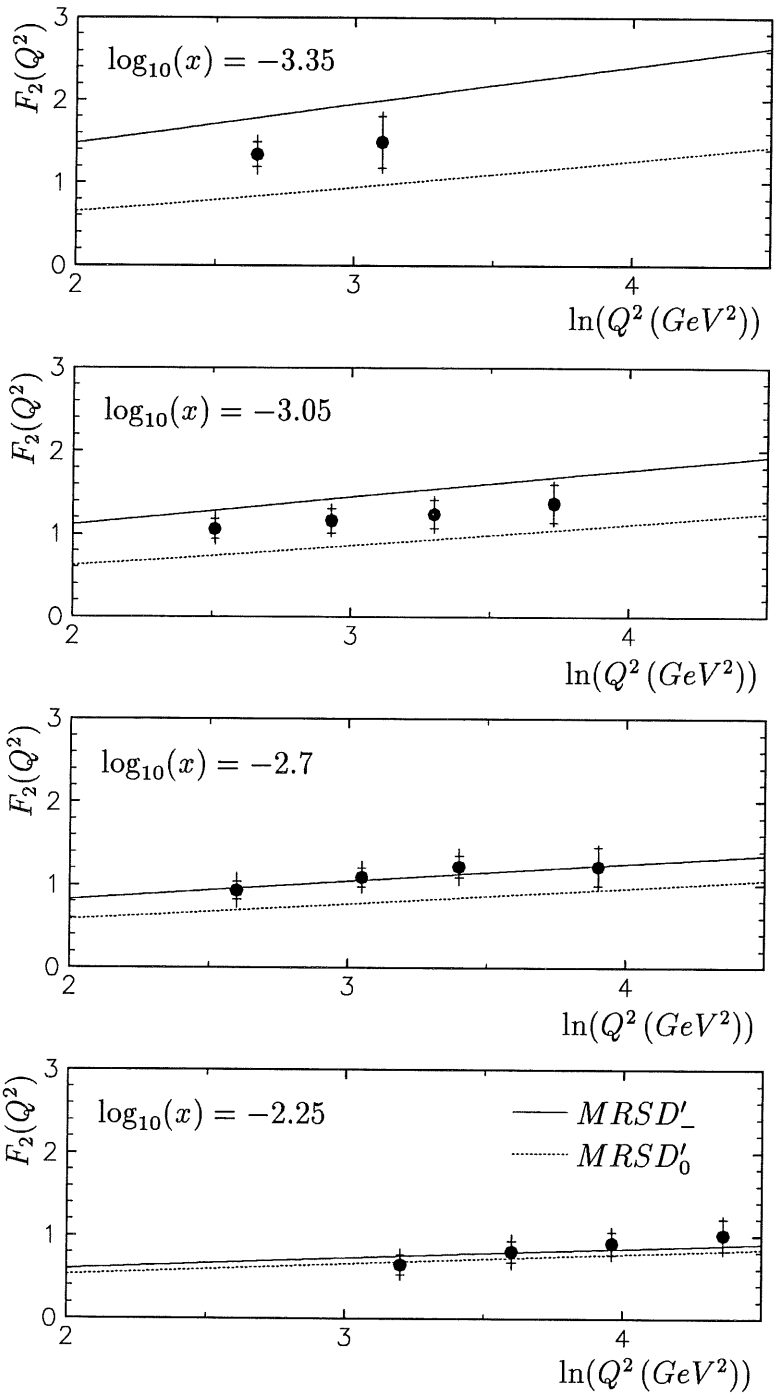


Figure 5.10: The measured structure function $F_2(x, Q^2)$ as a function of $Q^2$ for bins of $x$. The error bars show the statistical and total errors for the points, excluding an overall normalization uncertainty of 8%. The points are compared with some structure function parameterizations obtained from extrapolating fits to lower energy data.

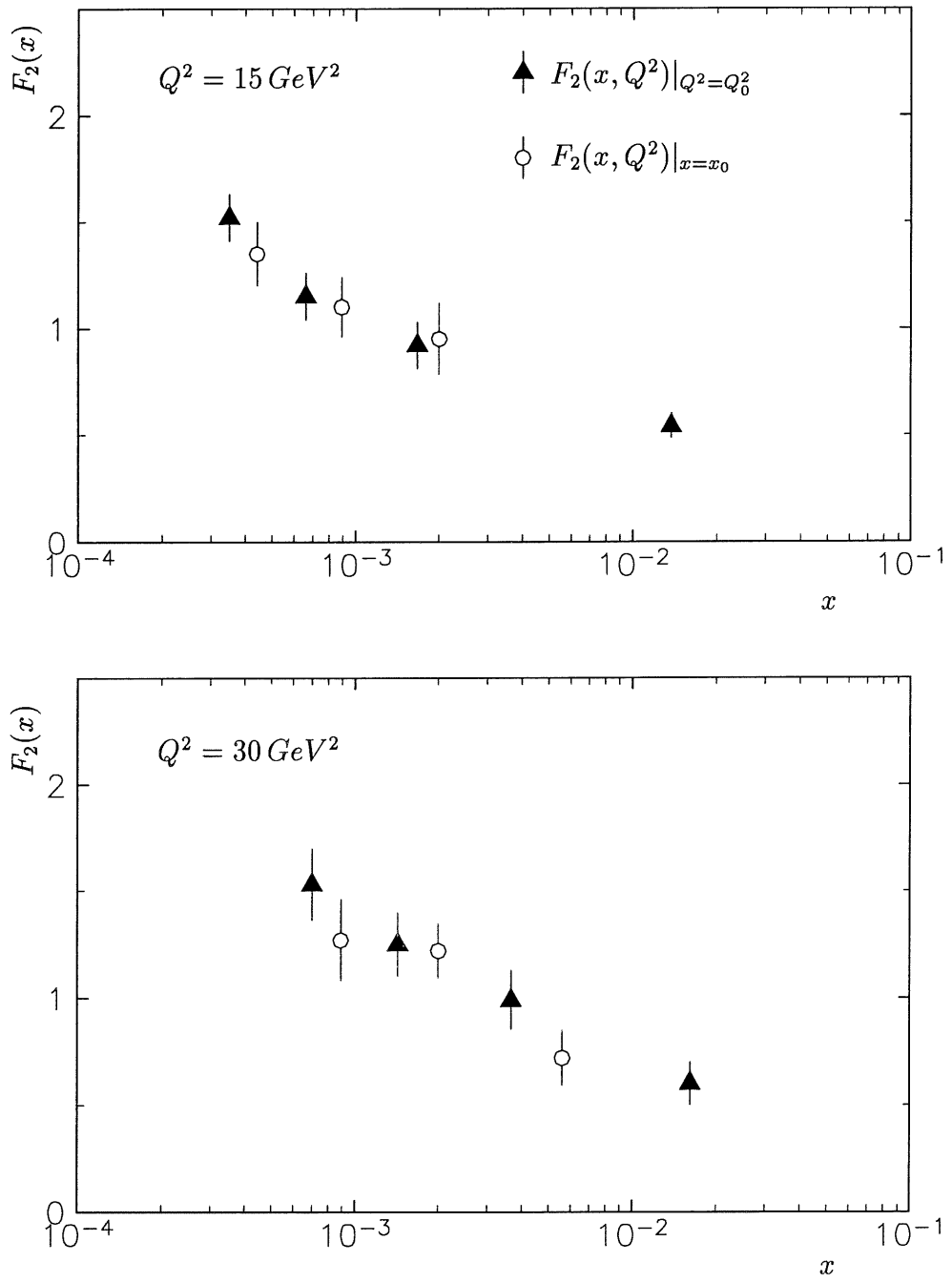


Figure 5.11: The comparison of the structure function values as unfolded as a function of $x$ at fixed $Q^2$ ($F_2(x,Q^2)|_{Q^2=Q_0^2}$) and $Q^2$ at fixed $x$ ($F_2(x,Q^2)|_{x=x_0}$). The solid triangles are the data points as unfolded in the $Q^2$ bins centred on $15\,GeV^2$ and $30\,GeV^2$, the error bars are only statistical errors. The hollow points are calculated from the unfolding as a function of $Q^2$, with an estimate of the statistical error.

## 5.9 The Proton Structure Function at low $x$

Figure 5.12 shows the results of the analysis of the $x$ dependence of the structure function together with previous measurements. There is clearly no evidence for any discontinuity between either the normalization or the $x$ dependance measured here and previous, lower energy, higher $x$ measurements (NMC [8] and BCDMS [9]). To within the limited expermental accuracy, the $Q^2$ dependence of $F_2$ follows the well established trend of the higher $x$ data (figures 2.7 and 5.10).

The $x$ dependence of $F_2$ in the DIS domain, figure 5.12 shows a substantial increase as $x$ decreases in the range $2 \cdot 10^{-4} \leq x \leq 2 \cdot 10^{-2}$. The results presented here reveal, at face value, the largest variation of $F_2$ with $x$ away from 'threshold' ($x = 1$). Given such a large rise, it is intriguing to speculate on the possibility of new QCD physics associated with a high gluon density at small $x$. The data clearly favours the $MRSD'_-$ parton density distribution (which has a BFKL motivated $x$ dependance of the gluon density, $xg(x, Q^2) \sim x^{-0.5}$) over the $MRSD'_0$, suggesting that BFKL evolution may be driving the structure function evolution. However, the $GRV$ parton density distributions also give a steeply rising structure function, but without the assumption of BFKL. Both the $MRS$ and $GRV$ parton density distributions have the sea quark distribution driven by the gluon distribution and, in the $Q^2$ range considered here, have large gluon densities at small $x$ (figures 2.8 and 2.10). On is thus led to the view that the rise in $F_2$, which measures the sum of the charged quark distributions, can be attributed to a large gluon density. Unambiguous demonstration of this will only come with precision measurements of the $Q^2$ dependence of the structure function.

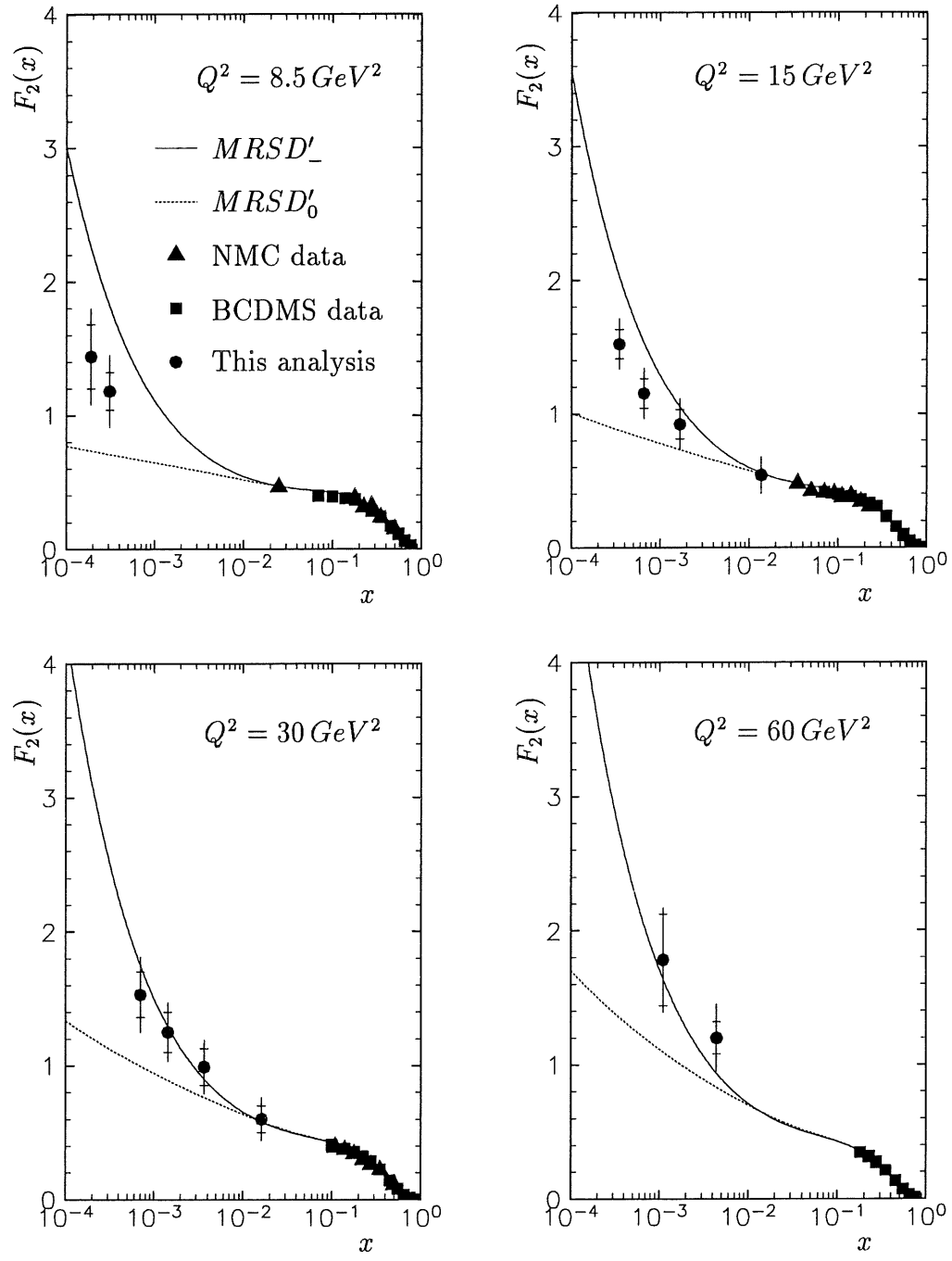


Figure 5.12: The structure function of the proton, $F_2^p(x, Q^2)$, at fixed $Q^2$. The measurements from this analysis and previous, lower energy, higher $x$ experiments (NMC [8] and BCDMS [9]) are shown, along with the prediction from the $MRS$ parton density distibutions.

# Chapter 6

# Summary and Conclusion

The structure function of the proton, $F_2(x, Q^2)$ has been measured in an entirely new kinematic region of Bjorken $x$, $2 \cdot 10^{-4} \leq x \leq 2 \cdot 10^{-2}$, for $8.5\,GeV^2 \leq Q^2 \leq 60\,GeV^2$. $F_2$ is observed to rise substantially as $x$ decreases through this region, consistent with BFKL motivated effects of the proton structure. It is, however, not yet possible to positively identify these effects in the $Q^2$ evolution of $F_2$, as the measurement of the latter presented here is consistent both with GLAP QCD evolution and scale invariance ($\chi^2/DoF = 0.4$).

# Appendix A

# Unfolding the Structure Function

In this analysis, unfolding is the extraction of the true structure function, $F_2(x)$ at fixed $Q^2$ (or $F_2(Q^2)$ at fixed $x$), from the measured distribution of the electron angle and energy, $\hat{g}(y)$. The procedure used is a general unfolding program by V. Blobel [43].

The expected distribution, $g(y)$, the structure function and the distribution of any remaining background events, $b(y)$, are related by the integral equation

$$g(y) = \int A(y,x)F_2(x)dx + b(y) \tag{A.1}$$

where $A(y,x)$, the kernel of the equation, is the resolution function. This describes the effects of the limited acceptance of the detector, its resolution, as well as the basic kinematic factors in the cross-section (eg the $\frac{1}{xQ^4}$ factor) other than the structure function itself. This resolution function is extremely complicated and cannot be calculated analytically. It is (approximately) determined by using Monte-Carlo simulation, with input structure function $f(x)$. From this one obtains an expected distribution $g(y)$, which is compared to the measured distribution and $f(x)$ is adjusted until the best fit of the distributions is obtained.

To extract the true function $F_2(x)$, equation A.1 has first to be re-written in a discrete form. This is done in two stages. Firstly the function $f(x)$ is expanded as a sum of $m$ cubic B-splines [47],

$$f(x) = \sum_{i=1}^{m} a_i p_i(x) \tag{A.2}$$

where $p_i(x)$ are a set of B-splines, and the $a_i$ are a set of coefficients that have to be determined. The B-splines are only non-zero over a small range of $x$, but

they overlap one another and sum to form a smooth function. The B-splines also satisfy the equations

$$\begin{aligned} p_i(x) &\geq 0 \\ \sum_i p_i(x) &= 1 \end{aligned} \tag{A.3}$$

The decomposition of a smooth function into cubic B-splines is shown in figure A.1.

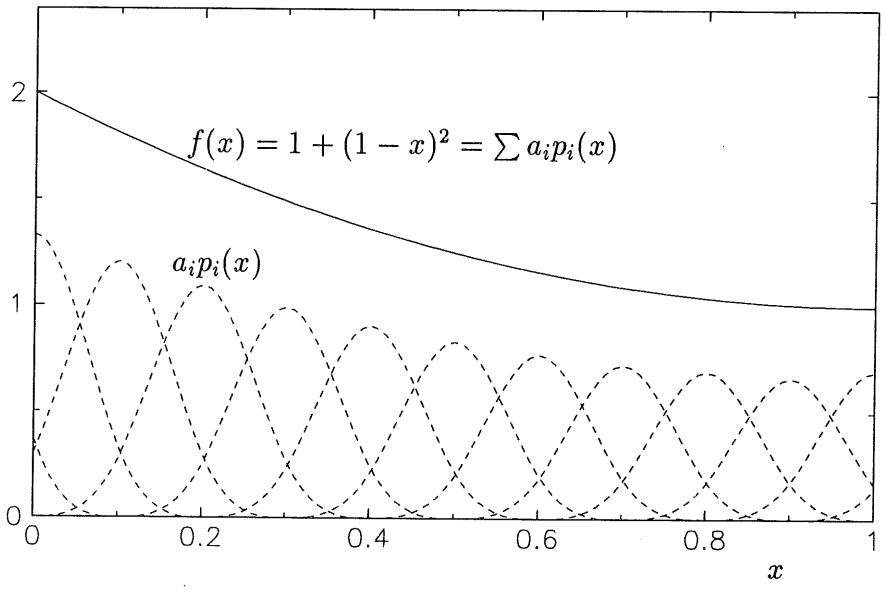


Figure A.1: The decomposition of a smooth function into cubic B-splines; the component spline functions are shown as a dashed line, their sum as a solid line.

After decomposition, equation A.1 is of the form

$$g(y) = \sum_{i=1}^{m} a_i A_i(y) + b(y) \tag{A.4}$$

with

$$A_i(y) = \int A(y,x) p_i(x) dx \tag{A.5}$$

The continuous functions $A_i(y)$, $g(y)$ and $b(y)$ are then integrated over small regions to make multi-dimensional histograms,

$$g_i = \int_{y_{i-1}}^{y_i} g(y) dy$$

$$\begin{aligned} b_i &= \int_{y_{i-1}}^{y_i} b(y)dy \\ A_{ij} &= \int_{y_{i-1}}^{y_i} A_j(y)dy \end{aligned} \tag{A.6}$$

Equation A.1 can then be written as a matrix equation

$$g_i = A_{ij}a_j + b_i \tag{A.7}$$

The elements $A_{ij}$ represent the expected number of events in the $i$'th bin in y $(\sqrt{E'_e}, \theta)$ space for a component of the structure function that is the $j$'th spline. In the Monte-Carlo, the true $x$ of the event is recorded, and the value of each of the B-splines is calculated. Since the B-splines are non-zero over only a small range of $x$, many of them will be 0. The electron energy and angle are taken from the simulation and this determines to which bin in $y$ space the event belongs. $A_{ij}$ is then filled with the values of the B-splines, weighted by a global factor to normalize the data and Monte-Carlo, $k_{lumi}$, and a factor depending on $i$ due to any efficiencies that the Monte-Carlo does not fully reproduce, $\epsilon_i$ (eg. the z-vertex efficiency).

$$A_{ij} = k_{lumi} \cdot \epsilon_i \cdot p_j(x) \tag{A.8}$$

The complete matrix $A_{ij}$ is built up by repeating the procedure for all the Monte-Carlo events that survive the cuts applied to the data.

Once the matrix has been determined, the coefficients $a_j$ have to be adjusted to give the best fit of the expected distribution, $g(y)$ and the measured one, $\hat{g}(y)$. The maximum likelihood method can be used to calculate a the coefficients. In this method, the product of the all the probabilities is maximized, by minimizing $S(a)$ as defined by

$$S(\mathbf{a}) = -\ln\left(\prod P_i\left(\hat{g}_i|g_i\right)\right) = -\sum \ln P_i\left(\hat{g}_i|g_i\right) \tag{A.9}$$

where $P_i$ is the probability of measuring $\hat{g}_i$ events in the $i^{th}$ bin when the expected number of events is $g_i$. In general this equation is non-linear and approximation methods have to be used to solve it.

Given an approximate solution to equation A.9, $\tilde{\boldsymbol{a}}$, $S$ can be expanded in the quadratic approximation as

$$S(\mathbf{a}) = S(\tilde{\boldsymbol{a}}) - (\mathbf{a} - \tilde{\boldsymbol{a}})^T\mathbf{h} + \frac{1}{2}(\mathbf{a} - \tilde{\boldsymbol{a}})^T\mathbf{H}(\mathbf{a} - \tilde{\boldsymbol{a}}) \tag{A.10}$$

where the elements of $\mathbf{h}$ and $\mathbf{H}$ are given by

$$\begin{aligned} h_j &= -\frac{\partial S}{\partial a_j} \\ H_{jk} &= \frac{\partial^2 S}{\partial a_j \partial a_k} \end{aligned} \tag{A.11}$$

Since $\mathbf{H}$ is symmetric, it can be transformed to a diagonal matrix, $\mathbf{D}$ by

$$\mathbf{D} = \mathbf{U}^T\mathbf{H}\mathbf{U} \tag{A.12}$$

where $\mathbf{D}$ contains the eigenvalues of $\mathbf{H}$ (ordered such that $D_{11} > D_{22} > \ldots$) and $\mathbf{U}$ the normalized eigenvectors. Defining a matrix $\mathbf{D}^{1/2}$ such that $\mathbf{D}^{1/2}\mathbf{D}^{1/2} = \mathbf{D}$, the basis vector $\mathbf{a}$ can be transformed by

$$\mathbf{a} = \mathbf{U}\mathbf{D}^{-\frac{1}{2}}\mathbf{a}_1 \tag{A.13}$$

Using equation A.13 in equation A.10 and omitting constant terms,

$$S(\mathbf{a}_1) = -\mathbf{a}_1^T\mathbf{D}^{-\frac{1}{2}}\mathbf{U}^T(\boldsymbol{H}\tilde{\boldsymbol{a}} + \mathbf{h}) + \frac{1}{2}\mathbf{a}_1^T\mathbf{a}_1 \tag{A.14}$$

The minimum of equation A.14, defined by $\nabla S = 0$, gives

$$\mathbf{a}_1 = \mathbf{D}^{-\frac{1}{2}}\mathbf{U}^T(\boldsymbol{H}\tilde{\boldsymbol{a}} + \mathbf{h}) \tag{A.15}$$

where $\mathbf{a}_1$ is an approximation to the result, given a starting point, $\tilde{\boldsymbol{a}}$. The nice feature of the result thus obtained is that the covariance matrix of the parameters, $\mathbf{a}_1$, is the unit matrix, $\mathbf{I}$, showing that the parameters are statistically independent.

Using the large statistics limit of the Poisson distribution in which

$$P(\hat{g}_i|g_i) = \frac{1}{\sqrt{2\pi}\sigma_i} e^{\frac{(\hat{g}_i - g_i)^2}{2\sigma_i^2}} \tag{A.16}$$

and $\sigma_i^2 = g_i \approx \hat{g}_i$, equation A.9 becomes

$$\begin{aligned} S(\mathbf{a}) &= \frac{1}{2}\sum \frac{(\hat{g}_i - g_i)^2}{\hat{g}_i} \\ &= \frac{1}{2}\sum \frac{(\hat{g}_i - A_{ij}a_j - b_i)^2}{\hat{g}_i} \end{aligned} \tag{A.17}$$

neglecting constant terms. The quadratic expansion is exact with

$$\begin{aligned} h_j &= \sum A_{ij}\frac{\hat{g}_i - g_i}{\hat{g}_i} \\ H_{jk} &= \sum \frac{A_{ij}A_{ik}}{\hat{g}_i} \end{aligned} \tag{A.18}$$

and so no iteration is required to find the result. This can be used as a starting point to find the solution based on the Poisson distribution, for which

$$P(\hat{g}_i|g_i) = \frac{e^{-g_i}g_i^{\hat{g}_i}}{\hat{g}_i!} \tag{A.19}$$

and so equation A.9 becomes

$$S(\mathbf{a}) = \sum g_i - \sum \hat{g}_i \log g_i \tag{A.20}$$

Since this is no longer quadratic, the solution has to be found by iteration using equation A.15.

Unfortunately, this simple approach to the unfolding results in some rather undesirable features. Owing to the smearing effects present in the measurement, the coefficients, $\hat{a}_i$, become highly correlated and the extracted function can oscillate wildly. Integrating the function over a bin of $x$ to extract the result then results in large (negative) correlations between bins.

To overcome this problem, regularization is used. In this it is assumed that the structure function is a smooth function of $x$. For a smooth function, the quantity

$$r(\mathbf{a}) = \int (f(x)'')^2 \, dx \tag{A.21}$$

should be small. Instead of only minimizing the products of the probabilities, the function

$$R(\mathbf{a}) = S(\mathbf{a}) + \tau r(\mathbf{a}) \tag{A.22}$$

is minimized, where $\tau$ is a regularization parameter whose value needs to be determined. As $\tau \to 0$, the original, oscillating solution is obtained, whilst as $\tau \to \infty$, the result becomes a straight line.

For cubic B-splines, $r(\mathbf{a})$ can be represented by the quadratic expression

$$r(\mathbf{a}) = \mathbf{a}^T \mathbf{C} \mathbf{a} \tag{A.23}$$

Inserting equation A.14 in equation A.22

$$R(\mathbf{a}_1) = -\mathbf{a}_1^T \mathbf{D}^{-\frac{1}{2}} \mathbf{U}^T (\boldsymbol{H}\tilde{\boldsymbol{a}} + \mathbf{h}) + \frac{1}{2}\mathbf{a}_1^T \mathbf{a}_1 + \frac{1}{2}\tau \mathbf{a}_1^T \mathbf{C}_1 \mathbf{a}_1 \tag{A.24}$$

where $\mathbf{C}$ and $\mathbf{C}_1$ are related by

$$\mathbf{C}_1 = \mathbf{D}^{-\frac{1}{2}} \mathbf{U}^T \mathbf{C} \mathbf{U} \mathbf{D}^{-\frac{1}{2}} \tag{A.25}$$

$\mathbf{C}_1$ can be transformed into a diagonal matrix, $\mathbf{S}$, defined by

$$\mathbf{S} = \mathbf{Y}^T \mathbf{C}_1 \mathbf{Y} \tag{A.26}$$

where $\mathbf{S}$ contains the eigenvalues of $\mathbf{C}_1$ (ordered such that $S_{11} < S_{22} < \ldots$) and $\mathbf{Y}$ the normalized eigenvectors. Defining a rotation in parameter space,

$$\mathbf{a}_1 = \mathbf{Y}\mathbf{a}' \tag{A.27}$$

equation A.24 can be rewritten as

$$R(\mathbf{a}') = -\mathbf{a}'\mathbf{Y}^T\mathbf{D}^{-\frac{1}{2}}\mathbf{U}^T(\boldsymbol{H}\tilde{\boldsymbol{a}} + \mathbf{h}) + \frac{1}{2}\mathbf{a}'^T(\mathbf{I} + \tau\mathbf{S})\,\mathbf{a}' \tag{A.28}$$

The regularized solution, $\hat{\boldsymbol{a}}$ is then given by

$$\begin{aligned} \hat{\boldsymbol{a}} &= (\mathbf{I} + \tau\mathbf{S})^{-1}\mathbf{V}^T\mathbf{D}^{-\frac{1}{2}}\mathbf{U}^T(\boldsymbol{H}\tilde{\boldsymbol{a}} + \mathbf{h}) \\ &= (\mathbf{I} + \tau\mathbf{S})^{-1}\overline{\boldsymbol{a}} \end{aligned} \tag{A.29}$$

where

$$\overline{\boldsymbol{a}} = \mathbf{V}^T\mathbf{a}_1 \tag{A.30}$$

Due to the orthogonality of $\mathbf{V}$, the covariance matrix of $\overline{\boldsymbol{a}}$ is same as for $\mathbf{a}_1$, the unit matrix (ie the parameters have a variance of one and are uncorrelated). Since the matrix $(\mathbf{I} + \tau\mathbf{S})$ is diagonal, the parameters $\hat{\boldsymbol{a}}$ are also uncorrelated. It can be seen that regularization is equivalent to multiplying each of the unregularized amplitudes by a factor $\frac{1}{(1+\tau S_{jj})}$. The sum of all of these factors can be considered as the effective number of independent contributions to the solution, $m_0$,

$$m_0 = \sum_{j=1}^{m} \frac{1}{1 + \tau S_{jj}} \tag{A.31}$$

$m_0$ then gives the number of bins in $x$ for the result. A lower estimate for $m_0$ can be found by testing the significance of the components of the unregularized solution, which then determines $\tau$.

Each of the parameters, $\hat{a}_i$, corresponds to a combination of B-splines that covers the entire $x$ range. The ordering of the eigenvalues of $\mathbf{S}$ means that the $j$'th solution oscillates more than its predecessor and has $(j-1)$ zeros. A normalized amplitude, $\alpha_j$, can be defined by

$$\alpha_j = \hat{\alpha}_j\sqrt{S_{jj}} \tag{A.32}$$

These $\alpha_j$ then have a variance of 1. Figure A.2 shows the absolute values of the first nine normalized amplitudes together with the damping function for the unfolding of $F_2(x)$ at $Q^2 = 15\,GeV^2$ ($m_0 = 5$).

For $m_0$ bins, the $(m_0+1)$th function is the one most likely to introduce correlations between neighbouring bins. The bin limits for integration are therefore chosen to minimize the integral of this component over the $x$ range. The 6th component of the solution in the unfolding of $F_2(x)$ for $Q^2 = 15\,GeV^2$ is shown in figure A.3, along with the bin limits.

The significance of the correlations was tested by generating 2000 deviations from the bin contents using the full covariance matrix and then calculating the

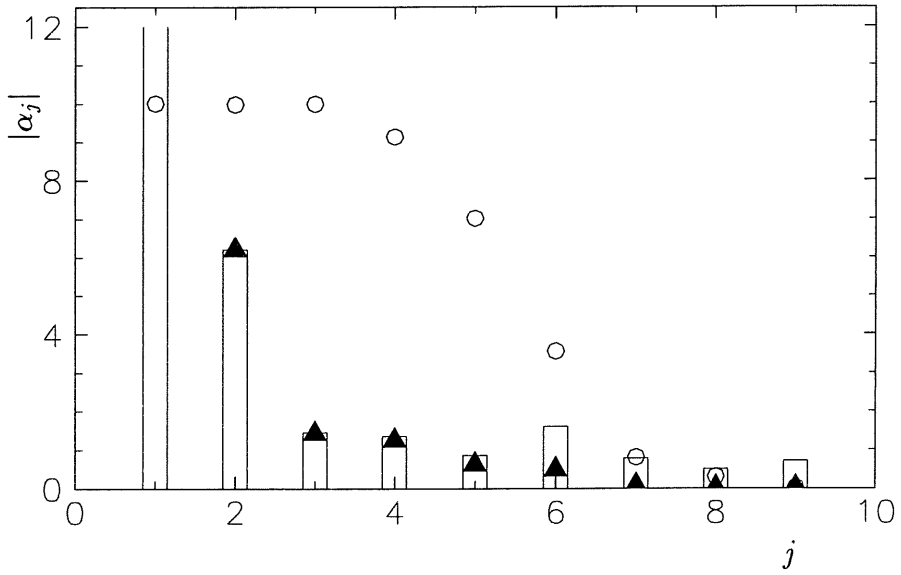


Figure A.2: The histogram shows the first nine normalized amplitudes for $F_2(x)$ at $Q^2 = 15\,GeV^2$ (the first amplitude is larger than the scale of the plot). The hollow circles show the damping factor multiplied by a factor of 10, and the triangles show the damped amplitude.

probability of such an occurrence using only the diagonal terms in the covariance matrix. If the distribution of this probability is flat, then the effect of the correlations is small and the errors on the results can be taken as the square root of the diagonal elements of the covariance matrix. This was the case with all the values unfolded in this thesis.

The solution for $F_2(x)$ at $Q^2 = 15\,GeV^2$ is shown in figure A.4. Note that the point at lowest $x$ is rejected as it is populated mainly by events for which the true kinematics lies outside the region of the kinematic domain defined by the cuts on the measured quantities.

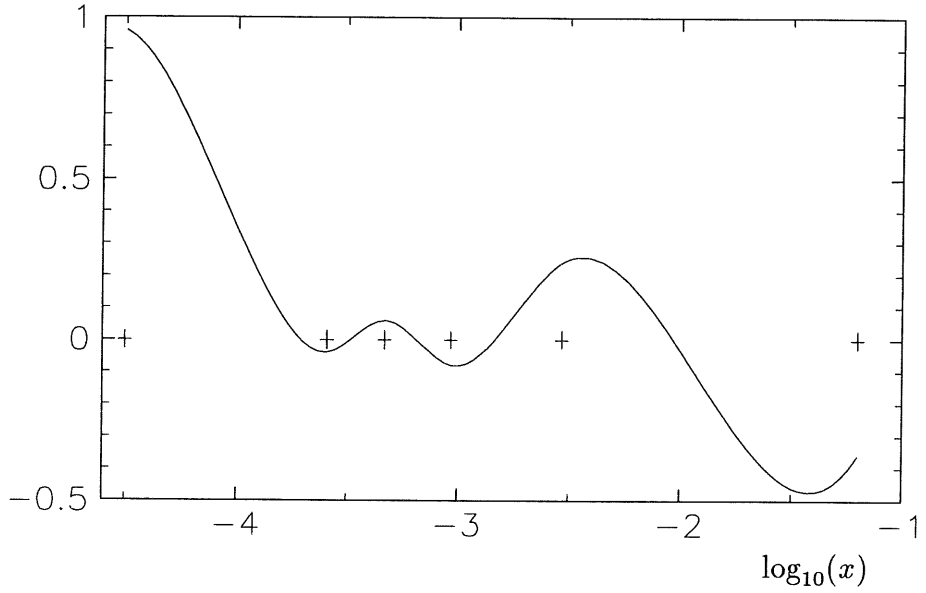


Figure A.3: The curve shows the 6th component of the solution for $F_2(x)$ at $Q^2 = 15\,GeV^2$. The crosses mark the bin limits for the result.

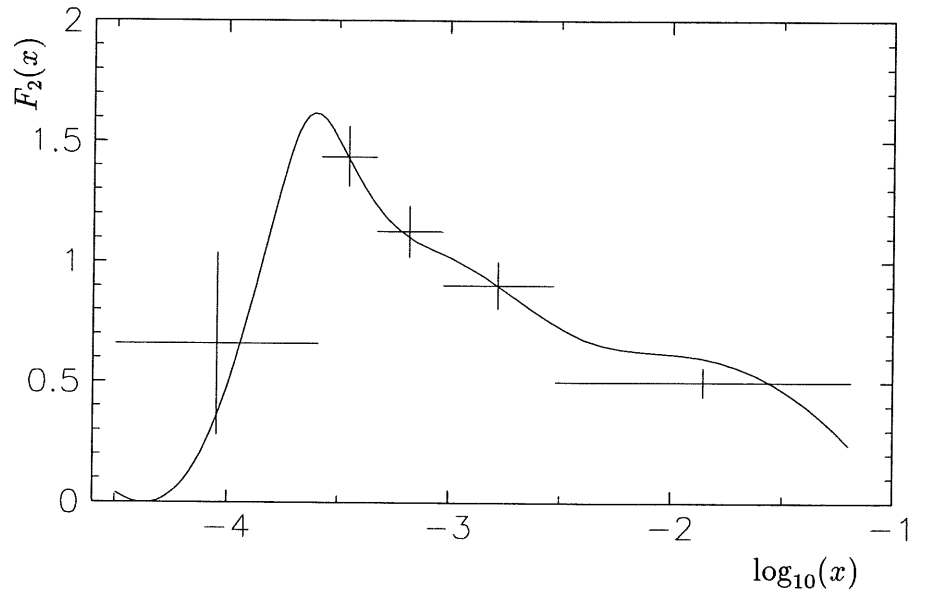


Figure A.4: The unfolded function $F_2(x)$ for $Q^2 = 15\,GeV^2$.

# References


[1] F. Jacquet, A. Blondel, *Proceedings of the Study of an ep Facility for Europe*, ed. U. Amaldi,DESY preprint, DESY 79–48, Hamburg (1979) 391

[2] U. Bassler, G. Bernardi, *Progress on Kinematical Variables Reconstruction. Consequences for DIS Physics Analysis at Low x*, H1 note, DESY, Hamburg, H1–03/93–274 (1993)

[3] A. Jacholkowska, *Determination of the Kinematic Variables from the fit of Electron and Hadron Variables*, H1 note, DESY, Hamburg, H1–04/93–283 (1993)

[4] J. Phillips *A Comparison of Kinematic Fitting with Conventional Reconstruction Techniques*, H1 note, DESY, Hamburg, H1–09/93–314 (1993)

[5] K. Gottfried, Phys.Rev.Lett. **18** (1967) 1174

[6] A. D. Martin, W. J. Stirling, R. G. Roberts, *Present status of parton distributions*, Journal of Physics G–volume 19, nr. 10, October 1993.

[7] V. N. Gribov, L. N. Lipatov, Sov.Journ.Nucl.Phys **15** (1972) 438 and 675
G. Altarelli, G. Parisi, Nucl.Phys. **B126** (1977) 298

[8] NMC Collaboration, Phys.Lett. **295B** (1992) 159

[9] BCDMS Collaboration, Phys.Lett **B223** (1989) 485

[10] S. J. Brodsky, G. P. Lepage, *Exclusive Processes in Quantum Chromodynamics*, ed. D. W. Duke, J. F. Owens, American Institute of Physics (1981)

[11] E. A. Kuraev, L. N. Lipatov, V. S. Fadin, Phys.Lett. **60B** (1975) 50; Zh.E.T.F **72** (1977) 377

[12] J. C. Collins, J. Kwiecinski, Nucl.Phys. **B316**, 307 (1989)

[13] A. D. Martin, W. J. Stirling, R. G. Roberts, Phys.Lett. **306B** (1993) 145, ibid. **309B** (1993) 492

[14] NMC Collaboration, Phys.Rev.Lett. **66** (1991) 2712

[15] CCFR Collaboration, Phys.Rev.Lett **64** (1990) 1207

[16] M. Bonesini et al., Z.Phys. **C38** (1988) 371

[17] J. Botts et al., Phys.Lett. **304B** (1993) 159

[18] M. Glück, E. Reya, A. Vogt, Z.Phys. **C53** (1992) 127; M. Glück, E. Reya, A. Vogt, Phys.Lett. **306B** (1993) 391

[19] A. M. Cooper-Sarkar, W. J. Stirling, *Summary of the activities of the Structure Function Working Group*, Journal of Physics G–volume 19, nr. 10, October 1993.

[20] G. A. Schuler, H. Spiesberger, Proceedings of the HERA Workshop Vol.3 Hamburg, Oct 29–30, 1991 p.1419. ed. W.Buchmüller, G.Ingelman.

[21] A. Kwiatkowski, H. Spiesberger, H.-J. Möhring Proceedings of the HERA Workshop Vol.3 Hamburg, Oct 29–30, 1991 p.1294 ed. W.Buchmüller, G.Ingelman.

[22] G. Ingelman, Proceedings of the HERA Workshop Vol.3 Hamburg, Oct 29–30, 1991 p.1366. ed. W.Buchmüller, G.Ingelman.

[23] H. Spiesberger et al., Proceedings of the HERA Workshop Vol.2 Hamburg, Oct 29–30, 1991 p.798. ed. W.Buchmüller, G.Ingelman.

[24] N. H. Brook, A. DeRoeck, A. T. Doyle, Proceedings of the HERA Workshop Vol.3 Hamburg, Oct 29–30, 1991 p.1453. ed. W.Buchmüller, G.Ingelman.

[25] Proceedings of the HERA Workshop Vol.3 Hamburg, Oct 29–30, 1991 p.1456. ed. W.Buchmüller, G.Ingelman.

[26] W. Zimmerman et al., *A 16 channel VME flash ACD system (F1001-FADC)*, H1 internal report, DESY, Hamburg (1989)

[27] H1 Collaboration, *The H1 detector at HERA*, DESY preprint, DESY 93–103, Hamburg (1993)

[28] H1 Collaboration, *Measurement of the Proton Structure Function, $F_2(x, Q^2)$, in the Low x Region at HERA*, DESY preprint, DESY 93–117, Hamburg (1993)

[29] K. Kleinknecht, *Detectors for Particle Radiation*, Cambridge University Press (1986)

[30] M.Aguilar–Benitez et al., *Particle Properties Data Booklet.*, (1992)

[31] H1 Calorimeter Group, *The H1 liquid argon calorimeter system*, NIM **A336** (1993) 460–498

[32] The VMEbus specification, IEEE standard 1014

[33] W. J. Haynes, *Bus-based architectures in the H1 data acquisition system*, VITA Int. Conf., *Open Bus Systems '92 in Research and Industry*, Zurich, Switzerland (1992), ISBN 90–72577–11–6 (1992) 27, Rutherford Appleton Laboratory report, RAL 92–048, (1992)

[34] G. Bernardi (Ed.), DESY central IBM, 'HERA01.H1REC.DOC' and files therein.

[35] H. Albrecht, P.Schleper, M. Erdmann, *PHAN - an H1 physics analysis package*, DESY central IBM, 'HERA01.H1PHAN.MANUAL', Hamburg (1993)

[36] V. Blobel, P. Binko, Z. Szkutnik, *FPACK - package for input/output*, DESY central IBM, 'HERA01.H1.FPACK.MANUALAB', Hamburg (1993)

[37] L. Womersley *Identifying the Scattered Electron in DIS Events at HERA*, H1 note, DESY, Hamburg, H1–06/92–229 (1992)

[38] H. Hufnagel, *L5-Event Classification*, DESY central IBM, deck ec_doc/ec_info in file 'HERA01.H1PHAN.CMZ'

[39] J. Meyer (Ed.), *Guide to Simulation Program H1SIM*, DESY central IBM, 'HERA01.H1SIM.GUIDE', Hamburg (1991)

[40] J. Heatherington, D. Kant, A. Mavroidis, G. Thompson, *Studies of ToF efficiency during Autumn 1992 run*, H1 note, DESY, Hamburg, H1–07/93–306 (1993)

[41] A. DeRoeck, Presentation to ELAN, June $10^{th}$ 1993

[42] A. DeRoeck, M.Klein, Th.Naumann, E.Peppel, U.Stoßlein, N.Wulff *Analysis II of the 1992 Data of the Structure Function* $F_2(x, Q^2)$, H1 note, DESY, Hamburg, H1–12/93–332 (1993)

[43] V. Blobel, *Unfolding Methods in High-Energy Physics experiments*, DESY preprint, DESY 84–118, Hamburg (1984)

[44] J-F. Laporte, *EPOKEPIK version 1.00/00 : a package to compute Parton Distributions Functions, Structure Functions and DIS Cross-Sections at HERA*, H1 note, DESY, Hamburg, H1–03/93–280 (1993)

[45] H1 collaboration, *Measurement of the Hadronic Final State in Deep Inelastic Scattering at HERA*, DESY preprint, DESY 92–162, Hamburg (1992)

[46] A. H. Mueller, Nucl.Phys. **B** (Proc.Suppl.) **18C** (1991) 125 A. H. Mueller, Nucl.Phys. **B282** (1987) 727

[47] C. de Boor, *A Practical Guide to Splines*, (1978) Springer-Verlag, New York, Heidelberg, Berlin.